**UNIVERSITÀ DEGLI STUDI DI MESSINA**

Dipartimento di Scienze Chimiche, Biologiche, Farmaceutiche ed Ambientali

Dottorato di Ricerca in Scienze Chimiche

Ciclo XXXVII

MUR PON "Ricerca e Innovazione" 2014–2020, Azione IV "Dottorati e Contratti di ricerca su tematiche dell'Innovazione."

---

# MULTIFUNCTIONAL HYBRID MAGNETO AND/OR PLASMONIC NANOSTRUCTURES FOR BIOMEDICAL APPLICATIONS

*Marco Abbate*

***Supervisor***

*Prof.ssa Anna Piperno*

***Co-supervisor:***

*Prof. Massimiliano Cordaro*

***Coordinatore:***

*Prof.ssa Concetta de Stefano*

---

**Anno Accademico 2023/2024**

La borsa di dottorato è stata cofinanziata con risorse del Programma Operativo Nazionale Ricerca e Innovazione 2014-2020 (CCI 2014IT16M2OP005) risorse FSE REACT-EU, Azione IV.4 "Dottorati e contratti di ricerca su tematiche dell'innovazione" e Azione IV.5 "Dottorati di ricerca su tematiche green"

# INDEX

## *Abstract*

In recent years, multifunctional nanostructures (NSs), combining ether the magnetic or the plasmonic properties of iron oxide or noble nanoparticles (*i.e.,* Ag or Au NPs) have attracted intensive research interest due to their unique properties and wide variety of promising applications including, selective sensors, functional composite materials or for biomedical use. This thesis focuses the attention on the development of new multifunctional hybrid magneto and/or plasmonic nanostructures using suitable biomolecule derivatives as templating or capping agents for the stabilization of hybrid components. Specifically, the carnosine modified with ferrocenyl unit (ferrocenylcarnosine, FcCAR) and the hyaluronic acid modified with β-cyclodextrins (HA-CD) were used as organic template/ligand/capping agent for the preparation of silver nanocluster and for the preparation of magneto and/or plasmonic hybrid nanostructures respectively.

The thesis is structured in two chapters. Chapter I reports the synthesis of ferrocenylcarnosine (FcCAR) and its applications as sensing materials in electrochemical analyses and as capping agents for the preparation of silvers nanoclusters. Chapter is articulated in the following sections:

- Synthesis of Ferrocenylcarnosine
- Preparation of Amphiphilic Silver Nanocluster (FcCAR@Ag NCs) and their evaluation as antimicrobial agents
- Modification of Screen-Printed Carbon Electrodes using Graphene Cyclodextrin and Ferrocenyl-Carnosine

Chapter II reports the synthesis of hyaluronic acid functionalized with β- cyclodextrin as delivery systems and for the development of magneto and/or plasmonic nanostructures.

The chapter II is articulated in the following sections:

- Development of HA-CD Drug Delivery System
- Mono and Bi-metallic Hybrid HA-CD Drug Delivery System

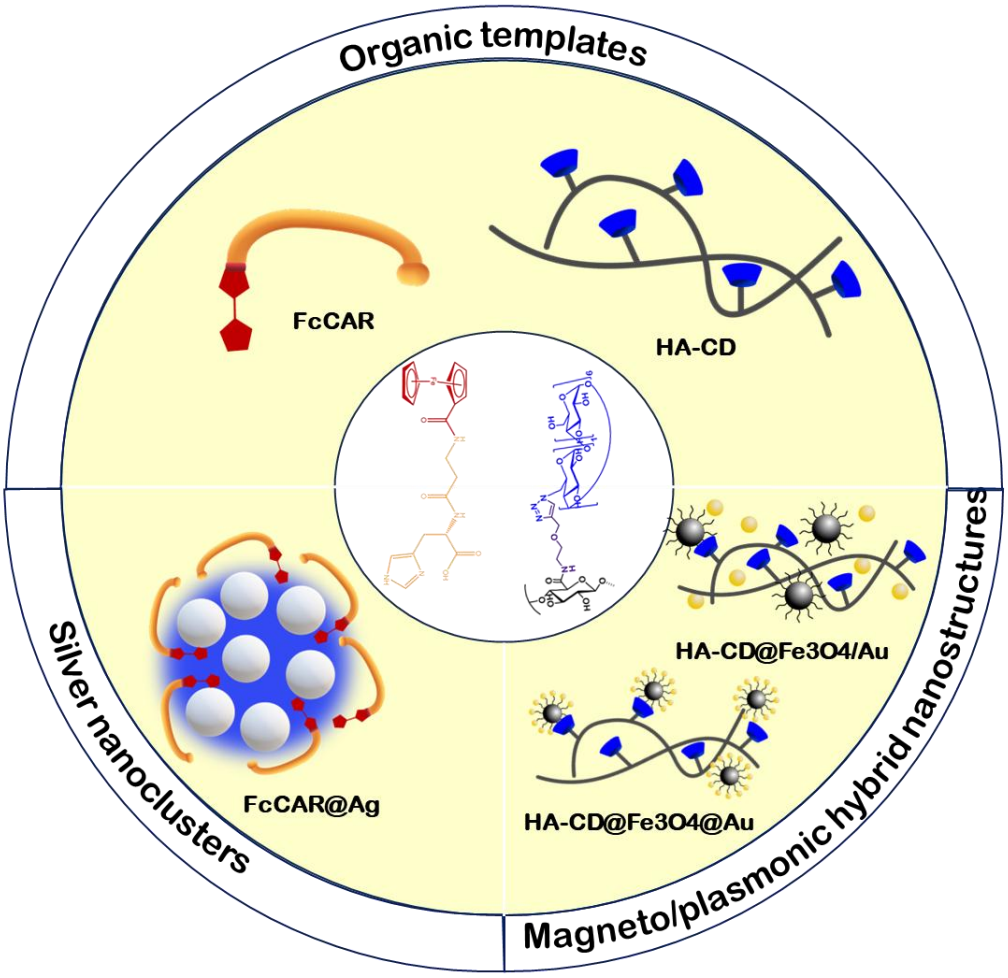


General overview of multifunctional hybrid magneto and/or plasmonic nanostructures based on ferrocenylcarnosine (FcCAR) and hyaluronic acid modified with β-cyclodextrins (HA-CD).

The fellowship supporting this work was awarded by MUR PON "Ricerca e Innovazione" 2014–2020, Azione IV "Dottorati e Contratti di ricerca su tematiche dell'Innovazione."
The project was carried out in collaboration with Institute CNR - Istituto per i Processi Chimico Fisici (Messina). Part of this work (six months) has been carried out during a research period abroad at the Nanotech Solutions (NTSOL, Spain) under the supervision of Dr Francisco J Teran.

# Chapter 1

# HYBRID NANOSTRUCTURES BASED ON FERROCENYLCARNOSINE

## Introduction

Carnosine (CAR) is a water-soluble dipeptide made from β-alanine and hystidine [1]. Discovered more than one century ago, this molecule was found in mammals, especially in skeletal muscles, olfactory bulb and brain tissue, with a concentration on the scale of millimolar [2]. Even if still today his physiologically role in human organism is not completely clarified the antioxidant properties and the ability to interact with bivalent metal cations were proved (Figure 1). The physiological properties of CAR depend on its ability to complex of bivalent metal cations, such as $Cu^{2+}$, $Mn^{2+}$, $Zn^{2+}$, $Ru^{2+}$, $Co^{2+}$, $Ni^{2+}$, $Cd^{2+}$, $Mg^{2+}$, and $Ca^{2+}$ [4]. CAR is a polydentate ligand and the metal coordinating sites include the imidazole nitrogens, the carboxylate group, the peptide linkage and the terminal amino group. [5]. Recently, the electrochemical properties of CAR were investigated by voltametric analyses [6] furthermore, the chemical modification of CAR with electroactive unit such as ferrocene unit improved the redox ability. Ferrocene is an electroactive small molecule, easily to functionalize [7] and works well as a reversable redox system (Fe (II)/Fe (III) for $Fc/Fc^{+}$ respectively) [8] conversely modifying amino group of β- alanine (to retain recognition sites of CAR) improve the application as a redox active system [9].

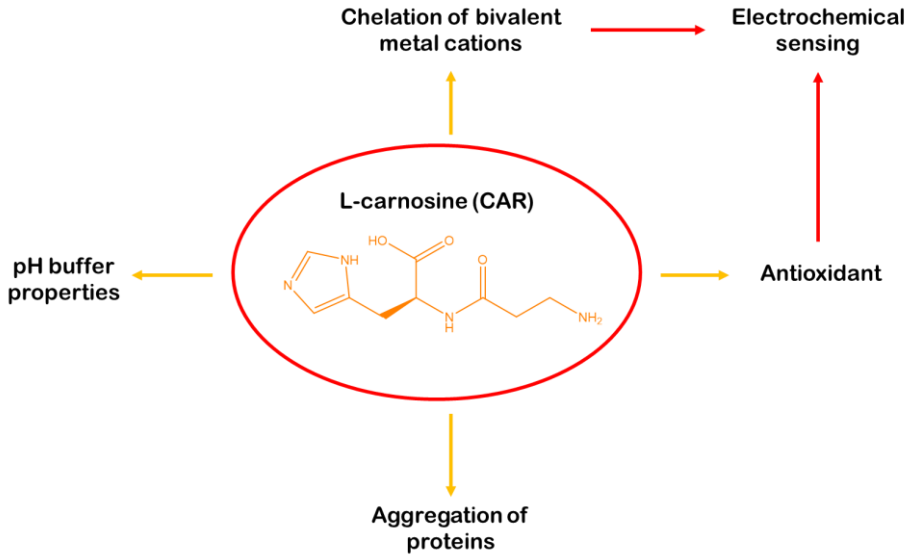


**Figure 1:** Overview of the carnosine properties. [3]

As peptide CAR was also investigated as templates for the synthesis of metal nanoparticles. Specifically, noble metal nanoclusters (Au, Ag, Pt) are a class of compounds which exhibit fluorescence characteristics. Their low toxicity, biocompatibility and biostability make them suitable for imaging, sensing and drug-delivery applications. Over the years, various chemical-physical synthesis methods have been indicated, for the preparation of metal nanoclusters the use of strong reducing agents and the possibility of aggregation of the structures has pushed towards the search for greener and milder methods for synthesis that improve their stability over time. To achieve this goal, by green synthesis approach, many researchers have turned their attention to natural compounds such as proteins and peptides. Protein templates can act simultaneously as both capping agents and reducing agents in the synthesis of metal nanostructure. The reducing ability of proteins is due to the aromatic amino acid residues, such as tyrosine (Tyr), tryptophan (Trp) and phenylalanine (Phe), under alkaline conditions (pH >11). Moreover, some proteins possess metal binding sites, such as N-terminal amines, histidine (His) and cysteine (Cys) residues. NCs based Lactoferrin (Lf), ovalbumin (OVA), gelatin (GEL), lysozyme, human serum albumin (HSA) and bovine serum albumin (BSA) are reported in literature. [10,11]

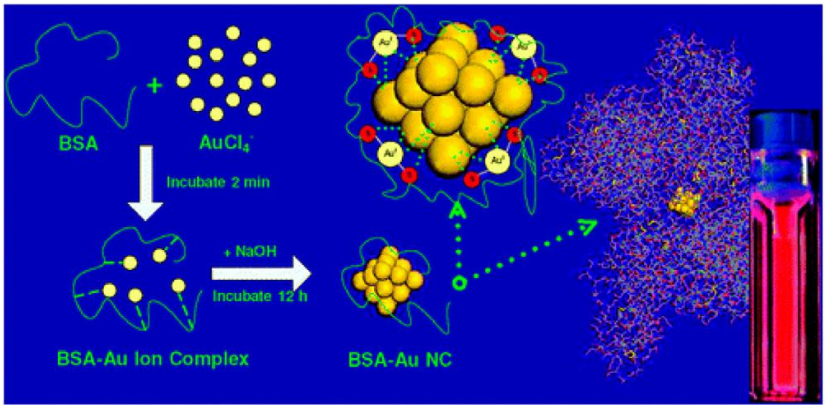


**Figure 2:** Au NCS synthesis from BSA as template [10]

Due to the presence of histidine in the chemical structure, CAR was investigated as template agent in the preparation of Au NCs [12,13]. Au NCs were obtained from free CAR in aqueous environment, without drastic reducing agents, with the sole aid of temperature and alkaline conditions (NaOH) to favour the formation of nanoclusters. The presence of luminescence products was demonstrated by the strong emission and absorption bands in fluorescence spectrum (Figure 3). TEM analysed confirmed the nanocluster nature of the nanostructures with an average diameter of around 2.3 nm (Figure 4).

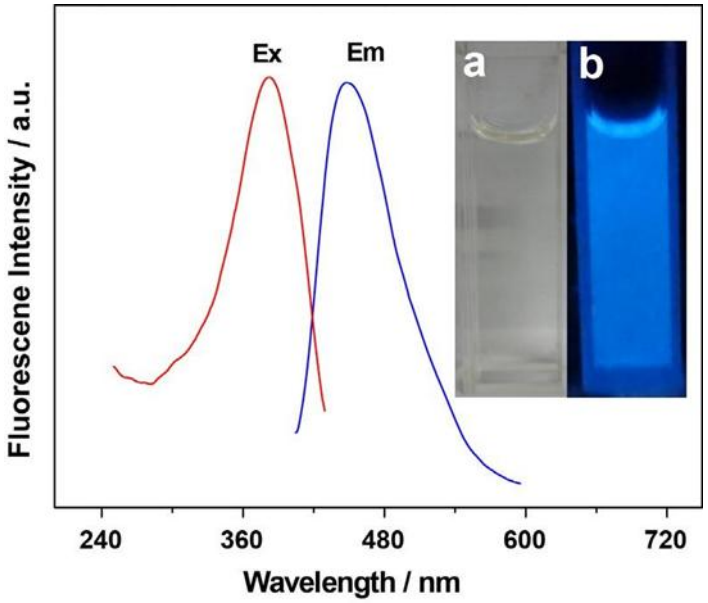


**Figure 3:** Fluorescence excitation and emission spectra of AuNCs: fluorescence excitation peak at 385 nm, red line, and fluorescence emission peak 448 nm blue line, respectively. Inset: Au NCs under visible light (a) and UV light with the wavelength of 365 nm (b).[13]

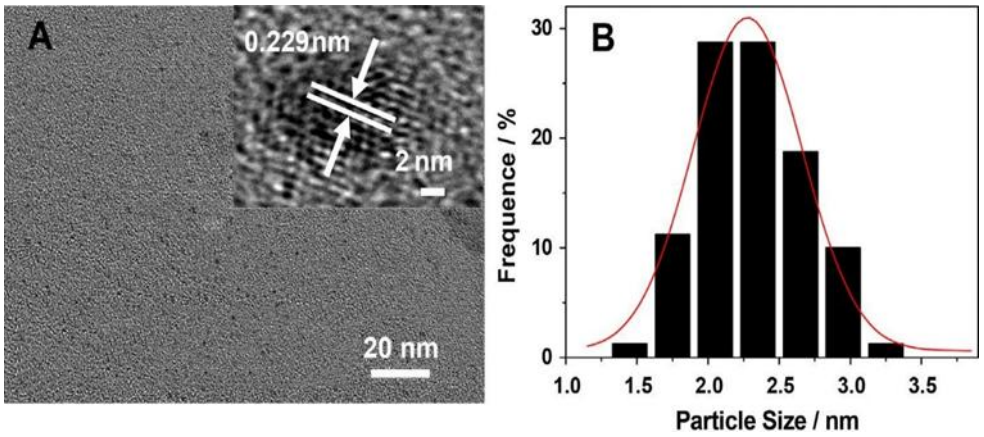


**Figure 4:** TEM image (A) and size-distribution histogram (B) of AuNCs. Inset shows the corresponding HR-TEM image. [13]

CAR is considered among other peptidic ligands in the production of gold nanoclusters (Au NCs) due to its capability to « shield », stabilize and have an influence on the properties of these nanostructures [14], now, at the best of our knowledge, no silver nanoclusters using carnosine as ligand were described in literature.

## Synthesis, Characterization and Properties of Amphiphilic Silver Nanoclusters

Noble metal nanoclusters (NCs) gained increased interest due to their extremely small nanosize, along the angstrom border, and their amazing properties, such as intrinsic tunable photoluminescence (PL), large Stokes-shift, non-toxicity, antimicrobial activity and great photostability [15]. Are extremely small in dimension (1-5 nm) and can be green-synthesized using template-assisted approaches in the presence of proteins [16], peptides [17], amino acids [18], etc. The kinetically controlled syntheses, using large excess of proteins or peptides as template are considered the elected strategies for the preparation of NCs in nanomedicine. Several proteins (i.g.,bovine serum albumin, lysozyme, globulins etc) or peptides (e.g, carnosine, glutathione, etc) have been investigated for the preparation of noble metal NCs, but the role of the specific amino acid (aa)of the peptidyl backbone is still not clear. From these studies emerged that AgNCs preparation is more challenging than AuNCs probably due to their relative susceptibility in solution under atmospheric conditions [19].

The physicochemical properties of Ag NCs such as size, the nature of the surface ligands (which dictate solubility, charge and stability) are strictly interrelated to their antibacterial activity. Recently, an increasing number of studies show that silver nanoparticles have efficient antibacterial activity due to their size and shape [5,20]. For example, Martinez-Castanon et al. [21,22] studied antimicrobial activity of silver nanoparticles with increase and decrease of size against *Escherichia coli* (E. coli) and *Staphylococcus aureus* (S. aureus) and found that the bactericidal properties decreased and got weaker with the increase of size of the silver nanoparticles. Lu et al. found the occurrence of the same phenomenon when they tested the antimicrobial activity of silver nanoparticles of different sizes against pathogenic bacteria [23,24]. In the framework of my research PhD thesis, the attention was focused on to the properties of Silver NCs obtained by amphiphilic ligands endowed of electrochemical properties such as Ferrocenylcarnosine (FcCAR).

## Synthesis of Ferrocenylcarnosine

The synthesis of FcCAR (Figure.5) was optimized compared to previously reported procedures [13], resulting in higher yield and purity of the final product. The use of EDCI and NHS as coupling reagents enabled the preparation of Fc-NHS derivative without forming the dicyclohexylurea byproduct. After purification by chromatography column, the intermediate was coupled with CAR and the crude reaction mixture was further purified by chromatography, using a gradient of DCM to DCM:MeOH (1:1) as eluent. Purification under weak acidic conditions, due to the silica support, prevented the formation of ferrocenyl aggregates, which are typically observed when water is used in

the synthesis and purification process. Fc-CAR was fully characterized by NMR spectroscopy. The proton signals of the CAR and Fc moieties were clearly distinguished in the 1H-NMR spectra. The chemical shifts of protons in the CAR moiety matched those of L-carnosine, under identical experimental conditions ($D_2O$ as deuterated solvent and neutral pH) (Figure 6). An evident downfield shift of H-11 protons, adjacent to nitrogen, was observed due to the formation of amide. The enantiotopic protons at C-6 were distinguished in two distinct peaks at 2.84 and 3.02 ppm, respectively, while the H-7 proton signal appeared as a double doublet at 4.33 ppm. Other protons showed no notable differences, except for the imidazole protons which exhibited large variations in chemical shift depending on sample concentration and pH. The Fc protons were anisotropic on the derivatized cyclopentadienyl ring, and two different signals were observed at 4.61 ppm and 4.40 ppm for protons H-15,18 and H-16-17, respectively. The five protons on the other cyclopentadienyl ring were equivalent, appearing as a single signal at 4.09 ppm. The $^{13}C$ NMR spectrum of Fc-CAR clearly showed three peaks for the carbonyl carbons at low fields (173-177 ppm), corresponding to two amides and one carboxylic acid group.

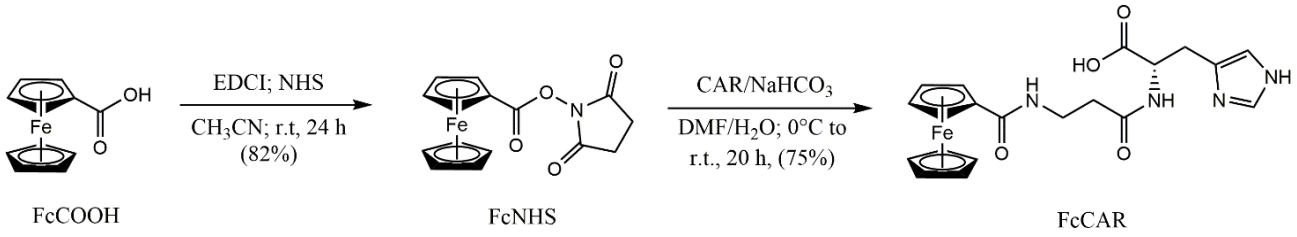


**Figure 5:** FcCAR Synthesis

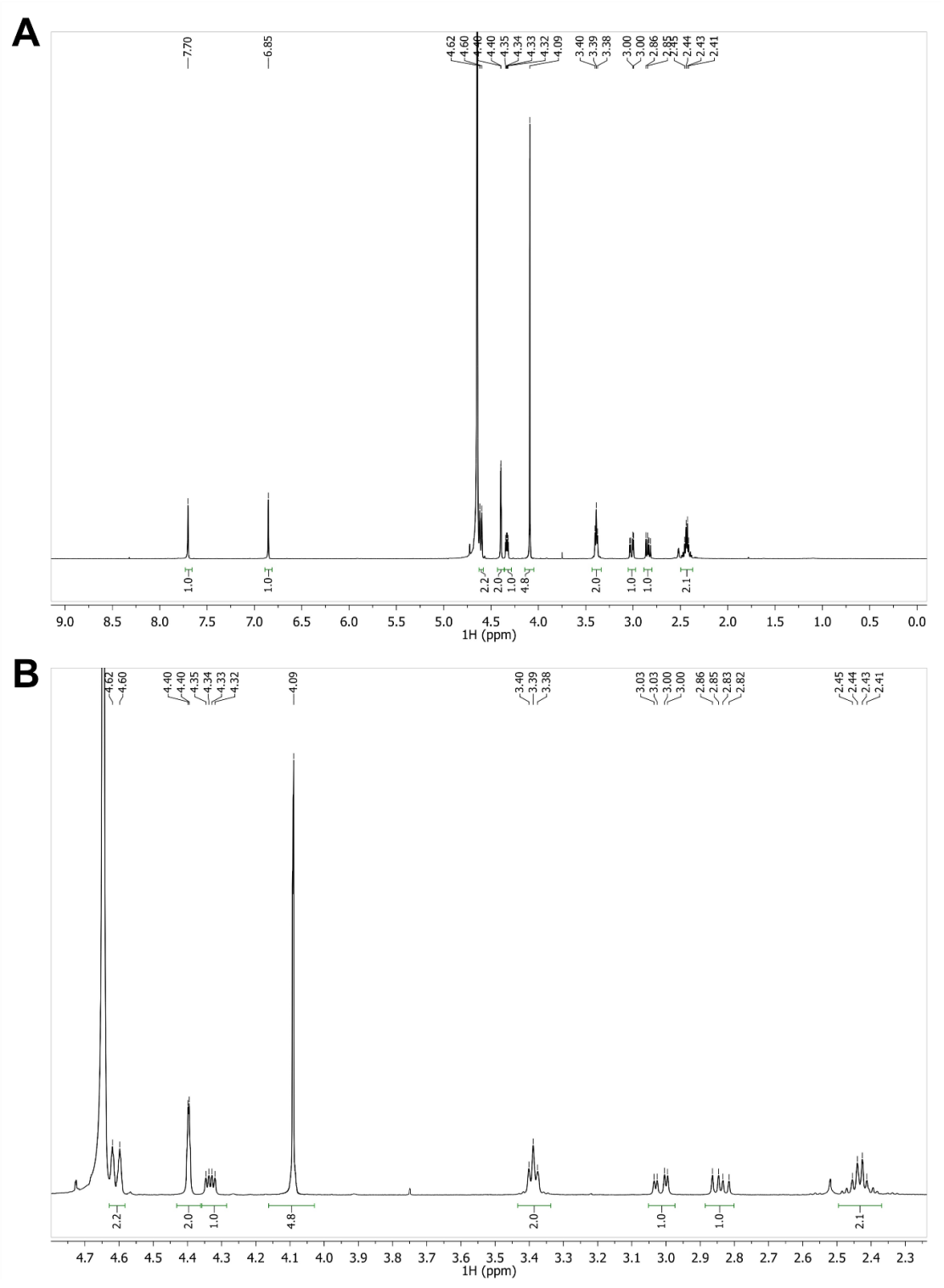


**Figure 6:** $^{1}$H-NMR ($D_2O$, 500 MHz) of Ferrocenyl-carnosine (FcCAR) (A), and a magnified area from 2.2 to 4.8 ppm (B).

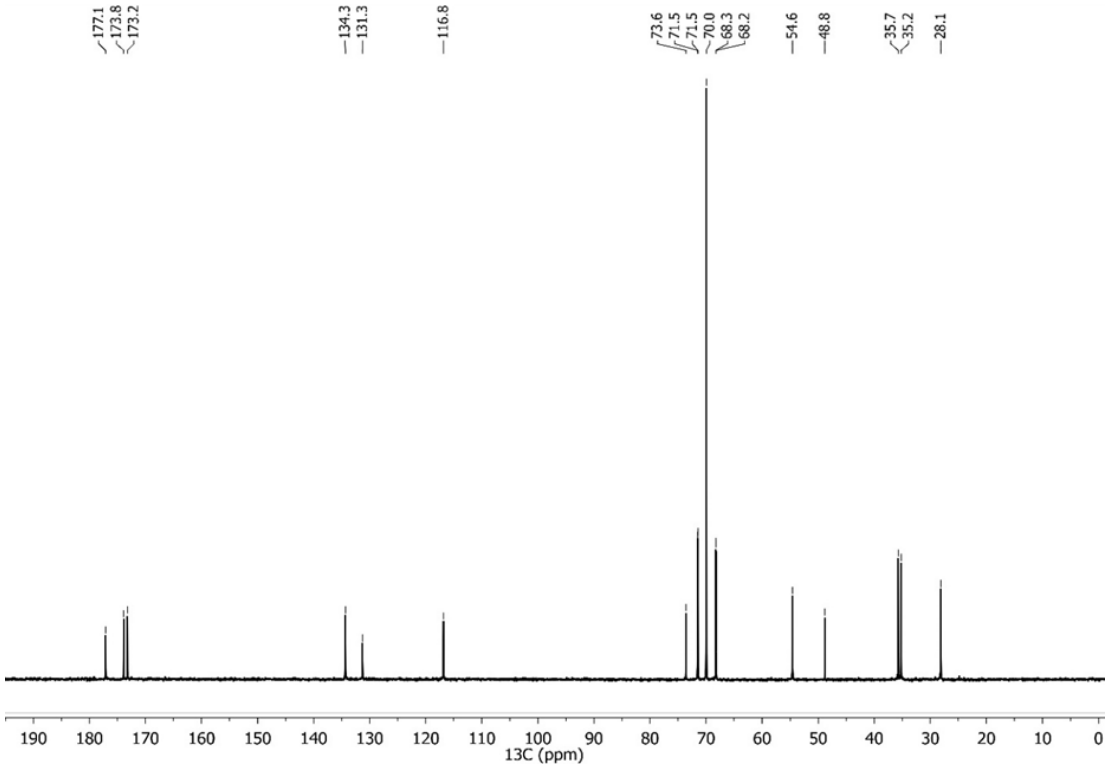


**Figure 7:** $^{13}$C-NMR ($D_2O$, 125 MHz) of Ferrocenyl-carnosine (FcCAR).

## Amphiphilic Silver Nanocluster (FcCAR@Ag NCs) and their Antimicrobial Properties

Nanoclusters were synthesized in one-step template-assisted method by adding silver ions to the heated aqueous solution of the ligand in very high large excess and in the presence of ascorbic acid as mild reducing agent. According to existing literature protocols, the condition (pH of ~11.5) that promotes the formation of clusters was adopted. [25]. In these experiment conditions, the main functional groups of the ligand (FcCAR) are in the deprotonated form [5]. Several attempts to optimize the PL property of NCs were carried out by varying L/Me ratio, temperature and reaction time (Table 1, Entry 1-3). The best PL properties were obtained using the experimental conditions of Entry 1 (Table 1). Briefly, a concentrate aqueous solution of ligand (100 mM) pre-heated to 80 °C was mixed with $AgNO_3$ aqueous solution (5 mM) under stirring. Ascorbic acid (0.02 mL, 50 mM) was added to assist the reduction of silver ions and finally the pH was corrected by adding NaOH (1 M). The samples prepared at lower L/Me molar ratio (e.g., FcCAR/$Ag^+$/6.25:1, Entry 2 Table 1) showed PL properties lower than Entry 1 sample. In order to investigate the role of ferrocene units on the formation of Ag NCs, the protocol of Entry 1 was applied to unmodified CAR: despite the higher ligand excess and the presence of ascorbic acid no products with measurable PL were detected (Entry 4 Table 1). These results pointing out the linchpin role of ferrocene unit that increasing the reducing capacity of the natural dipeptide enables the formation of nanoclusters containing the metals in dominantly zero oxidation state.

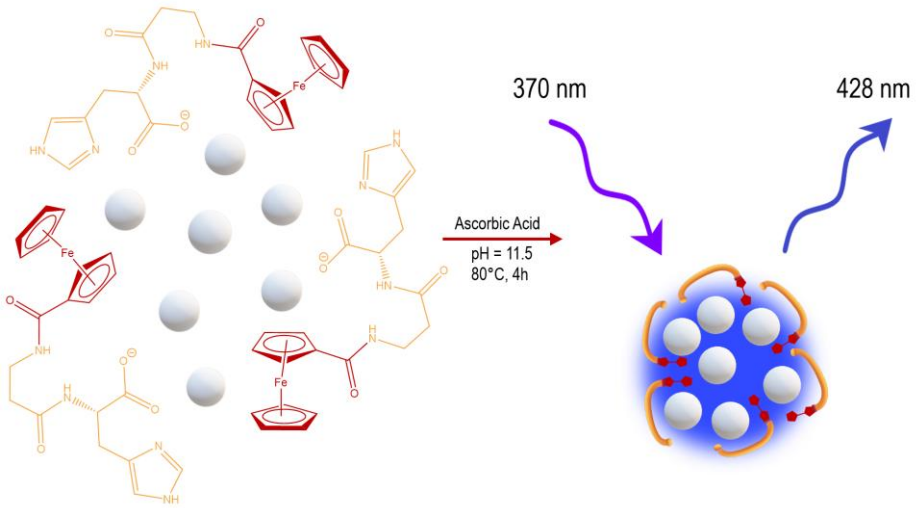


**Figure 8.** Representative synthesis of Silver Ferrocenyl Carnosine Nanoclusters (FcCAR@Ag NCs)

**Table 1**: Experimental protocol of silver nanocluster synthesized

| *Entry* | **Ligand** | **L/Me** | **T/time** | **Results** |
|---|---|---|---|---|
| 1 | FcCAR | 62.5/1 | 80°C/4h, pH=11,5 | NCs with maximum PL intensity |
| 2 | FcCAR | 6.25/1 | 80°C/4h pH=11,5 | NCs with good PL intensity |
| 3 | FcCAR | 62.5/1 | 80°C/12h or 40°C/4h, pH=11,5 or pH 7.5 | products with weak PL property and/or formation of Ag NPs and metallic Ag |
| 4 | CAR | 62.5/1 | 80°C/4h pH=11,5 | products with poor PL property |

The profile of FcCAR@Ag NCs was investigated via transmission electron microscopy (TEM) analyses and by their peculiar optical properties. Via TEM we could see FcCAR@Ag NCs exhibiting a spheric shaped morphology and a narrow particle size distribution with a mean diameter of 2.75 ±0.35 nm (Figure 9B). The hydrodynamic diameter of FcCAR@Ag NCs measured by dynamic light scattering showed an average size of ~45 nm in water (Figure 8A). The negative ζ-potential value -25,3 mV ensured a high stability in the colloidal state.

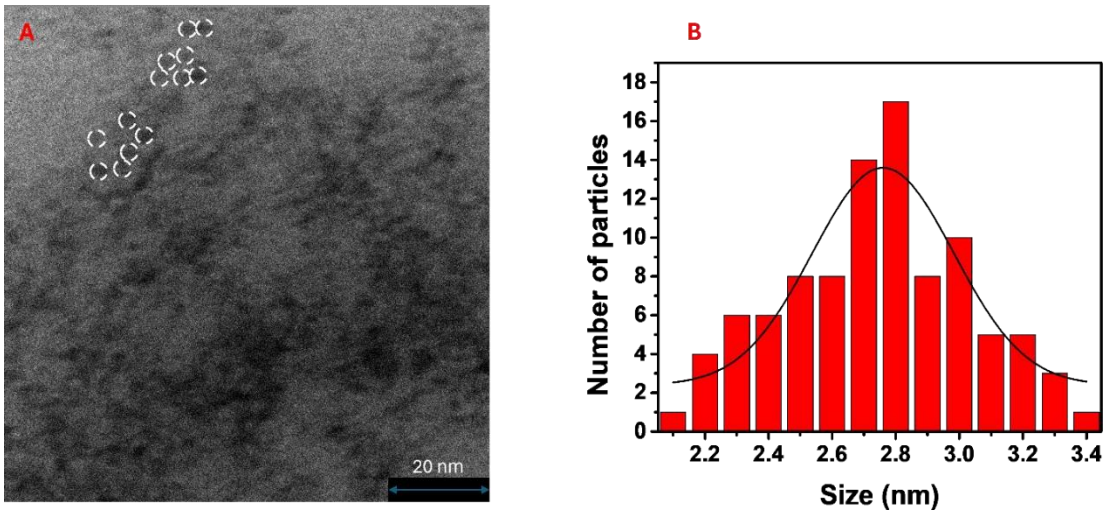


**Figure 9:** A) TEM image of FcCAR@Ag NCs (Scale bar: 20 nm); B) Size distribution of FcCAR@Ag NCs

- **Table 2: Particle size distribution and ζ-potential of FcCAR@Ag NCs and FcCAR**

| Sample | $D_H$ (nm ± SD)[1,2](%)[3] (Intensity) | $D_H$ (nm ± SD)[a,b](%)[c] (Number) | ζ (mV ± SD) |
|---|---|---|---|
| **FcCAR@Ag** from Entry 1 | 72,6 ± 5,3 (100)<br>588 ± 249 (83) | 45,4 ± 5,45 (100) | -25,3 ± 4,8 |
| **FcCAR** | 131 ± 632 (9) | 104± 28 (90) | -11,7 ± 4,7 |

[1]SD was calculated on three different batches. [2]Size with corresponding intensity % distribution. [3]Size with corresponding number % distribution.

From the intrinsic blue photoluminescence (PL) observed under UV irradiation and the absence of any significative surface plasmon resonance band in the range 400−450 nm in the UV/Vis spectrum (Figure 10a), is suggested the formation of ultrasmall AgNCs. Then, the peculiar intrinsic PL properties of FcCAR@Ag NCs were assessed by a comprehensive spectroscopical characterization that included UV/Vis and excitation/emission spectra (Figure 10b) and the determination of the absolute quantum yield (QY%) value.

UV/Vis absorption spectrum (Figure 10) exhibits the ligand bands at 262, 306 nm and a shoulder peak around 345 nm for both FcCAR and FcCAR@Ag NCs, thus demonstrating the functionalization of Ag NCs with the carnosine derivative. As reported in literature [26] there no a clear surface plasmon band around 400 nm indicating the stability of FcCAR@Ag NCs in the colloidal dispersion without the formation of larger Ag nanoparticles. It is well-known that amino acid conjugates of ferrocene can form amphiphiles structures with emission properties tunable through their aggregation behavior [27,28]. FcCAR@Ag NCs showed high fluorescence emission at 425 nm by excitation at 390 nm whereas a weak emission property was detected for the ligand (FcCAR) in the same experimental conditions (Figure 12) although it could produce fluorescent nanoaggregate [28]. We hypothesize that an increased aggregation-induced emission could occur by arrangement of Fc-CAR amphiphiles around Ag NCs. Emission properties of FcCAR@Ag NCs was confirmed by fluorescence emission spectra at different exicitation wavelength (Figure 13) and by excitation spectra (Figure 14) which assessed that the emission bands are due to the electronic transition of FcCAR ligand in the range 260-280 nm.

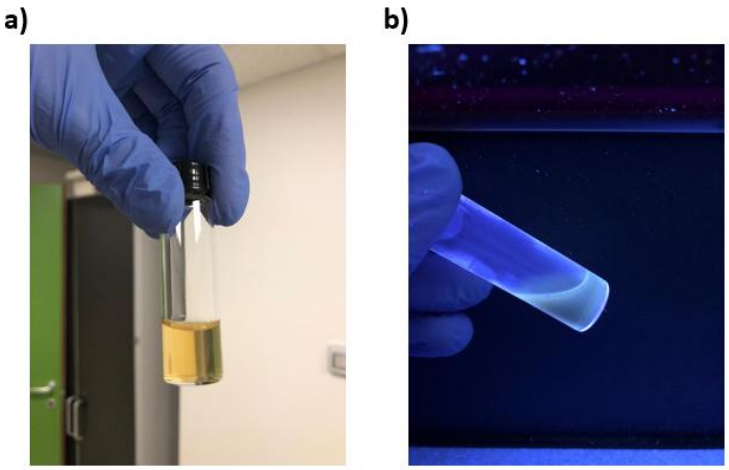


**Figure 10**: a) FcCAR@AgNCs solution under ambiental lighting (brownish). b) FcCAR@AgNCs solution under UV irradiation (change in color, we observe a blueish emission).

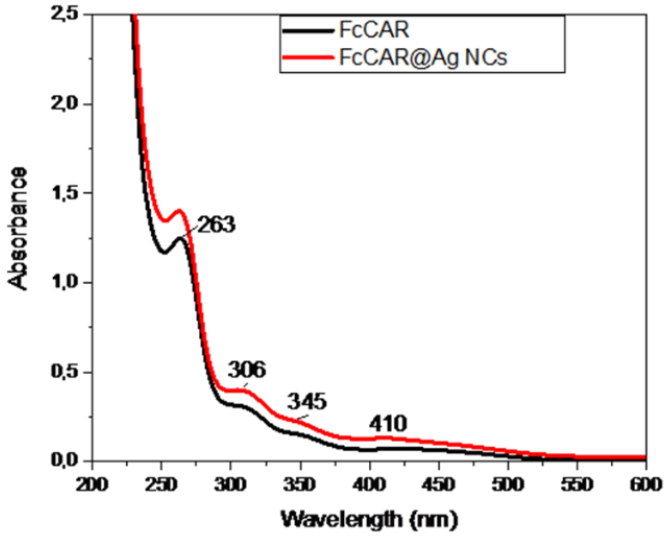


**Figure 11:** UV/Vis spectra of [FcCAR]= 0.22mM (black line) and FcCAR@AgNCs (red line). d = 1 cm

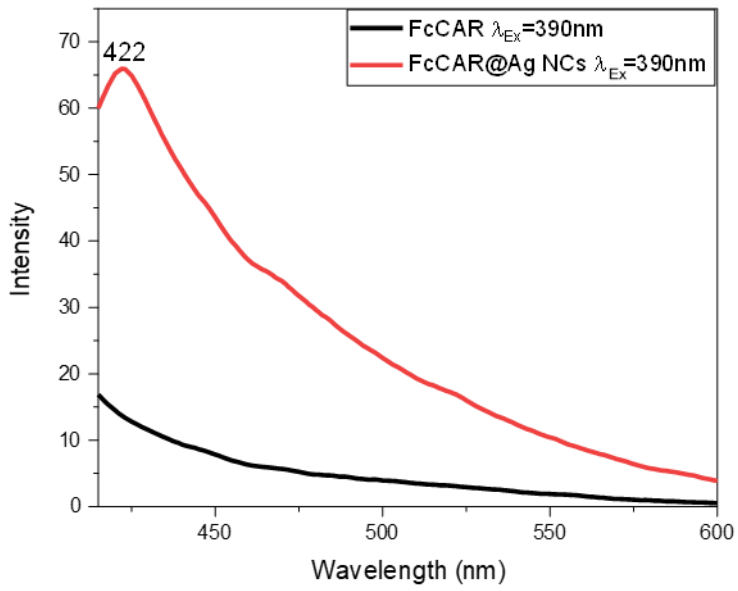


**Figure 12:** Fluorescence emission spectra FcCAR (black line) and FcCAR@Ag NCs (red line), at the excitation wavelength of 390 nm.

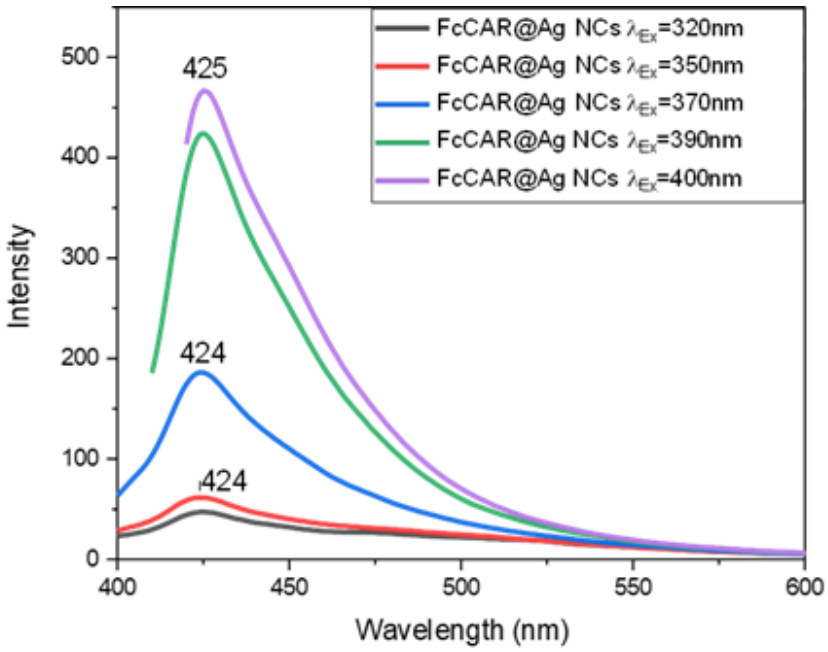


**Figure 13:** Fluorescence emission spectra of FcCAR@Ag NCs at different excitation wavelength at different excitation wavelengths ([FcAR]= 220 µM, d= 1cm).

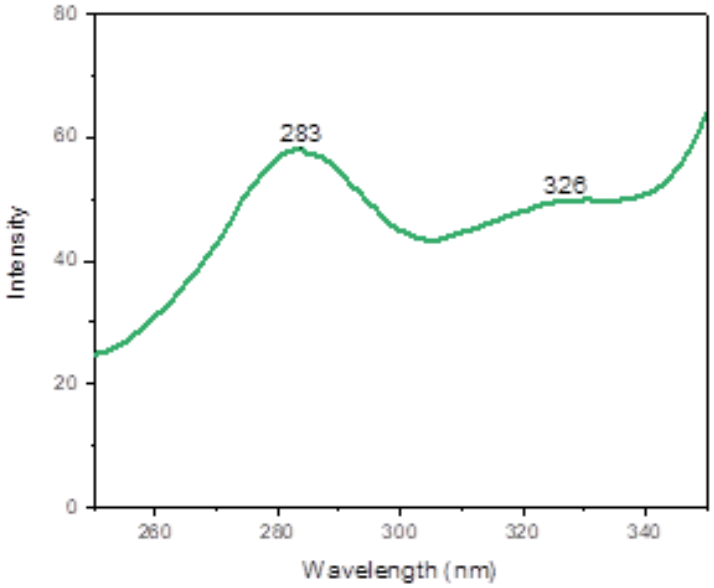


**Figure 14:** Fluorescence excitation spectra of FcCAR@AgNCs [FcAR]= 220 μM, d= 1cm, = 1cm, $\lambda_{em}$= 425 nm).

The quantum yield (QY%) of the blue-emitting products FcCAR@Ag NCs was calculated to be 5.9 % using an integrating sphere from JASCO. The fluorescence lifetime decay curve was extracted for both the FcCAR substrate and FcCAR@Ag NCs is showed in Figure 15.

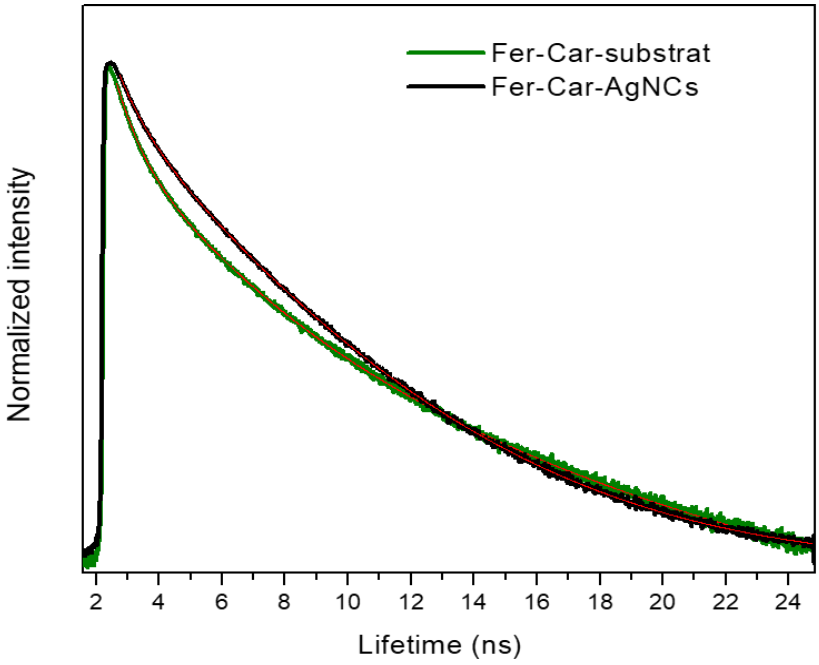


**Figure 15:** Fluorescence lifetime-decay curves of FcCar-substrat (green line) and FcCarAgNCs (black line – diluted 1:165 from the fresh prepared sample)

The fluorescence three-component lifetimes were calculated using tailfit fitting operations until the standard deviation, the residues and and $\chi^2$ converged to optimal values and the results are presented in Table 3. Changing from substrate to substrate-AgNCs there is a slight decrease in the average lifetime, from 4.58 to 3.51 ns. $t_1$ component reducing from 7.2 to 5 ns after the formation of the AgNCs inside the FcCAR matrix is the principal motive of the decrease of average lifetime of FcCAR@Ag.

**Table 3:** The fluorescence three-component lifetimes

| | **$t_1$** (ns) | **$I_1$** (%) | **$t_2$** (ns) | **$I_2$** (%) | **$t_3$** (ns) | **$I_3$** (%) | **$t_{av\ int}$** (ns) |
|---|---|---|---|---|---|---|---|
| FcCAR | 7.2 | 49.4 | 2.4 | 39.9 | 0.59 | 10.7 | 4.58 |
| FcCAR@Ag NCs | 5.0 | 47.6 | 2.5 | 44.3 | 0.68 | 8.2 | 3.51 |

## Antibacterial activity of FcCAR@AgNCs

The antibacterial activity of FcCAR@Ag NCs against planktonic growth of Gram positive and Gram-negative bacteria is reported in Table 4. MIC and MBC trends in the experiments performed are similar, with values ranging respectively values ranging from 2.9 μg/mL to 5.8 μg/mL for MIC and for MBC values ranging from 2.9 μg/mL to 46.7 μg/mL for all bacteria. Conversely $AgNO_3$ showed a lower efficacy against *S. aureus* and *E. coli.*

Studies of FcCAR@Ag NCs effect on biomass and metabolic activity of 24-h established biofilm of *S. aureus*, *E. coli* and *P. aeruginosa* were performed (Figure 15). Regarding the activity on *S. aureus* biofilm, FcCAR@Ag NCs showed a significant efficacy ($p < 0.05$) already at concentrations slightly higher respect to those active on the planktonic phase (11.7 μg/mL = 2 × MIC). Specifically, the effective percentage reductions of biofilm biomass (47%, 65%, 68%) and metabolic activity (46%, 71%, 74%) were detected with 11.7 μg/mL (2 × MIC), 23.4 μg/mL (4 × MIC) and 46.8 μg/mL (8 × MIC), respectively.

A lower effect of FcCAR@Ag NCs on *E. coli* and *P. aeruginosa* biofilm was observed. At doses equal to 8 × MIC, decreases of 54% and 62% of biomass and 39% and 37% of metabolic activity, respectively, were detected. However, it should be highlighted that *E coli* showed the lowest MIC values (2.9 μg/mL) compared to those of the other bacteria (5.8 μg/mL). Consequently, the dose of 8 x MIC corresponded to the dose of 4 x MIC for *S aureus* and *P.aeruginosa*.

**Table 4:** Antibacterial activity of FcCAR@Ag NCs (expressed as Ag concentration in μg/mL)

| Samples | *S. aureus* ATCC 6538 | | *S. aureus* (MRSA) ATCC 43300 | | *E. faecium* (VREfm) DSM 17050 | | *E coli* ATCC 10536 | | *E coli* DSM 105388 | | *P. aeruginosa* ATCC 9027 | |
|---|---|---|---|---|---|---|---|---|---|---|---|---|
| | MIC | MBC | MIC | MBC | MIC | MBC | MIC | MBC | MIC | MBC | MIC | MBC |
| FcCAR@Ag NCs | 5.8 | 11.7 | 5.8 | 23.4 | 5.8 | 46.7 | 2.9 | 2.9 | 5.8 | 5.8 | 5.8 | 5.8 |
| AgNO3 | 11.7 | 46.7 | NE[a] | NE[a] | NE[a] | NE[a] | 5.8 | 11.7 | NE[a] | NE[a] | NE[a] | NE[a] |
| FcCAR | -b | -b | -b | -b | -b | -b | -b | -b | -b | -b | -b | -b |

[a] N.E. Not evaluated

[b] No activity at the highest tested concentration

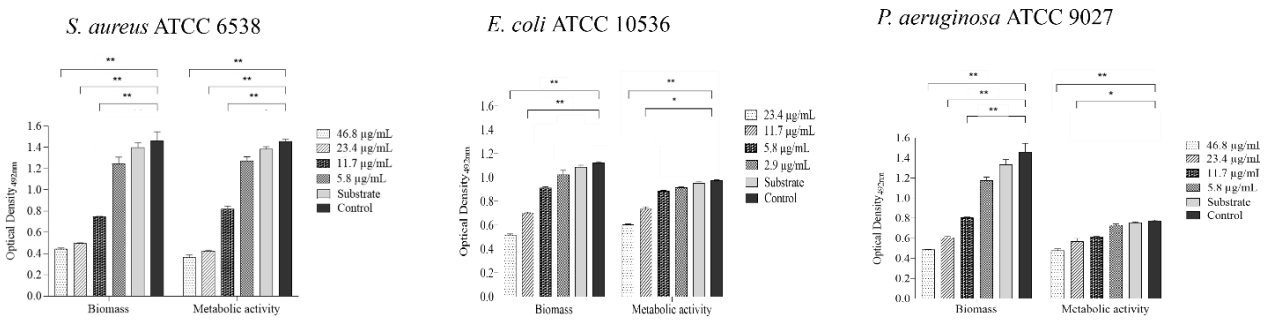


**Figure 16**. Effects of different concentrations (from MIC to 8 x MIC) of FcCAR@AgNCs on 24 h-biofilm of *S. aureus*, *E. coli* and *P. aeruginosa*. All data are presented as mean ± SD (* $p \leq 0.05$; ** $p \leq 0.01$).

## Screen-Printed Carbon Electrodes modified with graphene and Ferrocenyl-Carnosine

Nanohybrid composites based on the combination of metal nanoparticles, conductive polymers, metal oxides have been recently explored for the design of high performing electrochemical sensors [30,31]. In the framework of my PhD my attention was focused on the design of hybrid nanosystems based on carbon nanomaterials (CBNs) functionalized with β-cyclodextrins (βCD). CBNs thank to their large surface area, good electrical conductivity together with high mechanical strength have attracted great attention in electrochemical field. Moreover, their functionalization with βCD endows CBNs of further molecular recognition sites. Previously the Hg(II) electrochemical sensor obtained by the modification of screen-printed carbon electrodes (SPCEs) with carbon nanotubes-CD (CNT-βCD) supramolecular assembled with ferrocenylcarnosine (FcCAR) was developed in our lab [20]

In this thesis we propose a new electrochemical sensor based on graphene nanoplatform (rG) derivatized with Mono-6-deoxy-6-azido-β-cyclodextrin (CD) and assembled with FcCAR unit. rG provides a higher loading capacity compared to CBNs, thanks to its larger surface area. However, its hydrophobicity together with the ability to form irreversible agglomerate in water limits its application, therefore a suitable functionalization with cyclodextrins play a key role to overcome these issues [20], providing rGCD system with good biocompatibility and water dispersibility. Moreover, the GCD electrochemical sensing platform, takes advantages to the combination with FcCAR unit (Fig.15), which synthesis was described in literature [32], and an update is provided here. The obtained rGCD hybrid nanocomposite was characterized by TGA, SEM, XPS and Raman spectroscopy. Then the ability of rGCD/FcCAR modified SPCEs to behave like electrochemical sensor was investigated and a comparison with CNT- cβCD/FcCAR was carried out.

The chemical and structural modifications of carbon-based materials, such as graphene, play a crucial role in improving their processability and sensing performance. These modifications, often achieved through functionalization with macrocycles using click chemistry procedures, create suitable binding sites for the recognition of specific ligands [20]. This is significant as it enhances the material's ability to interact with target molecules, thereby improving its performance in various applications.

GCD nanoplatforms, with high affinity towards FcCAR, were obtained from commercial graphene oxide (GO) by a three-synthetic procedure (Fig. 17A).

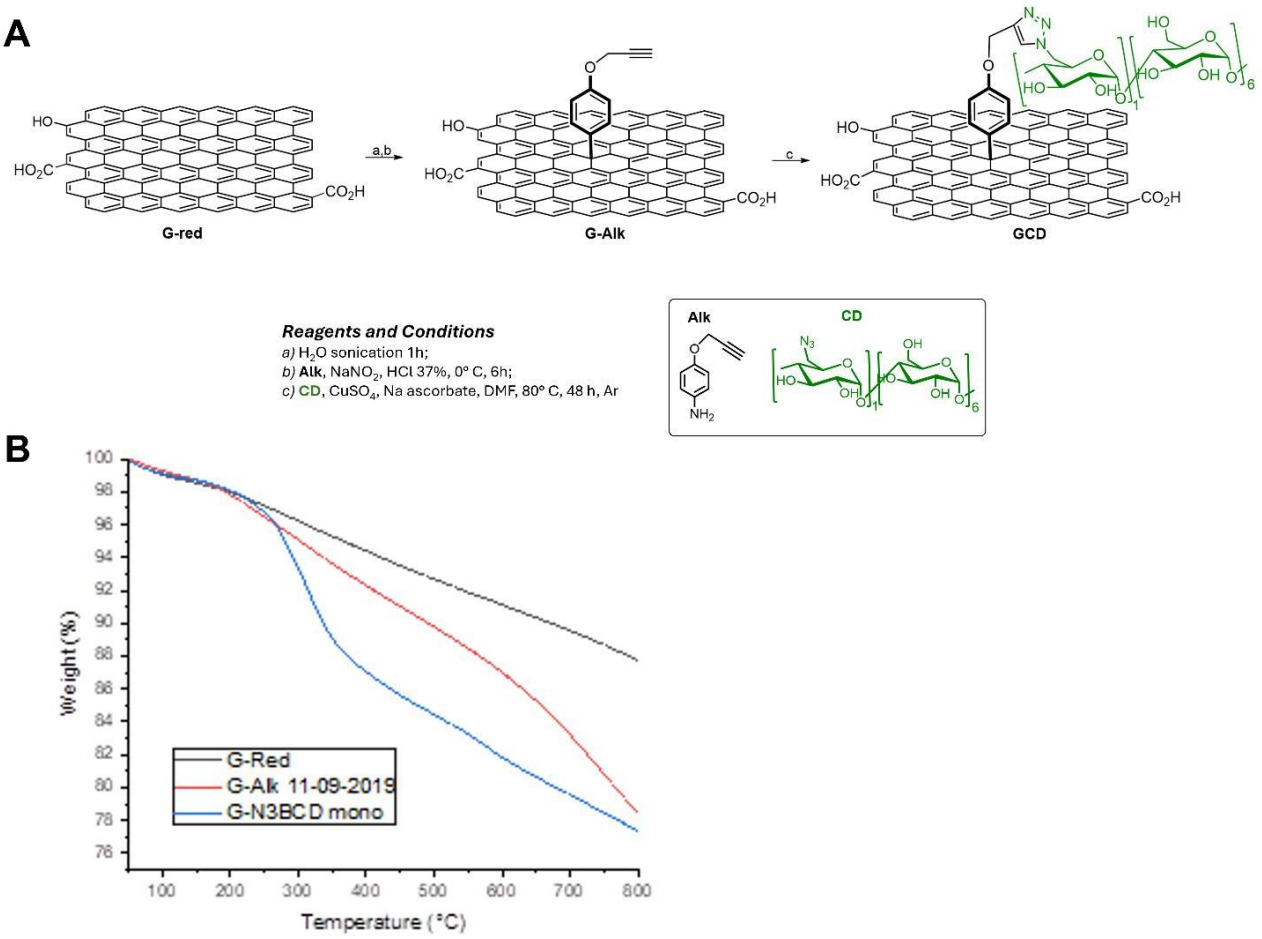


**Figure 17:** Schematic representation of (A) GCD and (B) TGA profiles of G-red (black line), G-Alk (red line) and GCD (blue line) under nitrogen flux.

GO was chemically reduced to G-red; this partial restoration of the $sp^2$ network improves the electrical properties of graphene, making it more suitable for electrochemical sensing applications. Subsequently, G-red was derivatized with an alkyne terminated group (G-Alk) [25], providing the anchorage sites for CD grafting. GCD nanosystem was obtained by a click chemistry reaction between the alkyne moiety on the G surface and the azide groups of mono-6-deoxy-6-azido-β-cyclodextrin (CD) [33]. Unambiguous evidence of the functionalization of the graphene platform was provided by TGA analysis (Fig. 15 B). G-red shows much higher thermal stability with a constant mass loss up to 800° C, while G-Alk displays a starting degradation point at 180° C, followed by a continuous degradation up to 800° C (Fig. 17B).

From the TGA thermogram, the amount of alkyne moiety grafted on graphene surface was found to be 0.37 mmol/mg (~5% weight loss, with respect G-Red residue @500°C). According to literature

data [40], the TGA profile of graphene decorated with CD shows a different thermal profile than the precursors (G-red and G-Alk). It exhibits two steps of weight loss: from 100 to 210 °C due to the loss of residual water and from 250 to 500 °C due to the loss of CD units (Fig. 17 B). The amount of CD grafted on GCD was established to be 44 µmol/mg (~5% weight loss, with respect G-Alk residue @500°C). The surface composition of carbon-based nanomaterials is an important factor influencing the sensor's electrochemical sensitivity. Thus, the elemental composition of the obtained samples (Table 5) was investigated by XPS survey spectra. For G-Alk, the slight percentage increase of O and N species in GCD proves the derivatization of the graphene with CD units, also confirmed by the increase of surface carbon oxidation and C-N bonds (Table 5, Fig. 16).

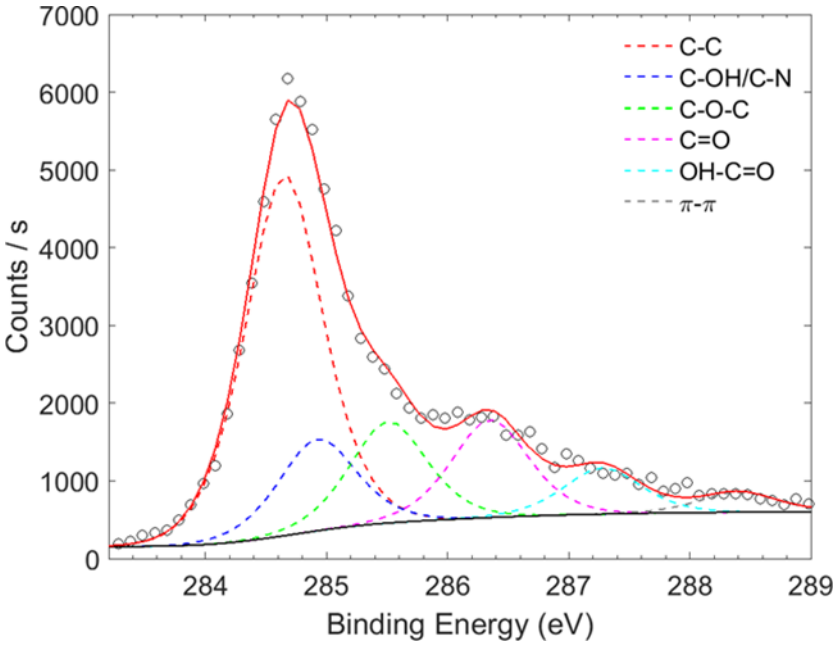


**Figure 18:** XPS C 1s high resolution spectra of the GCD sample deconvoluted using six Gauss-Lorentzian functions.

Moreover, a high compositional uniformity degree of GCD was observed by atomic species evaluation in different points, confirming the successful of the washing cycles to remove the unbonded materials from the platform. Raman spectroscopy also confirmed the derivatization of G-Alk with CDs.

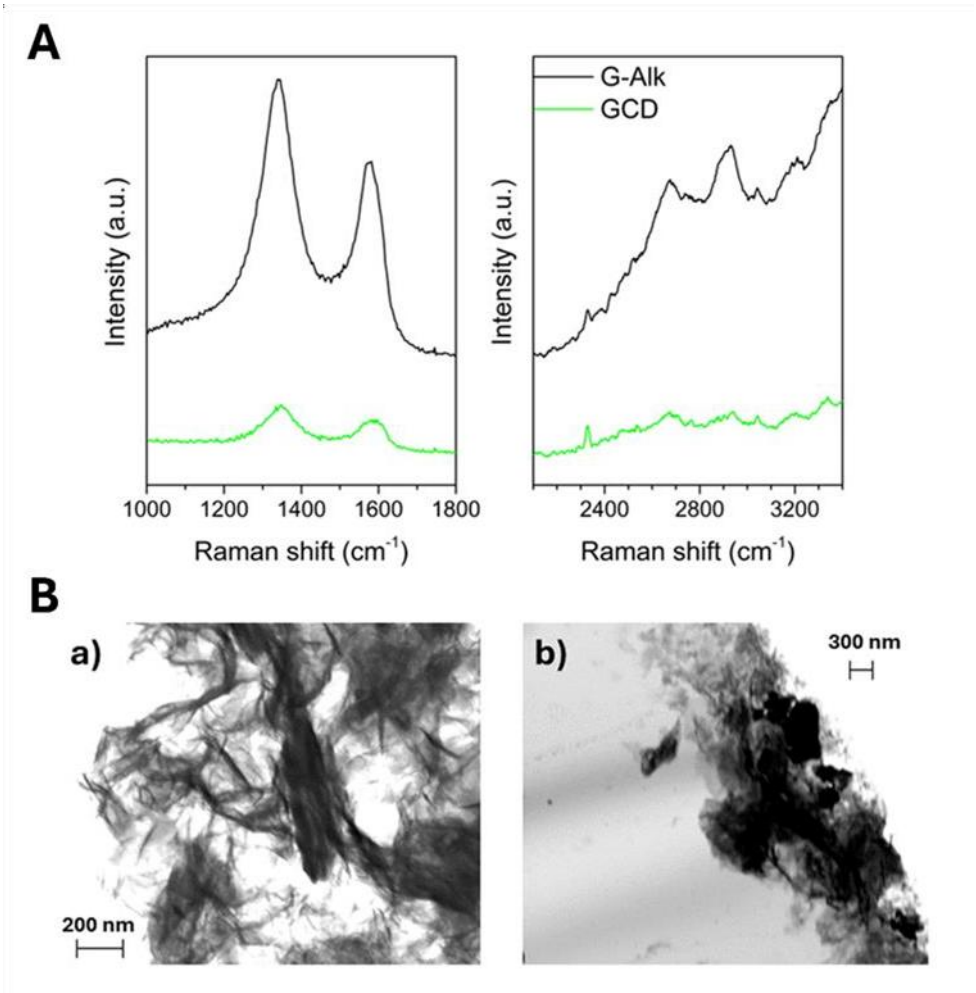


**Figure 19:** Raman spectra of G-Alk and GCD investigated samples(A). SEM images of G-Alk (Ba) and GCD (Bb).

The Raman spectra of G-Alk and GCD (Fig. 19A) show the typical bands of the carbon-based materials, namely G and D bands centred at about 1660 $cm^{-1}$ and 1380 $cm^{-1}$, respectively. The broadening and the shift of these bands towards a higher wavenumber are due to the graphene plane functionalization (GCD), which induces a size reduction of the in-plane sp2 domains. Moreover, the derivatization of the graphene surface is also proved by the D and G bands intensity decrease and the disappearance of both the G* band and second-order overtone 2D mode in the 2400–2700 $cm^{-1}$ range [34,35].

SEM images of G-Alk (Fig. 19B-a) and GCD (Fig. 19B-b) show well-defined edges and many thin layers of graphene. The G-Alk sample, in particular, exhibits homogeneous and quite smooth overlapped sheets, whereas GCD exhibits amorphous aggregates on the layer surface due to the functionalization with CDs.

**Table 5:** Surface elemental composition estimated by wide scan spectra, and the percentage of the carbon bonding configurations, estimated by deconvolving the HR C 1s spectra.

| Sample | C(%) | O(%) | N(%) | C-C (%) | C-OH/ C-N (%) | C-O-C (%) | C-C (%) | C=O (%) | OH-C=O (%) | π- π (%) |
|---|---|---|---|---|---|---|---|---|---|---|
| G-Alk | 85.4 | 11.1 | 3.5 | 56.1 | 12.6 | 16.1 | 56.1 | 9.0 | 4.7 | 1.5 |
| GCD (#1) | 82.0 | 13.7 | 4.3 | 50.3 | 12.8 | 14.1 | 50.3 | 13.6 | 6.4 | 2.8 |
| GCD (#2) | 80.8 | 14.3 | 4.9 | 52.1 | 13.3 | 13.7 | 52.1 | 13.9 | 5.1 | 1.9 |

**Electrochemical investigation**

GCD dispersion in DMF (1 µ; 3 mg $mL^{-1}$) was cast on the electrode surface, and the modified SPCE (SPCE/GCD) was dried under nitrogen atmosphere (80°C). Then, the electrochemical response was evaluated by Cyclic Voltammetry (CV) using $[Fe(CN)_6]^{3-}$ as the redox probe. Fig. 20 A shows the 30% amplification of the electrochemical signal by switching from SPCE to SPCE/GCD. The increase in electron transfer between potassium ferricyanide and the working electrode surface is due to the electrical conductivity of the GCD material, as well as demonstrating its deposition on the electrode surface. However, the electrode surface did not support further addition of conductive material, indicating saturation. A slight shift ($\Delta E_{a,p=}$ 0.028 V and $\Delta E_{c,p}$ = 0.009 V) occurs by switching from SPCE (0.216 V; 0.021 V *vs*. Ag/AgCl) to SPCE/GCD (0.188 V; 0.03 V *vs*. Ag/AgCl) that could be due to attractive interactions between the anionic $[Fe(CN)_6]^{3-}$ and functional groups on the electrode surface of SPCE/GCD.

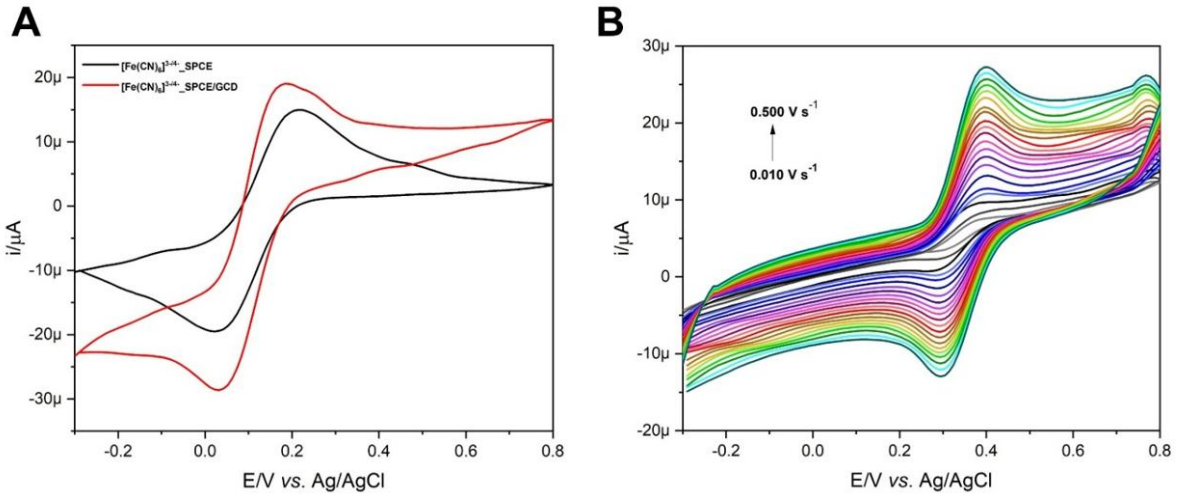


**Figure 20: A**) CVs of $[Fe(CN)_6]^{3-}$ (1 mmol $L^{-1}$) in KCl (0.1 mol $L^{-1}$) on bare SPCE (black line) and SPCE/GCD (red line). **B**) CVs of FcCAR (0.5 mmol $L^{-1}$) in KCl (0.1 mol $L^{-1}$) vs. scan rate (ν/ V $s^{-1}$) on SPCE/GCD.

The electrochemical behavior of FcCAR (0.5 mmol $L^{-1}$) in KCl (0.1 mol $L^{-1}$) on SPCE/GCD at 0.100 V $s^{-1}$ was investigated and compared with that obtained on bare SPCE. Fig. 21 shows the CVs of FcCAR on both SPCE and SPCE/GCD with a one-electron reversible redox process, similar to one occurred on SPCE/CNT-CD. The anodic ($E_{a,p}$) and cathodic ($E_{c,p}$) peaks of FcCAR on SPCE/GCD are at 0.395 V and 0.286 V (*vs*. Ag/AgCl), respectively. Comparing these potential values with those obtained on bare SPCEs, only the cathodic peak undergoes a slight cathodic shift as a result of functionalization of the electrode surface.

The electrochemical behavior of FcCAR was also studied in a wide range of scan rate ($0.01 \leq$ V $s^{-1} \leq 0.500$) on SPCE/GCD (Fig. 20B). The relationship between peak current and scanning rate provides information on whether the electrochemical process is controlled by adsorption or diffusion. The anodic ($i_a$) and cathodic ($i_c$) peak currents vary linearly with the scan rate ($\nu$) (Fig. 20 eqs. (1) and (2)), indicating that the redox process is mainly controlled by adsorption [38]

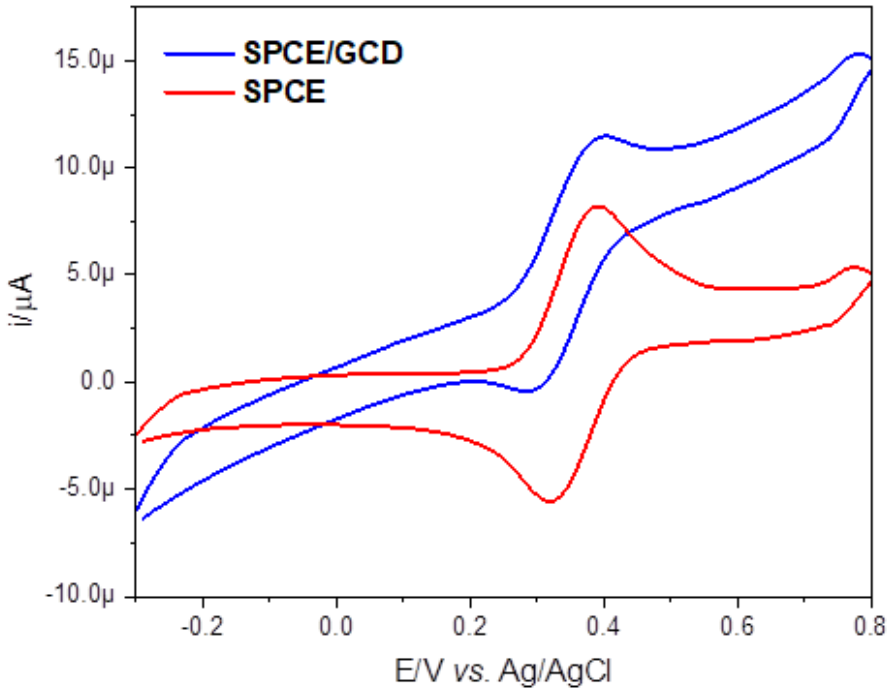


**Figure 21:** CV response (at 0.1 V $s^{-1}$) of FcCAR (0.5 mmol $L^{-1}$) in KCl (0.1 mol $L^{-1}$) on SPCE/GCD (blue line) and SPCE (red line).

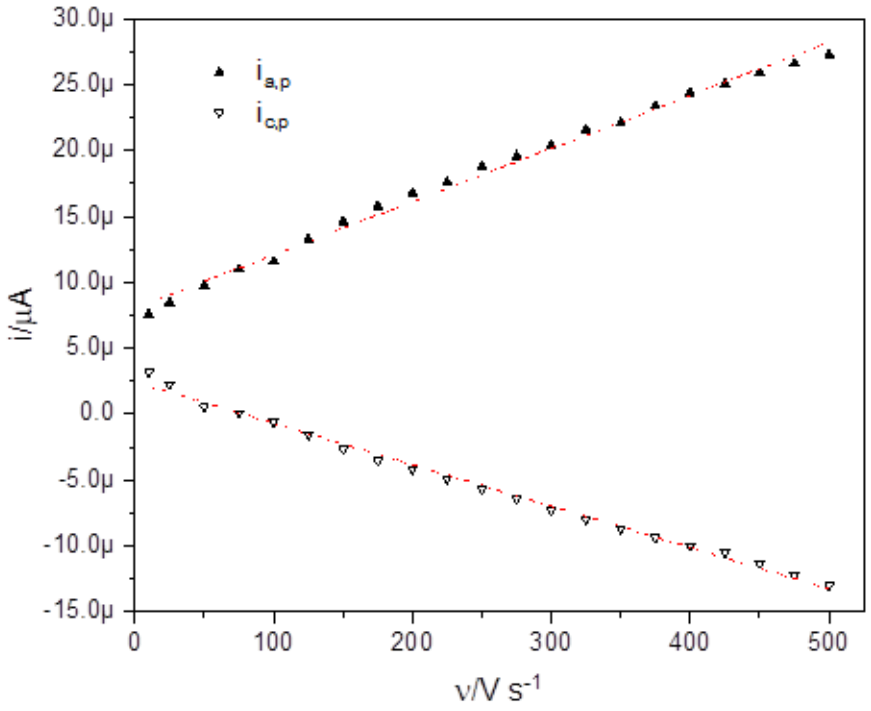


**Figure 22:** Dependence of anodic ($i_{a,p}$) and cathodic ($i_{c,p}$) peak currents on the scan rate (ν) for FcCAR (0.5 mmol $L^{-1}$) in KCl (0.1 mol $L^{-1}$) on SPCE/GCD. [39,40]

$$i_{a,p}\ (\mu A) = 4.031\ \nu\ (V\ s^{-1}) + 8.081,\ R^2 = 0.993 \quad (1)$$

$$i_{c,p}\ (\mu A) = -3.141\ \nu\ (V\ s^{-1}) + 2.452,\ R^2 = 0.994 \quad (2)$$

One we had analyzed the electrochemical behavior of the SPCE/GCD/FcCAR, voltammetric response of FcCAR in KCl (0.1 mol $L^{-1}$) in the presence of Mn(II) ($0.17 \leq$ nmol $L^{-1} \leq 417$) was evaluated by CV (at 0.100 V $s^{-1}$, Fig. 21), and Differential Pulse Voltammetry (DPV, see inset of Fig. 23).

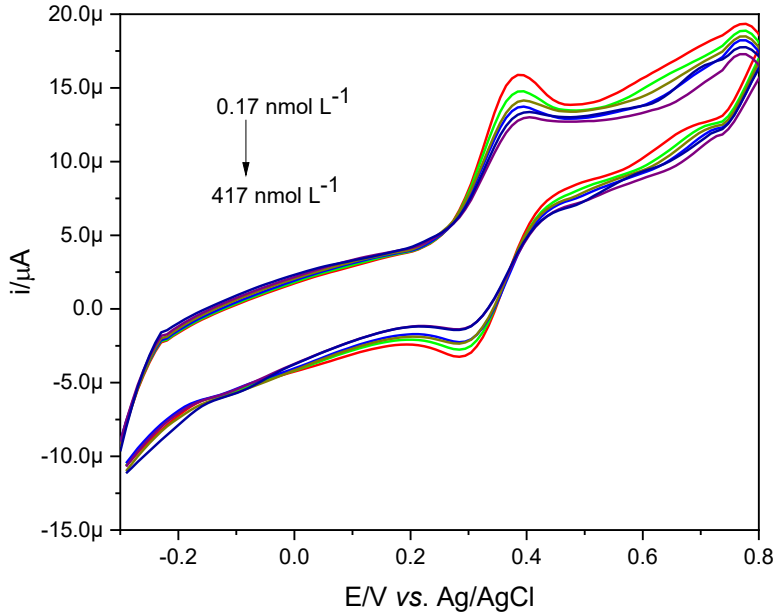


**Figure 23:** CVs of FcCAR (0.5 mmol $L^{-1}$) in KCl (0.1 mol $L^{-1}$) at different Mn(II) concentration on SPCE/GCD

While the potential values do not change in the presence of Mn(II), confirming that the $Fc/Fc^{+}$ redox couple is the responsible moiety to the redox process, the anodic peak currents linearly decrease as the metal concentration increases. The linear concentration range ($0.17 \leq$ nmol $L^{-1} \leq 48$) is shown in Fig.24. The Limit of Detection (LOD) and Limit of Quantification (LOQ) were determined according to the $3\sigma$ $s^{-1}$ and $10\sigma$ $s^{-1}$ approaches [41], where σ is the standard of seven independent measurements of a blank sample and s is the slope of the calibration plot (Fig. 24). LOD and LOQ were found to be 0.69 nmol $L^{-1}$ and 2.3 nmol $L^{-1}$, respectively, with a sensitivity of 0.20 μA/nmol $L^{-1}$. Comparing other LOD values, reported in the literature [42-53] (Table 6) this system (SPCE/GCD/FcCAR) shows high performance to detect Mn(II) in aqueous solutions.

**Table 6**: Comparisons with the literature data (type of electrode, linear range and LOD values) reported over the past 10 years

| Electrode | Linear range | LOD | Ref. |
|---|---|---|---|
| SPCE/GCD/FcCAR | 0.17 – 48 nmol $L^{-1}$ | 0.69 nmol $L^{-1}$ | This work |
| Pd | 455 nmol $L^{-1}$ - 10.9 μmol $L^{-1}$ | 334 nmol $L^{-1}$ | [42] |
| Pyrolytic graphite | 12.3 nmol $L^{-1}$ -0.1 mol $L^{-1}$ | 4.78 nmol $L^{-1}$ | [43] |
| Pt | 91-910 nmol $L^{-1}$ | 16.3 nmol $L^{-1}$ | [44] |
| Au | 0.11-0.32 μmol $L^{-1}$ | 31 nmol $L^{-1}$ | [45] |
| Additive Manufactured Electrode | 9.1 nmol $L^{-1}$ – 2.7 μmol $L^{-1}$ | 1.6 nmol $L^{-1}$ | [46] |

| | | | |
|---|---|---|---|
| GC | 2.5-200 µg $L^{-1}$ | 0.63 µg $L^{-1}$ | [47] |
| GC | 1-7 µmol $L^{-1}$ | 0.43 µmol $L^{-1}$ | [48] |
| Pt | 91 nmol $L^{-1}$-1.82 µmol $L^{-1}$ | 10.1 nmol $L^{-1}$ | [49] |
| SPE / Au NPs / rGO/$Fe_3O_4$ NPs / L-cysteine | 0.5–300 µg $L^{-1}$, 62–1500 µg $L^{-1}$ | 34 µg $L^{-1}$, 1550 µg $L^{-1}$ | [50] |
| Edge plane pyrolytic graphite electrode IIP/MWCNT-Chit-IL/GCE | 2-9 µmol $L^{-1}$ | 0.15 µmol $L^{-1}$ | [51] |
| Indium tin oxide | 5-500 µg $l^{-1}$ | 0.5 µg $l^{-1}$ | [52] |
| Gold electrodes | - | 4.64 µmol $L^{-1}$ | [53] |

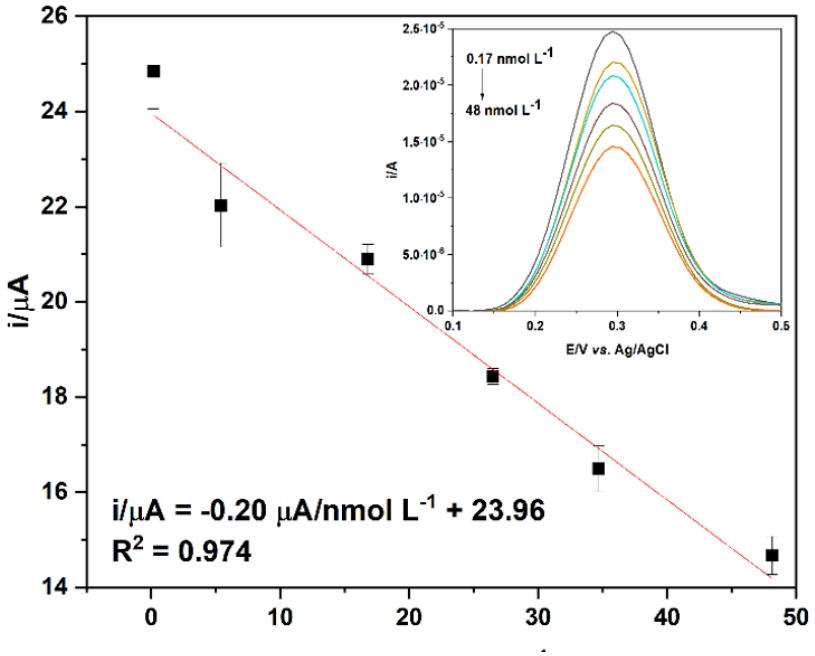


**Figure 24:** Linear range of the anodic peak ($i_{a,p}$) of FcCAR vs. Mn(II) concentration ($0.17 \leq$ [Mn(II)]/nmol $L^{-1} \leq 48$) on SPCE/GCD. The inset shows the respective DPV scans.

# CONCLUSIONS

The synthesis of amphiphilic dipeptide derived from natural carnosine (FcCAR) was optimized and its properties were investigated.

FcCAR was used for the synthesis of silver nanocluster: the unique properties of FcCAR ensured the appropriate reduction of silver ions in mild conditions and the stabilization of formed nanoclusters by carnosine functional groups. The direct conversion of silver ions into blue-emitting silver nanocluster was confirmed by the comprehensive study of them optical properties and by electron transmission microscopy (TEM). Their colloidal stability was evaluated by zeta potential (ζ) and dynamic light scattering (DLS) measurements. The biological profile of as produced silver nanoclusters (FcCAR@Ag NCs) showed a potent antibacterial effect against all tested microorganisms including the methicillin resistant Staphylococcus aureus (MRSA) The ability of FcCAR@Ag NCs to killing S. Aureus and E. Coli, resulted up to one orders of magnitude greater than silver nitrate alone.

FcCAR was investigated to prepare the graphene-cyclodextrin/ferrocenyl-carnosine (GCD/FcCAR) supramolecular assembly. GCD/FcCAR nanoassembly was used to modify Screen-Printed Carbon Electrode (SPCE) for the electrochemical detection of Mn(II).

GCD was synthesized by a multistep process involving the reduction of commercial GO, followed by a treatment with diazonium compound to insert alkyne terminated groups onto the graphene surface (G-Alk). A subsequent click chemistry reaction was performed to covalent bond graphene platform to CDs. The success of the synthetic route was confirmed by TGA, SEM, Raman spectroscopy and XPS analysis. The electrochemical output of engineered SPCE with GCD was studied by Cyclic Voltammetry (CV) using $[Fe(CN)_6]^{3-}$ as redox probe and compared to the ones of bare SPCE. The findings highlight the ability of GCD on SPCE to improve the electric current response (by 30%) compared with the bare SPCE.

At the same time, the metal-ion complexing ability and analytical properties of FcCAR were studied in the absence and presence of Mn(II) using CV and DPV techniques. The latter was employed to calculate the Limit of Detection (LOD) and Limit of Quantification (LOQ) in the metal concentration range ($0.17 \leq [Mn(II)]/nmol\ L^{-1} \leq 48$). LOD and LOQ values were found to be 0.69 nmol $L^{-1}$ and 2.3 nmol $L^{-1}$, respectively, with a sensitivity of 0.20 μA/nmol L-1. The LOD value obtained is being one of the lowest reported in literature.

# MATERIALS AND METHODS

FerrocenylCarnosine (FcCAR ; M.W. 438.27 g/mol) was synthesized via coupling method. All the reagents and solvents, unless otherwise indicated, are purchased by Sigma-Aldrich (Milan, Italy): Ferrocenecarboxylic acid (Fc; M.W. 230.04 g/mol); N-Hydroxysuccinimide (NHS; M.W. 115.09 g/mol); N-(3-Dimethylaminopropyl)-N′-ethylcarbodiimide hydrochloride (EDCI or EDAC; M.W. 191.70 g/mol); Acetonitrile (Fluka ; ≥99.0%(GC)); Dichloromethane (puriss. p.a., ACS reagent, reag. ISO, ≥ 99.9% (GC)); Silica gel (J. T. Baker; 0.063 - 0.200 mm (70 - 230 mesh ASTM) « BAKER ANALYZED »); L-Carnosine (CAR; M.W. 226.23 g/mol); (DM); Methanol (≥99.8% (GC), ACS reagent, suitable for HPLC, reag. Ph. Eur., USP/NF, reag. ISO); Dry silver-nitrate ($AgNO_3$; 99.9999% trace metals basis; M.W. 169.87 g/mol), L (+) ascorbic-acid (AA; M.W. 176.13 g/mol), Sodium Hydroxide (NaOH; reagent grade, ≥98%, pellets (anhydrous); M.W. 40.00 g/mol).

## Characterization

UV/Vis characterization was performed on a model Jasco V-730 using 1 cm path length quartz cells at r.t. ≅ 25 °C. Steady state fluorescence spectroscopy Steady-state fluorescence measurements were performed on a Jasco model FP-750 spectrofluorimeter by using a 1 cm path length quartz cell.

Fluorescence lifetime decay curves of FcCar-substrate and FcCar-AgNCs were obtained using a time-resolved confocal fluorescence MicroTime200 microscope system from PicoQuant (Berlin, Germany). The measurements were performed under 405 nm excitation laser (PicoQuant diode laser LDH-D-C-405, 40 MHz).

The absolute quantum yield (QY) was acquired under an excitation of 400 nm via a JASCO spectrofluorometer FP-8600 equipped with an integrating sphere accessory (ILF-835) in a 3 mm thickness quartz cuvette.

The mean diameter, width of distribution (polidispersity index, PDI) and ζ-potential were measured through photon correlation spectroscopy (PCS) by a Zetasizer Nano ZS (Malvern Instrument, Malvern, U.K.) at 25°C in ultrapure water. The measurements were performed at a 173° angle with respect to the incident beam at 25 ± 1 °C for each dispersion. The deconvolution of the measured correlation curve to an intensity size distribution was achieved by using a non-negative least-squares algorithm. The ζ-potential values were determined using a Zetasizer Nano ZS Malvern Instrument equipped with a He−Ne laser at a power P = 4.0 mW and λ = 633 nm. The results are reported as the mean of three separate measurements on three different batches ± the standard deviation (SD).

Transmission Electron Microscopy images of samples were performed in Servicio de Microscopía

Electrónica del Centro de Biología Molecular "Severo Ochoa" in a Jeol JEM-1010 microscope equipped with a CMOS 4K × 4K, F416 de TVIPS camera.

**Synthesis of Ferrocenylcarnosine (FcCAR)**

Ferrocenecarboxylic acid (1 g; 4.34 mmol), NHS (500 mg; 4.34 mmol) and EDCI (850 mg; 5.47 mmol) were dissolved in anhydrous acetonitrile (5 mL) and stirred overnight at room temperature. After roto-evaporation, the crude mixture was purified by silica column chromatography with DCM as eluent, to obtain 2,5-dioxopyrrolidin-1-yl ferrocenoate (FcNHS; 1.16 g; 3.54 mmol; 82% yield). To obtain FcCAR, a solution of FcNHS (530 mg; 1.63 mmol) dissolved in DMF (10 mL) was slowly added to a cold solution of Carnosine (407 mg; 1.79 mmol) and NaHCO3 (126 mg; 1.49 mmol) in 1:1 H2O/DMF (50 mL) under stirring. The reaction mixture was stirred at room temperature for 20 h. The crude mixture was purified by silica gel column chromatography from $CH_2Cl_2$ to $CH_2Cl_2$/MeOH (1:1) as gradient eluent, to obtain Ferrocene-carnosine (FcCAR) (536 mg, 75% yield). $^1$H-NMR ($D_2O$, 500 MHz): δ 2.58–2.51 (m, 2H), 2.95 (dd, 1H, J=15.4Hz, J=8.6Hz), 3.12 (dd, 1H, J=15.4Hz, J=4.6Hz), 4.52 (t, 2H, J=2.0Hz), 4.45 (dd, 1H, J=4.6Hz, J=8.6Hz), 4.21 (s, 4H), 3.51 (dt, 2H, J=2.0Hz, J=6.3Hz), 4.75-4.71 (m, 2H), 6.94 (s, 1H), 7.74 (s, 1H). $^{13}$C-NMR ($D_2O$, 125 MHz): δ 28.1, 35.2, 35.7, 48.8, 54.6, 68.2, 68.3, 70.0, 71.4, 71.5, 73.6, 116.8, 131.3, 134.3, 173.2, 173.8, 177.1. ESI-MS (m/z): 439.10 detected as $[MH]^+$ species cld for $C_{20}H_{22}FeN_4O_4$ (m/z: 438.099).

**Synthesis of Silver Nanocluster**

Before usage all the glassware were carefully cleaned with aqua regia ($HCl/HNO_3$, volume ratio 3:1) and rinsed thoroughly with ultrapure water. Ligand stock solutions (100 mM; 46 mg/mL), $AgNO_3$ (5 mM) Ascorbic Acid (AA, 50 mM), NaOH (1 M) were prepared using ultrapure water. The FcCAR@Ag NCs were prepared according to the experimental conditions described in Entry 1. *Entry 1*: to the FcCAR stock solution (3 mL, 0.3 mmol), pre-heated to 80 °C under stirring, the $AgNO_3$ stock solution (1 mL, 0.005 mmol) was added. After 5 minutes AA (50 mM, 0.02 mL) was added, and the pH was corrected by addition of 0.5 mL of NaOH 1 M. The mixture was stirred for 4 hours at 80 °C and then cooled to room temperature. The FcCAR@Ag NCs water solution was stored at 4 °C and used without purification. The nominal contents of FcCAR and $Ag^+$ in FcCAR@Ag NCs solution are 66 mM (30.36 mg/mL) and 1.1 mM (119 µg/mL) respectively.

**Minimal inhibitory concentration and minimal bactericidal concentration**

The microorganisms used in this study were *S. aureus* ATCC 6538, methicillin resistant *S. aureus* (MRSA) ATCC 43300, vancomycin resistant *Enterococcus faecium* (VRE) DSM 17050, *Escherichia coli* ATCC 10536, ESBLs producing *E. coli* DSM105388 and *P. aeruginosa* ATCC 9027. Minimal Inhibitory Concentration (MIC) and the Minimal Bactericidal Concentration (MBC) of the FcCAR@AgNCs (containing $AgNO_3$ = 187 μg/mL), were performed according to the guidelines of the Clinical and Laboratory Standards Institute (CLSI) [47], with some modifications. The samples were twofold diluted in 96-well round-bottomed using MHB and overnight bacterial cultures were inoculated to yield a final concentration of $5 \times 10^5$ CFU/mL. After incubation at 37 °C for 24 h, the MBC was determined by seeding 20 μL from all clear wells onto Muller Hinton agar and incubated at 37 °C for 24 to 48 h. The MBC was defined as the lowest concentration that killed 99.9% of the inoculum. The data from at least three replicates were evaluated, and modal results were calculated.

**Effect on preformed 24 h-biofilms**

Overnight cultures grown in TSB or TSB + 1% glucose were standardized to $1 \times 10^6$ CFU/mL and were inoculated (100 μL) in 96-well polystyrene flat-bottomed microtitre plates. After incubation for 24 h at 37˚C, the planktonic bacterial growth was dislodged and the wells were washed with sterile PBS and filled with twofold dilutions of samples, ranging from the MIC to a 8-fold the MIC (referred to the values reported in Table 2). After incubation for 24 h at 37˚C, the effects on: *i)* biofilm biomass and *ii)* biofilm metabolic activity were estimated as follows.

**Biofilm biomass**. The planktonic growth was dislodged, and each well was washed with PBS, dried, stained with 0.1% safranin and then washed with water. The biofilm biomass was eluted in acetic acid 30% (v/v) and the $OD_{492}$ was quantified.

**Biofilm metabolic activity**. The planktonic growth was dislodged and, after washing, each well was treated with the Cell Proliferation Kit II XTT (Roche Diagnosis, Mannheim, Germany) as previously reported [34]. This assay is based on the metabolic reduction of a tetrazolium salt [2,3-bis[methyloxy-4-nitro-5-sulfophenyl]-2H-tetrazolium-5carboxanilide carboxanilide (XTT)] to a coloured water-soluble formazan derivative. Briefly, each well was filled with the XTT solution (final concentration 0.3 mg/mL) for 5 h at 37˚C and the formazan derivative was measured spectrophotometrically at 492 nm. The reduction of biofilm biomass and biofilm metabolic activity was estimated using Eq 1:

$$[100 - (\frac{OD_{492}\ of\ treated\ well}{mean\ OD_{492}\ of\ control\ well})]\ x\ 100$$

**Statistical analysis**

Results were expressed as the mean ± standard deviation from three experiments. A two-way analysis of variance (ANOVA) was used to determine significant differences between the samples after treatment. Multiple comparisons were performed among groups by the Bonferroni correction test. The results with a *p*-value <0.05 were considered statistically significant.

**Synthesis of GCD**

Alkyne-terminated graphene (G-Alk) was synthetized as reported [25] and the amount of alkyne group grafted on the graphene platform was computed, by TGA, to be ∼5 wt % corresponding to∼0.37 mmol/g. The mono-6-deoxy-6-azido-β-cyclodextrin (CD) was obtained following the method described in [35].

G-Alk (270 mg, 0.175 mmol of Alk moiety) was dispersed in 15 mL of DMF, by sonication treatment. Then, CD (229.3 mg, 0.175 mmol), $CuSO_4$ (28 mg, 0.175 mmol) and sodium ascorbate (45 mg, 0.227 mmol) were added, and reaction was refluxed at 80° C for 48 h, under argon flow (Fig. 2A). The mixture was cooled at r.t., diluted with MqW and centrifugated at 4500 rpm for 25 min. The precipitate was collected and resuspended in MqW: MeOH (2:1) mixture and sonicated for 20 min, followed by an additional centrifugation step for 35 min at 4500 rpm. The washing step was repeated one more time. GCD was lyophilizate and 288 mg of product was obtained. From TG analyses, functionalization degree of GCD was evaluated to be around 5%, corresponding to 44 μg/mg of CD on G-Red.

**Voltammetric equipment and measurements**

All electrochemical measurements were carried out in KCl (0.1 mol $L^{-1}$) aqueous solutions (rt) using a PC-controlled electrochemical workstation with a three-electrode cell configuration (Metrohm DropSens Screen-Printed Electrodes (SPEs), DRP-DSC4MM 72098), which is connected to a μAutolab potentiostat-galvanostat type III (Eco Chieme) with an IME663 interface. Screen-Printed Carbon Electrodes (SPCEs), consisting of carbon- working, -counter electrodes and Ag/AgCl reference electrode, were used. The electrode surface was further modified by drop casting 1μL of a homogeneous dispersion of GCD in DMF (3 mg $mL^{-1}$), obtained by probe sonication treatment (5

min, 50% power), and drying the modified SPCEs (SPCE/GCD) at 80°C under DMF atmosphere (for at least 1h). Voltammograms were processed with General Purpose Electrochemical System (GPES) software, version 4.9 (Eco Chemie B.V.). Voltammetric response of SPCE/GCD was assessed by Cyclic Voltammetry (CV), using $[Fe(CN)_6]^{3-}$ (1 mmol $L^{-1}$) in KCl solution (0.1 mol $L^{-1}$), performed from -0.3V to +0.8V (vs. Ag/AgCl) at 0.1 $Vs^{-1}$. The electrochemical behavior of FcCAR (0.5 mmol L-1) in KCl solution (0.1 mol L-1) at different scan rates (0.010, 0.025, 0.050, 0.060, 0.075, 0.100, 0.125, 0.150, 0.175, 0.200, 0.225, 0.250, 0.275, 0.300, 0.325, 0.350, 0.375, 0.400, 0.425, 0.450, 0.475, 0.500Vs-1) was investigated on modified SPCEs from 0V to +0.8V (vs. Ag/AgCl). The electrochemical activity of FcCAR was also studied in the presence of $Mn^{2+}$ ($0.17 \leq$ nmol $L^{-1} \leq 417$) by Cyclic Voltammetry (CV), performed at 0.100 V $s^{-1}$ with a step potential of 0.010V, and Differential Pulse Voltammetry (DPV) as follows: potential step and amplitude equal to 0.010V and 0.1V, respectively. CV and DPV experiments were carried out in the following potential range ($-0.3 \leq E/V \leq 0.8$, vs. Ag/AgCl).

# Chapter 2

## MAGNETO AND/OR PLASMONIC NANOSTRUCTURES BASED ON SPIONS, GOLD AND HYALURONIC CYCLODEXTRIN DERIVATIVES

During my PhD research activity, the cyclodextrin-functionalized Hyaluronic Acid (HA-CD, Figure 29) was developed with the aim to create an integrated stimuli-responsive nanoplatform, as a drug delivery system. To achieve this goal the ability of HA-CD to entrap pharmaceutical ingredients was investigated by in vitro and in vivo experiments. Diclofenac, an anti-inflammatory drug was selected as model drug.

Additionally, ability of HA-CD to produce and to stabilize Gold Nanoplarticles (Au NPs) was investigated. The presence of hydroxyl groups and hemiacetal functionalities in HA-CD avoided the use of classical reducing agents in the synthesis of Au NPs, with the method of seeding growth [54]. The entrapment of superparamagnetic nanoparticles was achieved by the means of phase transfer method. The interactions of oleic acid units with CD cavities promoted the transfer of magnetic nanoparticles in aqueous phase. The main focus is centered on superparamagnetic nanoparticles, (SPIONs), because they are highly investigated in the biomedical field due to their magnetic targeting capacity which makes them suitable in the field of imaging and drug delivery, combined with their biocompatibility, bioavailability and hyperthermic properties. Core-shell bimetallic derivatives with gold have also recently been considered. Core-shell, as they are called, have a magnetic "core" and an external gold shell. The combination with gold gives the material SERS and plasmonic properties and improves the hyperthermal properties. The surface functionalization of a magnetic core with a gold-shell has enabled the creation of diverse nanocomposites that possess improved, complementary, even novel properties. Specifically, the gold coating onto magnetic NPs endows them of unique magnetic and optical properties ensuring biocompatibility, especially for photothermal therapy [55].

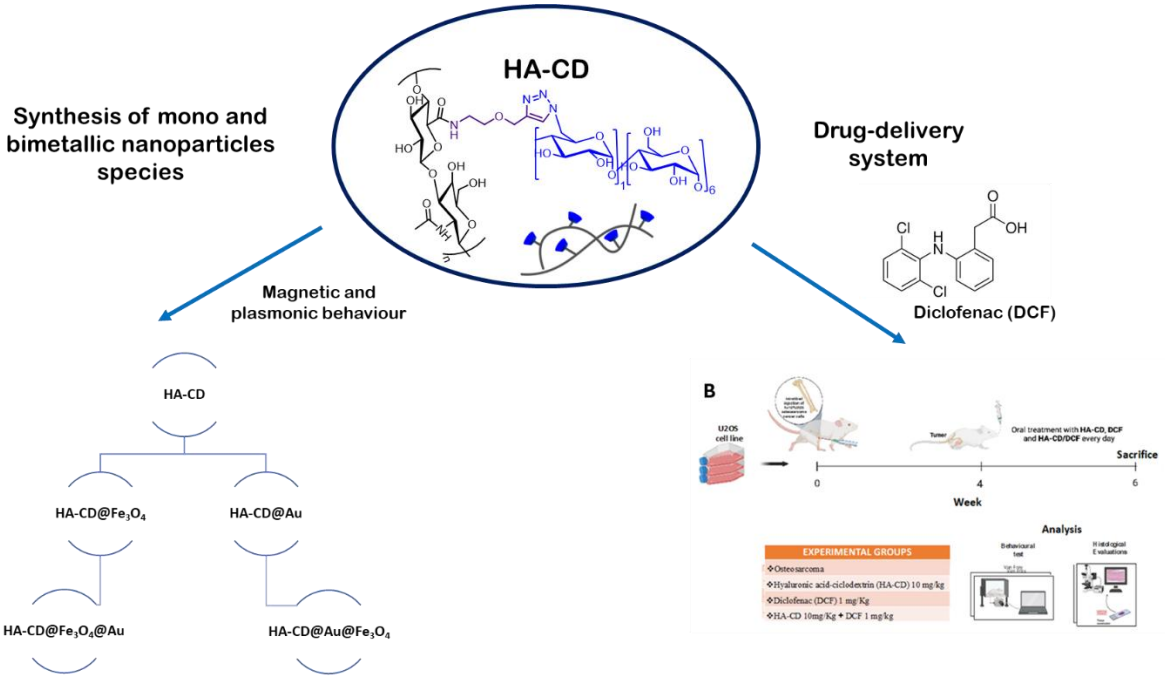


**Figure 29:** Overview of HA-CD applications

# Development of HA-CD Drug Delivery System

HA-CD was synthesized by a click chemistry two-step procedure previously reported [56]. Hyaluronic acid appropriately modified with an alkyl group and reacted with the azido modified β-cyclodextrin, according to the synthetic procedure described in figure 30. The degree of substitution of HA-CD was estimated by $^{1}H$ NMR analysis (DS 21%).

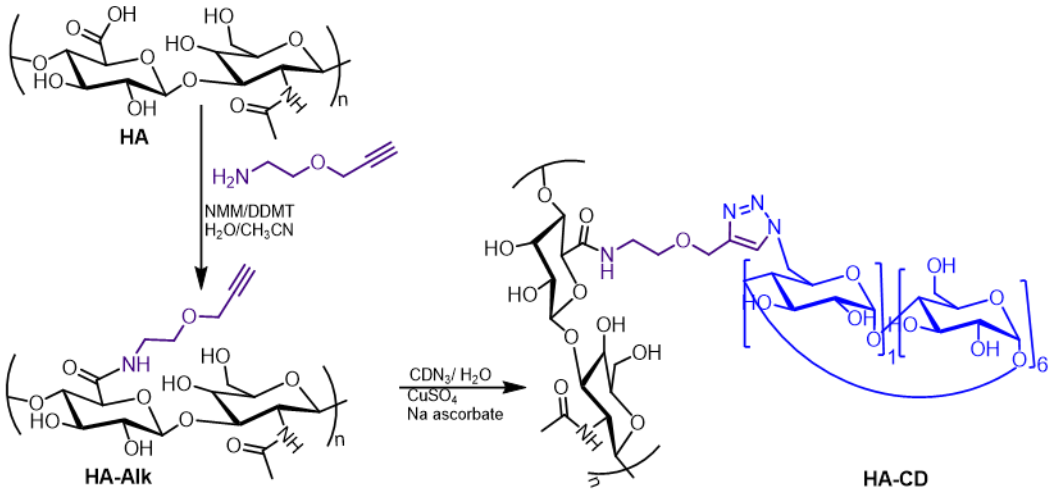


**Figure 30**: HA-CD synthesis

Diclofenac (DCF) was entrapped in HA-CD by hydration of an organic film and the stability of DCF/HA-CD nanosystem was investigated by UV-vis analysis (Fig.31). The DCF peak at 275.5 nm shifts slightly and becomes more intense when it is entrapped into HA-CD. No significant change of absorbance were observed upfront to 2 weeks.

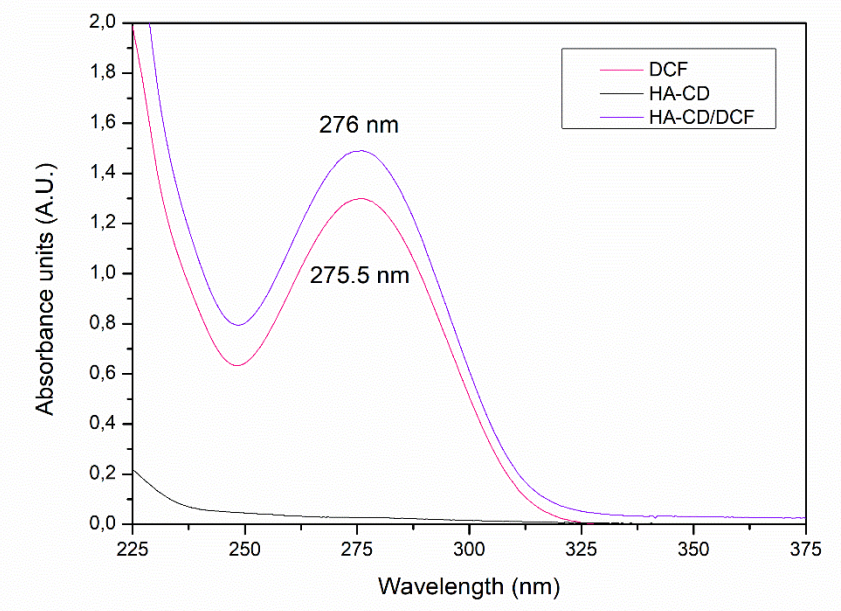


**Figure 31:** UV-vis spectra of HA-CD (red line; 0.16 mg/mL), DCF (fuchsia line; 100 μM), HA-

CD/DCF (HA-CD 0.16 mg/mL; DCF 100 µM, blue line); d= 1cm

The DCF release profile (Figure 32) was evaluated by UV-Vis analyses. After 92 hours, 75 % of DCF was released.

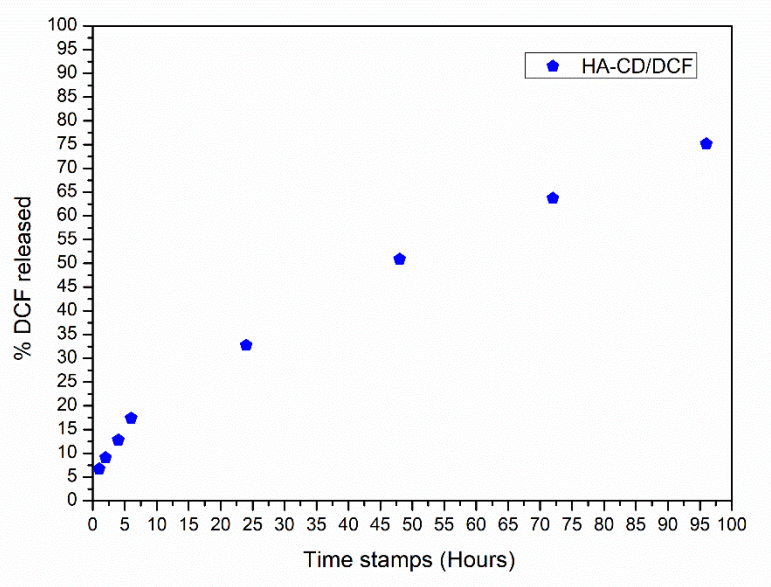


**Figure 32:** Release profile of DCF

To identify whether treatment with HA-CD could influence the longevity of the animals in the 24 hours, the survival of the animals at the end of the test was assessed. 24 hours after intra-articular injection of HA-CD (dosage 20 mg/mL), all animals had survived (Figure 33).

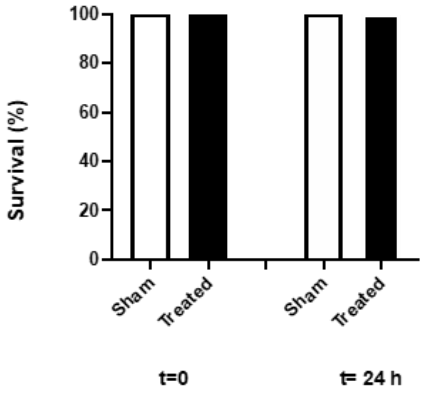


**Figure 33:** Survival assessment

From the periodic 24-hour observation of the animals, no clinical signs and no mortality were observed in all experimental groups until the end of the experiment (Table 7).

**Table 7:** Clinical signs

| Experimental Groups | Numbers | Doses | Mortality | Clinical Signs* | | | | | | | | | | | | | |
|---|---|---|---|---|---|---|---|---|---|---|---|---|---|---|---|---|---|
| Hours | | | 24 | 1 | 2 | 3 | 4 | 5 | 6 | 7 | 8 | 9 | 10 | 11 | 12 | 13 | 14 |
| Sham | 1 | * | 0 | 0 | 0 | 0 | 0 | 0 | 0 | 0 | 0 | 0 | 0 | 0 | 0 | 0 | 0 |
| | 2 | * | 0 | 0 | 0 | 0 | 0 | 0 | 0 | 0 | 0 | 0 | 0 | 0 | 0 | 0 | 0 |
| | 3 | * | 0 | 0 | 0 | 0 | 0 | 0 | 0 | 0 | 0 | 0 | 0 | 0 | 0 | 0 | 0 |
| | 4 | * | 0 | 0 | 0 | 0 | 0 | 0 | 0 | 0 | 0 | 0 | 0 | 0 | 0 | 0 | 0 |
| | 5 | * | 0 | 0 | 0 | 0 | 0 | 0 | 0 | 0 | 0 | 0 | 0 | 0 | 0 | 0 | 0 |
| HA-CD | 1 | 20 mg/ml | 0 | 0 | 0 | 0 | 0 | 0 | 0 | 0 | 0 | 0 | 0 | 0 | 0 | 0 | 0 |
| | 2 | 20 mg/ml | 0 | 0 | 0 | 0 | 0 | 0 | 0 | 0 | 0 | 0 | 0 | 0 | 0 | 0 | 0 |
| | 3 | 20 mg/m | 0 | 0 | 0 | 0 | 0 | 0 | 0 | 0 | 0 | 0 | 0 | 0 | 0 | 0 | 0 |
| | 4 | 20 mg/ml | 0 | 0 | 0 | 0 | 0 | 0 | 0 | 0 | 0 | 0 | 0 | 0 | 0 | 0 | 0 |
| | 5 | 20 mg/ml | 0 | 0 | 0 | 0 | 0 | 0 | 0 | 0 | 0 | 0 | 0 | 0 | 0 | 0 | 0 |
| * Clinical signs evaluated: Changes in skin and fur, eyes and mucous membranes, and also respiratory, circulatory, autonomic and central nervous system, and somatomotor activity and behaviour pattern. Attentions should be directed to observations of tremors, convulsions, salivation, diarrhoea, lethargy, sleep and coma. | | | | | | | | | | | | | | | | | |

The body weight of the animals was measured at the beginning of the test (on day 0), and on day 1 after administration. No major differences were observed in body weight changes in all experimental groups, as shown in Table 8.

**Table 8:** Body weight

| SD Rats | HA-CD | Weight (gr) | Weight (g) 24 hours | Δ weight | mean |
|---|---|---|---|---|---|
| | 1 | 250 | 224 | 4,1 | 8,3 |
| | 2 | 240,3 | 238 | 12,7 | |
| | 3 | 228,1 | 233 | 10,8 | |
| | 4 | 235 | 239,4 | 9,8 | |
| | 5 | 226,7 | 231,8 | 8,3 | |
| | N | 5 | 5 | | |
| | Mean | 189,02 | 233,24 | | |
| | Std. Deviation | 6,53 | 5,00 | | |
| | Std. Error | 2,66 | 2,04 | | |
| SD Rats | Sham | Weight (g) 0° day | Weight (g) 7° day | Δ weight | mean |
| | 1 | 280 | 293,4 | -1 | 3,5 |
| | 2 | 231 | 236,2 | 3,4 | |
| | 3 | 285 | 290 | 5 | |
| | 4 | 278,6 | 282 | 6,2 | |
| | 5 | 233,7 | 225 | 3,9 | |
| | N | 5 | 5 | | |
| | Mean | 261,66 | 304,62 | | |
| | Std. Deviation | 6,90 | 6,84 | | |
| | Std. Error | 2,82 | 2,793 | | |

From observance 15 days after intra-articular injection of HA-CD, all animals survived (Figure 8). No clinical signs and no mortality were observed in all experimental groups until the end of the experiment (Table 9 and 10).

**Table 9:** Clinical signs of female rats

| Experimental Groups | Numbers | Doses | Mortality | Clinical Signs* | | | | | | | | | | | | | |
|---|---|---|---|---|---|---|---|---|---|---|---|---|---|---|---|---|---|
| Days | | | 14 | 1 | 2 | 3 | 4 | 5 | 6 | 7 | 8 | 9 | 10 | 11 | 12 | 13 | 14 |
| Sham | 1 | * | 0 | 0 | 0 | 0 | 0 | 0 | 0 | 0 | 0 | 0 | 0 | 0 | 0 | 0 | 0 |
| | 2 | * | 0 | 0 | 0 | 0 | 0 | 0 | 0 | 0 | 0 | 0 | 0 | 0 | 0 | 0 | 0 |
| | 3 | * | 0 | 0 | 0 | 0 | 0 | 0 | 0 | 0 | 0 | 0 | 0 | 0 | 0 | 0 | 0 |
| | 4 | * | 0 | 0 | 0 | 0 | 0 | 0 | 0 | 0 | 0 | 0 | 0 | 0 | 0 | 0 | 0 |
| | 5 | * | 0 | 0 | 0 | 0 | 0 | 0 | 0 | 0 | 0 | 0 | 0 | 0 | 0 | 0 | 0 |
| | | | | | | | | | | | | | | | | | |
| HA-CD | 1 | 20 mg/ml | 0 | 0 | 0 | 0 | 0 | 0 | 0 | 0 | 0 | 0 | 0 | 0 | 0 | 0 | 0 |
| | 2 | 20 mg/ml | 0 | 0 | 0 | 0 | 0 | 0 | 0 | 0 | 0 | 0 | 0 | 0 | 0 | 0 | 0 |
| | 3 | 20 mg/m | 0 | 0 | 0 | 0 | 0 | 0 | 0 | 0 | 0 | 0 | 0 | 0 | 0 | 0 | 0 |
| | 4 | 20 mg/ml | 0 | 0 | 0 | 0 | 0 | 0 | 0 | 0 | 0 | 0 | 0 | 0 | 0 | 0 | 0 |
| | 5 | 20 mg/ml | 0 | 0 | 0 | 0 | 0 | 0 | 0 | 0 | 0 | 0 | 0 | 0 | 0 | 0 | 0 |
| * Clinical signs evaluated: Changes in skin and fur, eyes and mucous membranes, and also respiratory, circulatory, autonomic and central nervous system, and somatomotor activity and behaviour pattern. Attentions should be directed to observations of tremors, convulsions, salivation, diarrhoea, lethargy, sleep and coma. | | | | | | | | | | | | | | | | | |

**Table 10:** Clinical signs of male rats

| Experimental Groups | Numbers | Doses | Mortality | Clinical Signs* | | | | | | | | | | | | | |
|---|---|---|---|---|---|---|---|---|---|---|---|---|---|---|---|---|---|
| Days | | | 14 | 1 | 2 | 3 | 4 | 5 | 6 | 7 | 8 | 9 | 10 | 11 | 12 | 13 | 14 |
| Sham | 1 | * | 0 | 0 | 0 | 0 | 0 | 0 | 0 | 0 | 0 | 0 | 0 | 0 | 0 | 0 | 0 |
| | 2 | * | 0 | 0 | 0 | 0 | 0 | 0 | 0 | 0 | 0 | 0 | 0 | 0 | 0 | 0 | 0 |
| | 3 | * | 0 | 0 | 0 | 0 | 0 | 0 | 0 | 0 | 0 | 0 | 0 | 0 | 0 | 0 | 0 |
| | 4 | * | 0 | 0 | 0 | 0 | 0 | 0 | 0 | 0 | 0 | 0 | 0 | 0 | 0 | 0 | 0 |
| | 5 | * | 0 | 0 | 0 | 0 | 0 | 0 | 0 | 0 | 0 | 0 | 0 | 0 | 0 | 0 | 0 |
| | | | | | | | | | | | | | | | | | |
| HA-CD | 1 | 20 mg/ml | 0 | 0 | 0 | 0 | 0 | 0 | 0 | 0 | 0 | 0 | 0 | 0 | 0 | 0 | 0 |
| | 2 | 20 mg/ml | 0 | 0 | 0 | 0 | 0 | 0 | 0 | 0 | 0 | 0 | 0 | 0 | 0 | 0 | 0 |
| | 3 | 20 mg/m | 0 | 0 | 0 | 0 | 0 | 0 | 0 | 0 | 0 | 0 | 0 | 0 | 0 | 0 | 0 |
| | 4 | 20 mg/ml | 0 | 0 | 0 | 0 | 0 | 0 | 0 | 0 | 0 | 0 | 0 | 0 | 0 | 0 | 0 |
| | 5 | 20 mg/ml | 0 | 0 | 0 | 0 | 0 | 0 | 0 | 0 | 0 | 0 | 0 | 0 | 0 | 0 | 0 |
| * Clinical signs evaluated: Changes in skin and fur, eyes and mucous membranes, and also respiratory, circulatory, autonomic and central nervous system, and somatomotor activity and behaviour pattern. Attentions should be directed to observations of tremors, convulsions, salivation, diarrhoea, lethargy, sleep and coma. | | | | | | | | | | | | | | | | | |

No major differences were observed in body weight changes in all experimental groups, as shown in Table 11 referring to female rats and Table 12 referring to male rats.

**Table 11:** Body weight of female rats

| SD Rats | HA-CD | Weight (gr) 0° Days | Weight (gr) 5° Days | Weight (gr) 10° Days | Weight (gr) 14° Days | Δ weight From 0° to 14° Days | mean |
|---|---|---|---|---|---|---|---|
| | 1 | 326 | 310 | 315 | 317 | 9 | 16,6 |
| | 2 | 293 | 291 | 289 | 283 | 10 | |
| | 3 | 309 | 321 | 310 | 290 | 19 | |
| | 4 | 304 | 299 | 285 | 281 | 23 | |
| | 5 | 315 | 301 | 297 | 293 | 22 | |
| | N | 5 | 5 | 5 | 5 | | |
| | Mean | 309,400 | 304,400 | 299,200 | 292,800 | | |
| | Std. Deviation | 12,300 | 11,480 | 13,008 | 14,394 | | |
| | Std. Error | 5,50 | 5,13 | 5,81 | 6,43 | | |
| | | | | | | | |
| SD Rats | Sham | Weight (gr) 0° Days | Weight (gr) 5° Days | Weight (gr) 10° Days | Weight (gr) 14° Days | Δ weight From 0° to 14° Days | mean |
| | 1 | 310 | 311 | 313 | 315 | -5 | -10,8 |
| | 2 | 291 | 294 | 299 | 301 | -10 | |
| | 3 | 285 | 289 | 301 | 306 | -21 | |
| | 4 | 278 | 280,1 | 283 | 286 | -8 | |
| | 5 | 280 | 281 | 284 | 290 | -10 | |
| | N | 5 | 5 | 5 | 5 | | |
| | Mean | 288,800 | 291,020 | 296 | 299,600 | | |
| | Std. Deviation | 12,872 | 12,568 | 12,610 | 11,803 | | |
| | Std. Error | 5,75 | 5,62 | 5,63 | 5,27 | | |

**Table 12:** Body weight of male rats

| SD Rats | HA-CD | Weight (gr) 0° Days | Weight (gr) 5° Days | Weight (gr) 10° Days | Weight (gr) 14° Days | Δ weight From 0° to 14° Days | mean |
|---|---|---|---|---|---|---|---|
| | 1 | 447 | 443 | 445 | 447 | 0 | 4,6 |
| | 2 | 412 | 411 | 421 | 426 | -14 | |
| | 3 | 393 | 390 | 388 | 385 | 8 | |
| | 4 | 404 | 401 | 399 | 391 | 13 | |
| | 5 | 415 | 410 | 401 | 399 | 16 | |
| | N | 5 | 5 | 5 | 5 | | |
| | Mean | 414,200 | 411 | 410,800 | 409,600 | | |
| | Std. Deviation | 20,216 | 19,786 | 22,521 | 26,130 | | |
| | Std. Error | 9,04 | 8,84 | 10,07 | 11,68 | | |
| | | | | | | | |
| SD Rats | Sham | Weight (gr) 0° Days | Weight (gr) 5° Days | Weight (gr) 10° Days | Weight (gr) 14° Days | Δ weight From 0° to 14° Days | mean |
| | 1 | 308 | 310 | 312 | 313 | -5 | 1 |
| | 2 | 388 | 390 | 391 | 393 | -5 | |
| | 3 | 385 | 383 | 380 | 382 | 3 | |
| | 4 | 301 | 314 | 311 | 303 | -2 | |
| | 5 | 398 | 391 | 390 | 388 | 10 | |
| | N | 5 | 5 | 5 | 5 | | |
| | Mean | 356 | 357,600 | 356,800 | 355,800 | | |
| | Std. Deviation | 47,323 | 41,765 | 41,578 | 43,951 | | |
| | Std. Error | 21,16 | 18,67 | 18,59 | 19,49 | | |

No major differences in gross pathology and organ weight were observed in the period up to 15 days after intra-articular administration of HA-CD. Gross pathology included: the external surface of the body, all orifices, cranial, thoracic and abdominal cavities. The following organ weights were recorded; brain, liver, kidneys, adrenal glands, ovaries, heart, epididymis, spleen and testes (Table 12 and 13).

**Table 13:** Female rat organ weights

| | SHAM | | | | | | |
|---|---|---|---|---|---|---|---|
| **ORGANS** | 1 | 2 | 3 | 4 | 5 | | **AVERAGE** |
| ADRENALS (g) | 0,14 | 0,11 | 0,12 | 0,09 | 0,14 | | 0,120 |
| BRAIN (g) | 1,07 | 1,11 | 1,09 | 1,02 | 1,04 | | 1,066 |
| HEART (g) | 0,89 | 1,09 | 0,87 | 1,1 | 0,99 | | 0,988 |
| KIDNEYS (g) | 0,87 | 0,91 | 1,01 | 0,99 | 0,89 | | 0,934 |
| LIVER (g) | 8,78 | 8,56 | 7,98 | 7,84 | 7,91 | | 8,214 |
| OVARIES (g) | 0,09 | 0,1 | 0,11 | 0,14 | 0,15 | | 0,118 |
| SPLEEN (g) | 0,45 | 0,53 | 0,69 | 0,74 | 0,69 | | 0,620 |

| | HA-CD | | | | | | |
|---|---|---|---|---|---|---|---|
| **ORGANS** | 1 | 2 | 3 | 4 | 5 | | **AVERAGE** |
| ADRENALS (g) | 0,03 | 0,08 | 0,07 | 0,12 | 0,11 | | 0,082 |
| BRAIN (g) | 1,82 | 1,43 | 1,51 | 1,48 | 1,58 | | 1,564 |
| HEART (g) | 0,89 | 1,54 | 1,34 | 1,23 | 1,08 | | 1,216 |
| KIDNEYS (g) | 1,21 | 1,12 | 0,99 | 0,97 | 0,99 | | 1,056 |
| LIVER (g) | 6,31 | 6,43 | 7,45 | 8,31 | 8,12 | | 7,324 |
| OVARIES (g) | 0,11 | 0,08 | 0,1 | 0,13 | 0,13 | | 0,11 |
| SPLEEN (g) | 0,98 | 0,45 | 0,71 | 0,73 | 0,71 | | 0,716 |

**Table 14:** Male rat organ weights

| | SHAM | | | | | | |
|---|---|---|---|---|---|---|---|
| **ORGANS** | 1 | 2 | 3 | 4 | 5 | | **AVERAGE** |
| ADRENALS (g) | 0,14 | 0,15 | 0,19 | 0,17 | 0,18 | | 0,166 |
| BRAIN (g) | 1,75 | 1,81 | 1,99 | 1,84 | 1,91 | | 1,860 |
| EPIDIDYMIDES (g) | 0,91 | 0,98 | 0,99 | 0,87 | 0,83 | | 0,916 |
| HEART (g) | 1,32 | 1,54 | 1,21 | 1,34 | 1,22 | | 1,326 |
| KIDNEYS (g) | 1,75 | 1,99 | 2,54 | 2,61 | 2,75 | | 2,328 |
| LIVER (g) | 12,21 | 12,98 | 12,84 | 12,36 | 12,87 | | 12,652 |
| SPLEEN (g) | 0,91 | 0,99 | 1,01 | 1,05 | 1,15 | | 1,022 |
| TESTES (g) | 3,24 | 3,52 | 3,98 | 3,12 | 3,01 | | 3,374 |

| | HA-CD | | | | | | |
|---|---|---|---|---|---|---|---|
| **ORGANS** | 1 | 2 | 3 | 4 | 5 | | **AVERAGE** |
| ADRENALS (g) | 0,16 | 0,19 | 0,14 | 0,13 | 0,15 | | 0,154 |
| BRAIN (g) | 1,57 | 1,83 | 1,94 | 1,91 | 1,81 | | 1,812 |
| EPIDIDYMIDES (g) | 0,93 | 0,91 | 0,85 | 0,89 | 0,99 | | 0,914 |
| HEART (g) | 1,51 | 1,23 | 1,41 | 1,35 | 1,42 | | 1,384 |
| KIDNEYS (g) | 1,93 | 2,43 | 2,47 | 1,91 | 1,85 | | 2,118 |
| LIVER (g) | 12,83 | 13,09 | 14,87 | 14,13 | 13,98 | | 13,780 |
| SPLEEN (g) | 0,87 | 0,76 | 0,86 | 1,01 | 1,13 | | 0,926 |
| TESTES (g) | 3,41 | 3,97 | 3,86 | 3,76 | 3,67 | | 3,734 |

From the histologic evaluation it was observed that no variation had occurred in the organs of the animals treated with HA-CD, compared with control group (Sham), as shown in the pictures below (Figures 34-39)

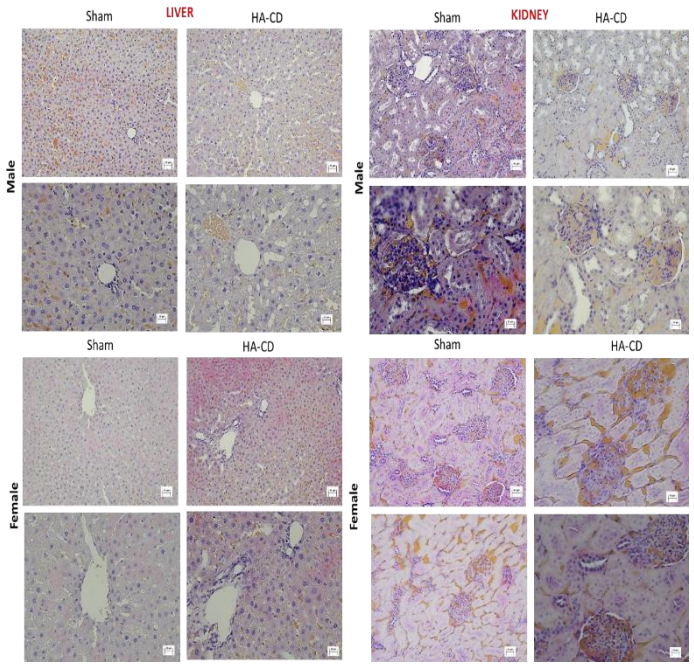


**Figure 34:** Histologic evaluation live and kidney

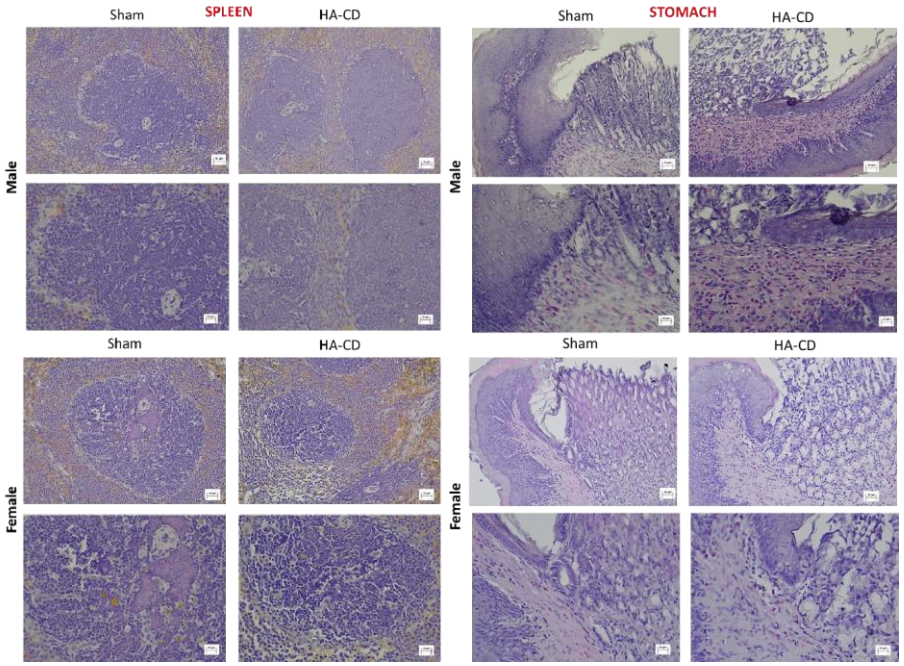


**Figure 35:** Hystologic Evaluation spleen and stomach

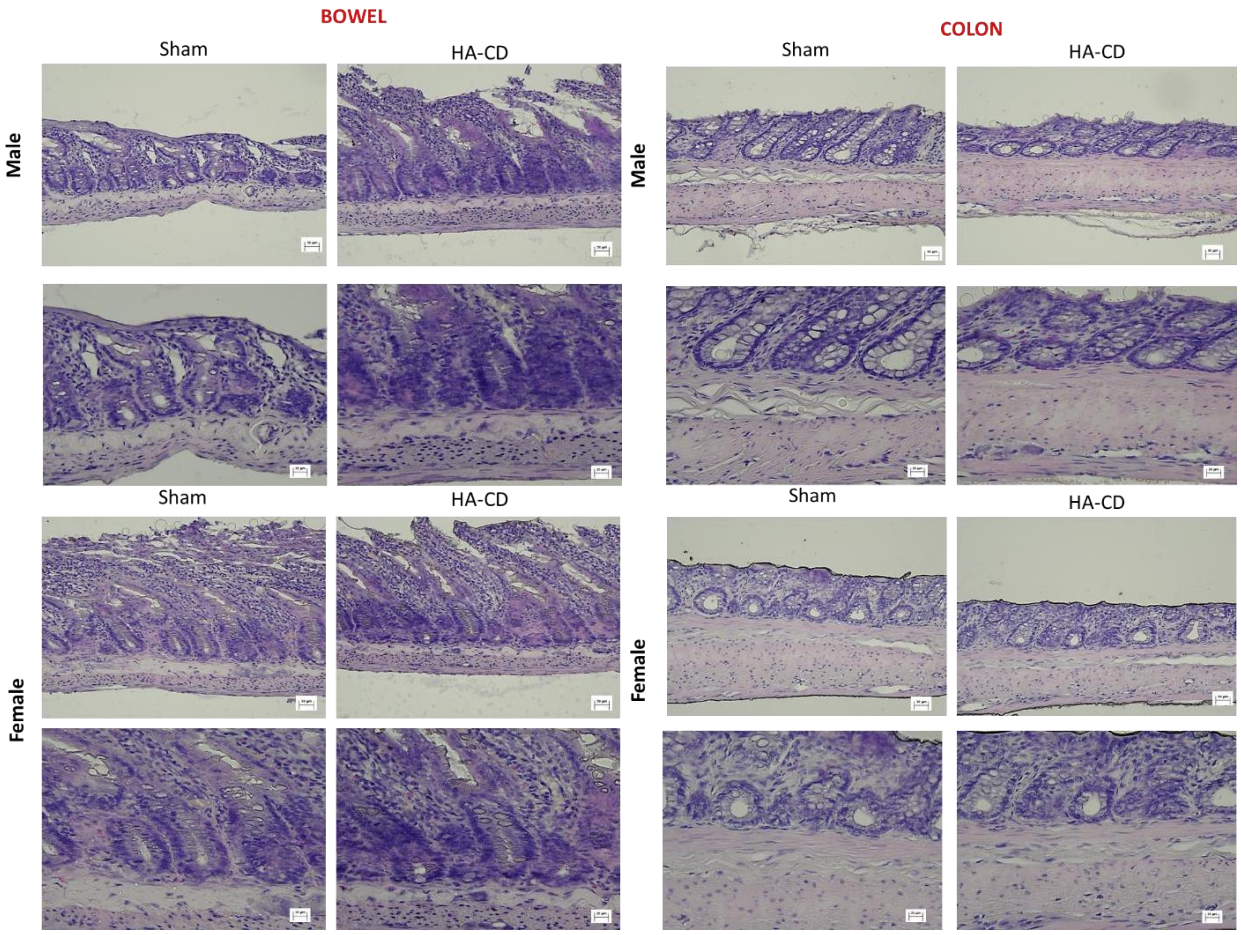


**Figure 36**: Hystologic evaluation Bowel and colon

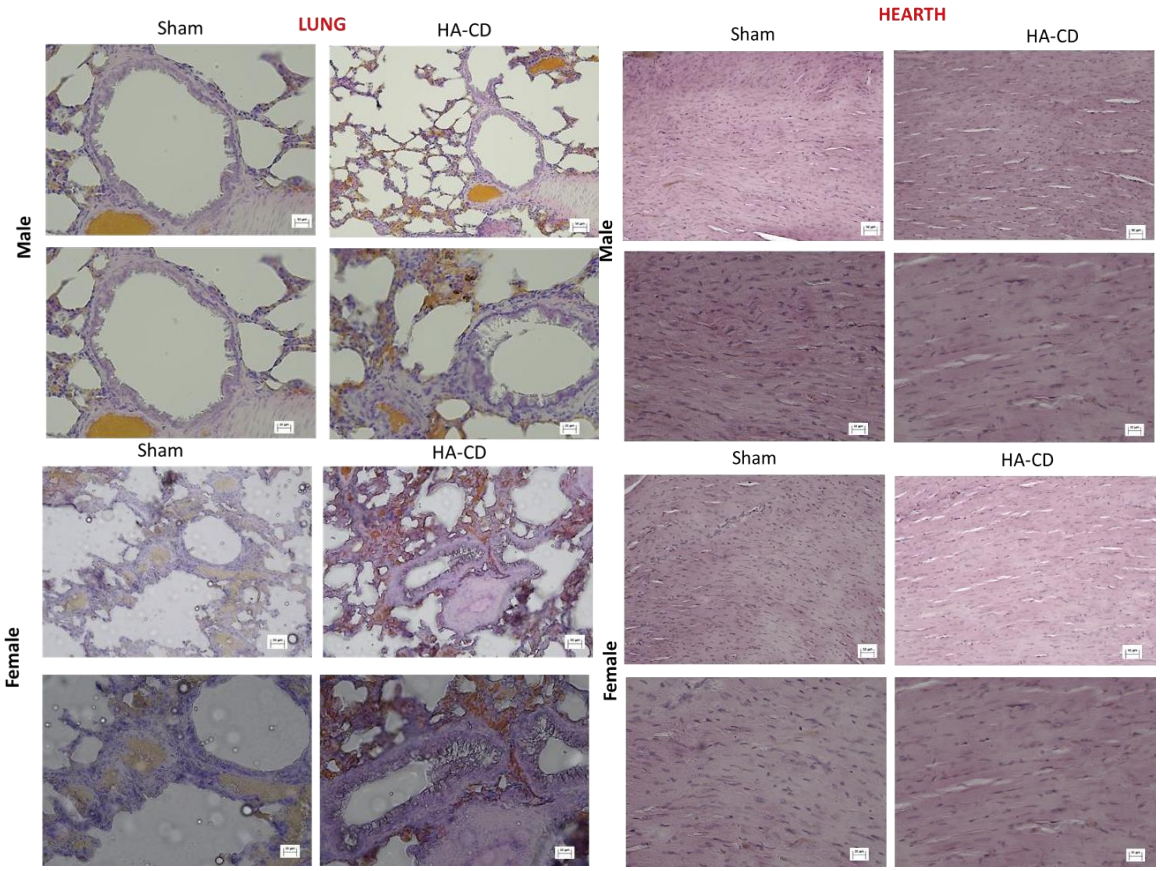


**Figure 37:** Hystologic evaluation of lung and heart

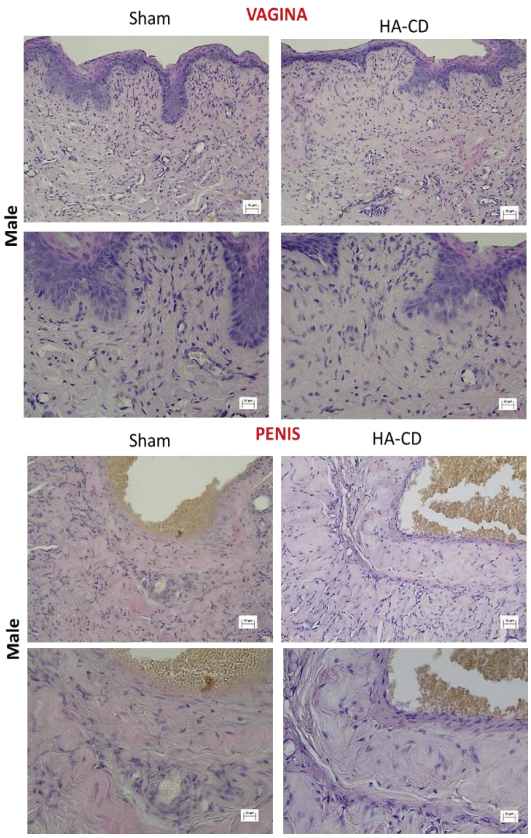


**Figure 38:** Hystological evaluation of penis and vagina

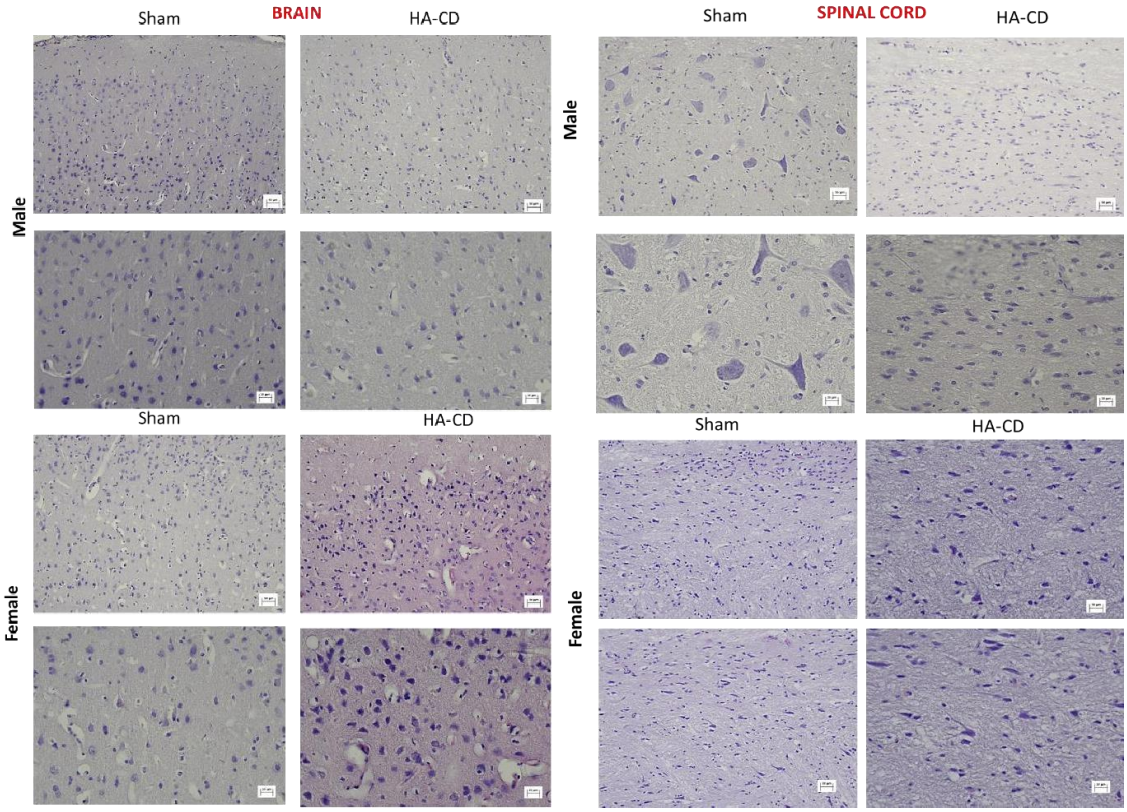


**Figure 39** Hystological evaluation of brain and spinal cord

The cell viability test carried out 24 hours after the treatment with HA-CD and HA-CD/DCF demonstrated slight cytotoxicity for the therapy with HA-CD (HA-CD Group) and in association with Diclofenac (HA-CD Group/ DCF) (Figure 40).

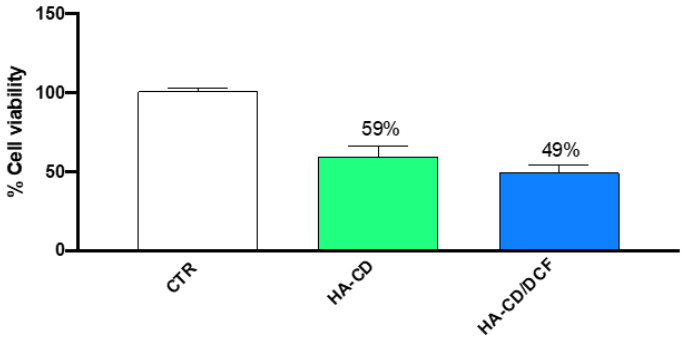


**Figure 40:** Cell viability assay on U2OS cells.

From mechanical allodynia test it was reported that induction of osteosarcoma from intratibial injection of U2OS type cells has reduced greatly paw withdrawals threshold; and both treatments with DCF e HA-CD/CDF has increased significantly pain tolerance level caused by osteosarcoma (Fig. 41).

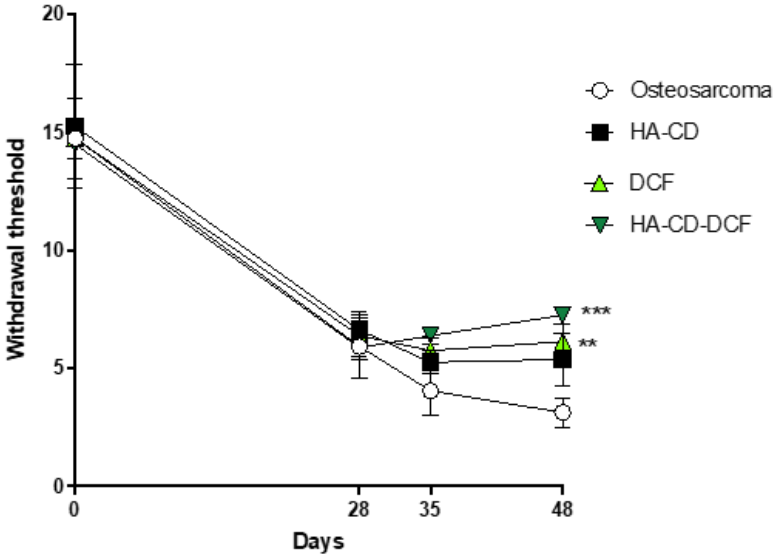


**Figure 41:** Von Frey test. ** $p < 0.01$ vs osteosarcoma group; *** $p < 0.001$ vs osteosarcoma group.

From Von Frey test we observed that DCF e HA-CD/DCF treatments has increased greatly paw withdrawals threshold compared to non-treated animals.

After four weeks, tibial tumour resulted well consolidated and increased in dimensions. It was observed in the osteosarcoma group necrosis area, evidentiated from loss of integrity of bone tissue on tibia level, invading surrounding soft tissue. While with HA-CD treatment it wasn't observed any significant hystopathologic improvement, invasion and growth of tumoral cells was mitigated from treatment with DCF and HA-CD/DCF; observing an improvement of bone tissue and reduction of necrosis area. (Fig. 42).

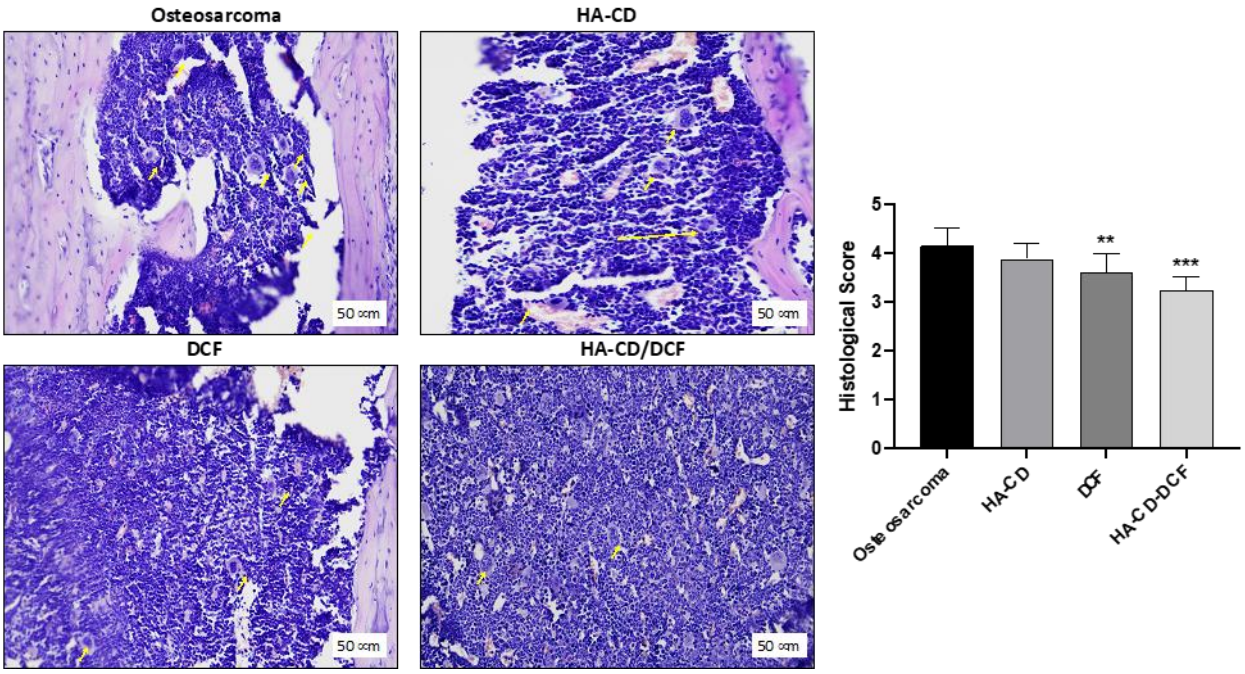


**Figure 42**: Hystological evaluation. ** $p < 0.01$ vs osteosarcoma group; *** $p < 0.001$ vs osteosarcoma group.

Sovraexpression of tumoral marker Ki-67 results correlated in the increase of malignity level of bone tumors, osteosarcoma included [57] Immunohistochemistry analysis has revealed that animal with osteosarcoma presented a high number of cells positive at Ki67 marker. Conversely, DCF and HA-CD/DCF treatment has reduced significantly the number of cells positive Ki67. HA-CD treatment has not apported any significant changes number of cells positive to Ki67 compared to ostheosarcoma ones (Fig. 43).

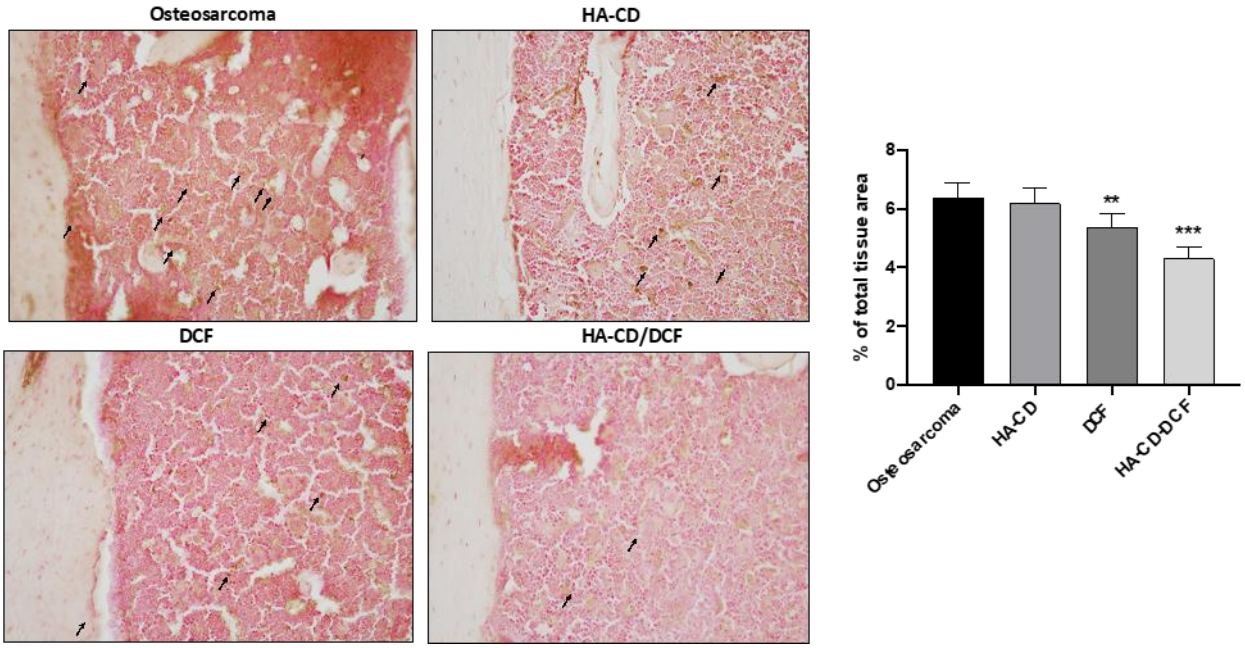


**Figure 43:** Immunohistochemistry analysis for Ki67. ** $p < 0.01$ vs osteosarcoma group; *** $p < 0.1$ vs osterosarcoma group.

# CONCLUSIONS

From biological assays, several analyses were conducted to identify the safety of the materials used to treat osteoarticular pathologies, using the drug delivery system based on the bioconjugate between hyaluronic acid and cyclodextrin. Both experimental models demonstrated that HA-CD a good safety profile, as it was non-cytotoxic to murine fibroblast cells and non-toxic when administered intratibial in both female and male rats in no organ examined. Also, several analyses were conducted to identify the effectiveness of materials used as a treatment for osteoarticular pathologies through the drug delivery system based on HA-CD containing a well-known anti-inflammatory, Diclofenac (DCF), through an in vivo study of osteosarcoma induced by intratibial injection of tibial sarcoma cells (U2OS cell type). The two-week treatment of HA-CD/DCF in animals that had developed the pathology of osteosarcoma was shown to be effective in reducing intratibial allodynia as well as the pain caused by the induction of osteosarcoma. Furthermore, by histological and immunohistochemical analysis of the cellular proliferation marker Ki67, regression of the tibia tumour with the increasing repair of the surrounding soft tissues was observed following treatment with HA-CD/DCF.

# MONO AND BI-METALLIC HYBRID HA-CD DRUG DELIVERY SYSTEMS

## Introduction

Nanoparticles are defined as matter with a diameter between 1 and 100 nm, as indicated by IUPAC [58-60], although objects up to 500 nm can be displayed. They can have different shapes and sizes, as well as be made of various materials as shown in Fig 25. The peculiarity of this type of matter is the presence of new or different chemical-physical properties distinct from those of the bulk material, due precisely to their small size. They can be used as such or modified superficially with organic material to adapt their use to the target audience.

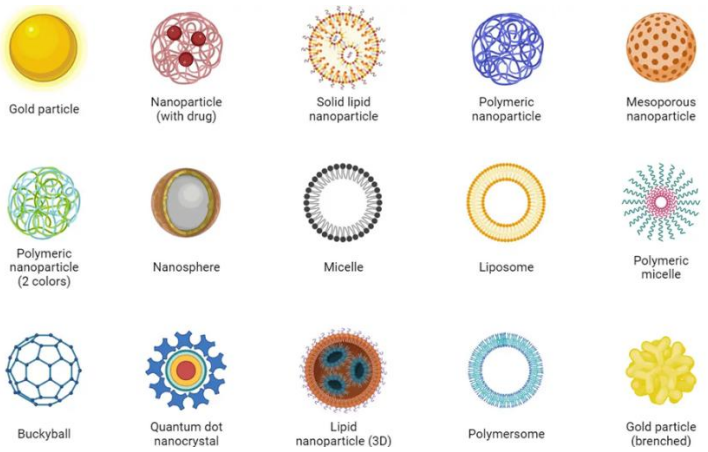


**Figure 25**: Different types of Nanoparticles [61]

Noble metal nanoparticles (NPs), in particular those composed of gold and/or silver, are versatile agents endowed with unique physicochemical properties, which recently have drawn great interest for a variety of applications ranging from catalysis to nanomedicine. Gold nanoparticles (Au NPs) were synthesized for the first time in the 50s by *Turkevic* [62]. The peculiar optical properties are due to the presence of the LSPR (localized surface plasmon resonance) phenomenon caused by the electrons on the surface. This phenomenon allows a greater absorption and scattering of magnetic radiation, in conjunction with the aforementioned band, giving the particles optical properties and colors different from the bulk material [63,64]. This among their biocompatibility and capability to be functionalized open a series of applications (Fig. 26) including biomedicine. Therefore, Au NPs nanoparticles are considered versatile in this branch, however to enhance certain feature it is recently considered to modified them pairing with another metal, forming bi-metallic species such as core-shell [65]

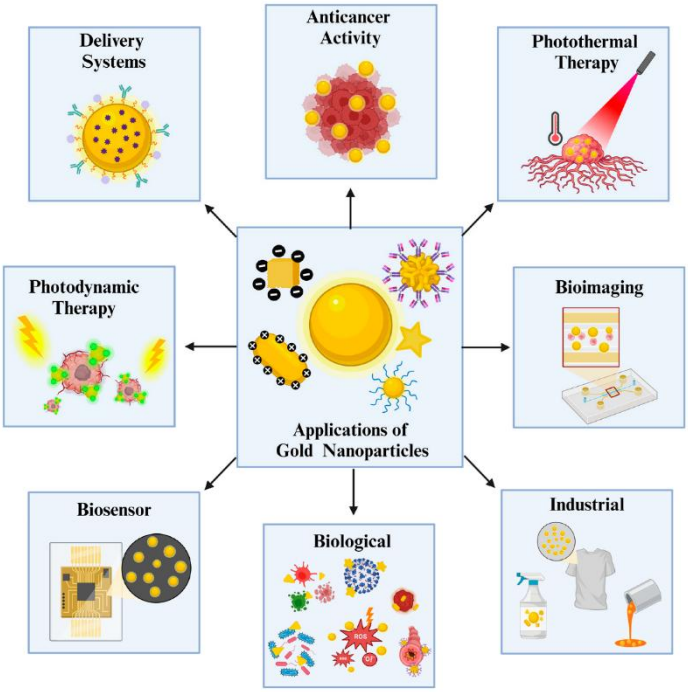


**Figure 26** Application of Gold Nanoparticles [66-69]

Magnetic nanoparticles are a type of nano-magnetic material, with the characteristics of small particle size, large surface area, magnetic response and super paramagnetism. Due to the applications of magnetic nanoparticles [MNPs] in biotechnology, biomedical, material science, engineering, and environmental areas, the synthesis of different kinds of MNPs is a field of large interest. [68] Magnetic materials can be classified into five major classes: ferro-, ferri-, para-, antiferro-, and dia-magnetism according to their magnetic behavior. Ferro- and ferrimagnetism are the basic mechanisms in permanent magnets. Superparamagnetism is a form of magnetism that appears in small ferro- or ferrimagnetic nanoparticles (Figure 27).

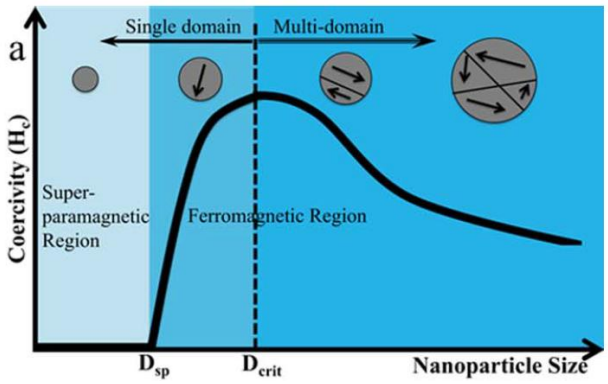


**Figure 27:** Transition from superparamagnetic to the multi-domain region [66].

Ferromagnetic and paramagnetic materials in this state can behave as superparamagnetic: a property that guarantees an effective response to an external magnetic field, which can guide them in the desired direction, without the presence of residual magnetization [70]. The cases considered in the literature are mainly concerned with using magnetite and maghemite [71], different mineral forms of iron oxide, which are easily synthesised in bulk in the laboratory by acid or basic precipitation of iron salts. Although different methodologies for the synthesis of iron nanoparticles have been known for years, the difficulty lies in obtaining a satisfactory result in terms of reproducibility due to the various sizes of the particles obtained and methodologies that require, in some cases, the use of relatively strong/polluting chemicals that therefore make it difficult to use the particles in the nanopharmaceuticals field [72] (Figure 28 [73]).

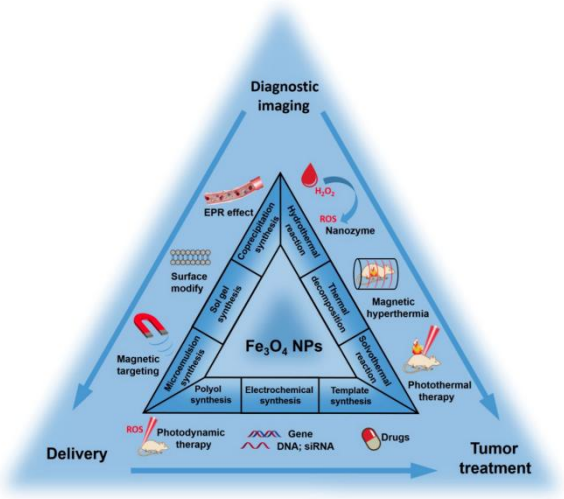


**Figure 28:** applications of Fe3O4 NPS [73]

Multifunctional nanoparticles (NPs) originated by the combination of multiple components on a nanometer scale have attracted great interest in the field of nanomedicine due to their physicochemical properties and integrated functionalities and the consequent broad spectrum of biomedical applications including ultrasensitive biosensing, imaging, targeted therapy [74]. The surface functionalization of a magnetic core with a gold-shell has enabled the creation of diverse nanocomposites that possess improved, complementary, even novel properties. Specifically, the gold coating onto magnetic NPs endows them of unique magnetic and optical properties ensuring biocompatibility, especially for photothermal therapy [55].

## Result and discussion

Mono metallic HA-CD@Au NPs were prepared by reduction of $HAuCl_4$ using HA-CD as both reducing and capping agent [54,56], due to its functional groups, such as amines, primary and secondary alcohols, hemiacetals, able to interact and stabilize Au NPS. The method is known as seeding growth, implying a sequential reduction of both metals, carry on the formation of core–shell particles. The formation of small gold NPs was confirmed by the presence of the LSPR band detected at 526 nm in the UV–vis spectrum (Figure 42). The characteristically plasmonic peak is recognizable at 519 nm also in bimetallic species. Stability of NPs was monitored by UV-Vis analysis (Figure 44-46).

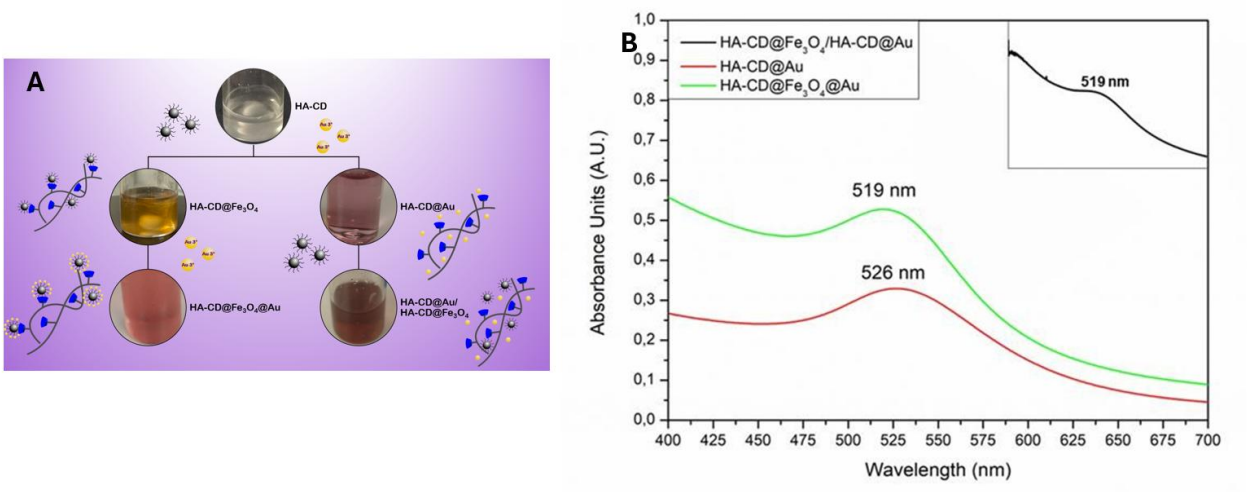


**Figure 44:** A) Mono and bimetallic nanoparticles; B) UV-vis spectra of mono and bimetallic species with Au NPs

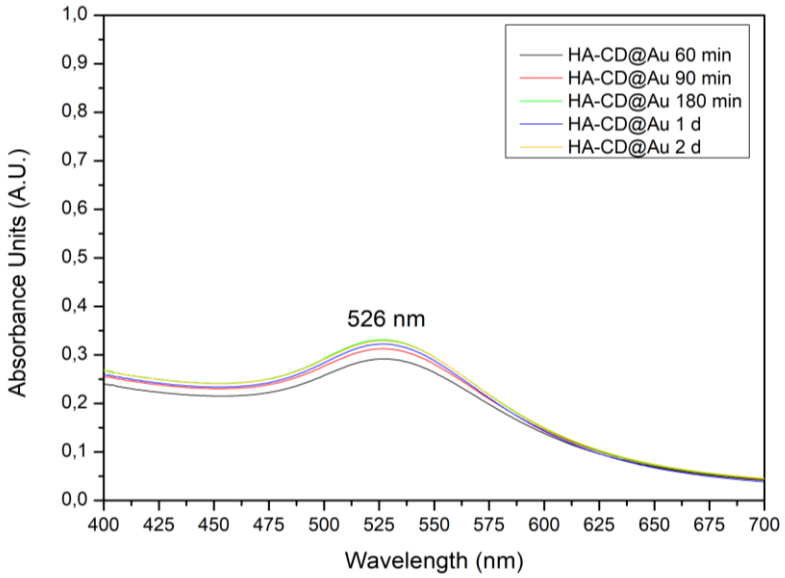


**Figure 45:** stability of HA-CD@Au

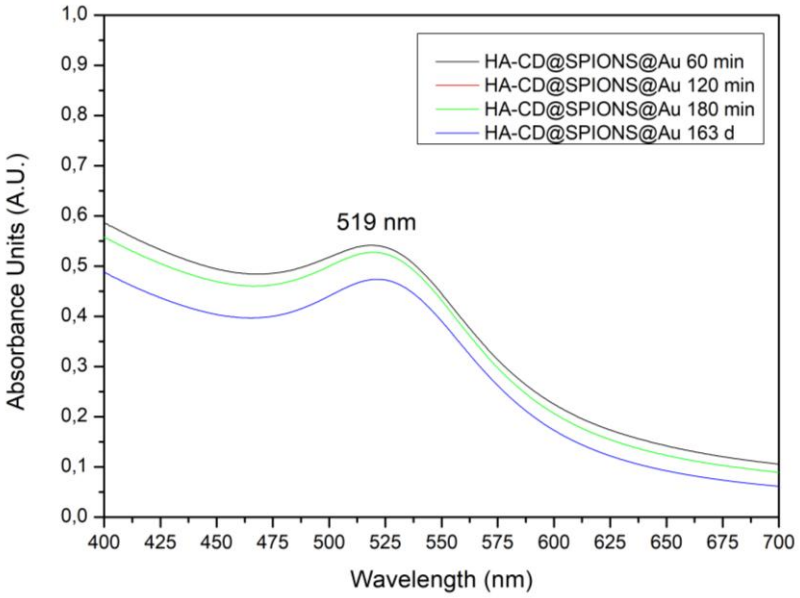


**Figure 46:** stability of HA-CD@Fe3O4@Au

Magnetic properties of magnetic nanoparticles were evaluated during the research period abroad at the Nanotech Solutions (NTSOL, Spain) under the supervision of Dr Francisco J Teran. Two methodologies were employed: alternating current (indicated as AC) and SQUID. The magnetic saturation, coercivity and remanence parameters were evaluated. From the magnetometric analysis of monometallic species, it is noted that the magnetite in toluene and the magnetite conjugated to HA-CD maintain the same behaviour; In the core-shell system, the magnetization of the system is lost,

probably due to the external shell of the gold, while the double population system maintains a lower magnetization compared to systems with only magnetite. (a sign that gold can partially shield the saturation). The SQUID (figure 47) confirms this change in the magnetic behaviour between the monometallic species and the core shells, in which linear progress can be seen in the second case in the analyses carried out at 298 K. At low temperatures both systems lose their properties and we observe a different behaviour

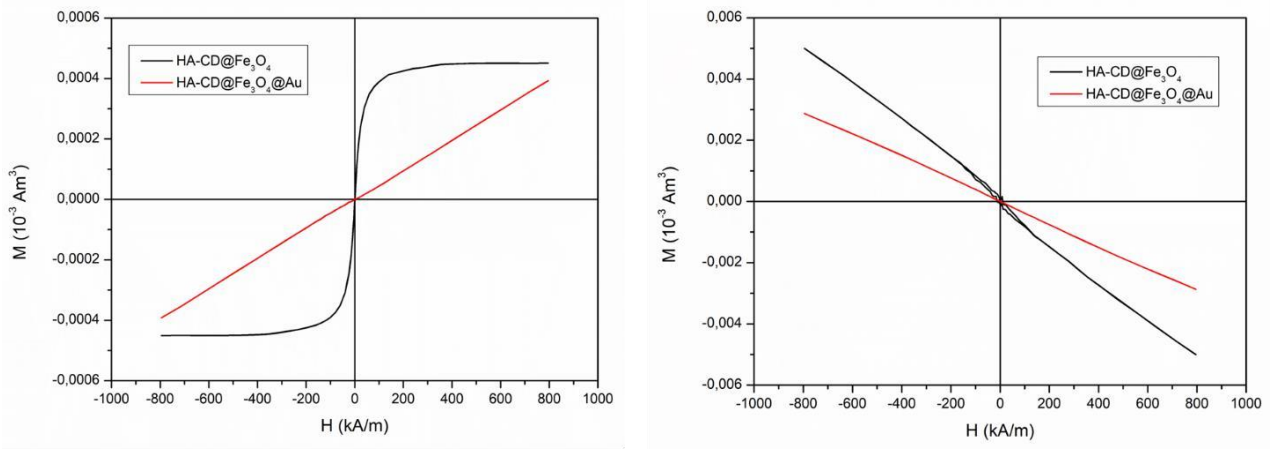


**Figure 47:** SQUID magnetic measurements of HA-CD@Fe (black) and HA-CD@Fe@Au (red) in water, at 298 K(A) and(B) 4 K

The morphological characterization of the species was carried out using TEM (figure 48). For magnetic monometallic species, particles with a diameter between 8 and 12 nm are observed, while for gold ones the range is wider; from 5 to 13 nm. The core-shell system instead presents particles that reach up to 16-17 nm in diameter, which is not present in the bimetallic system, where they maintain the "measurements" of the individual populations.

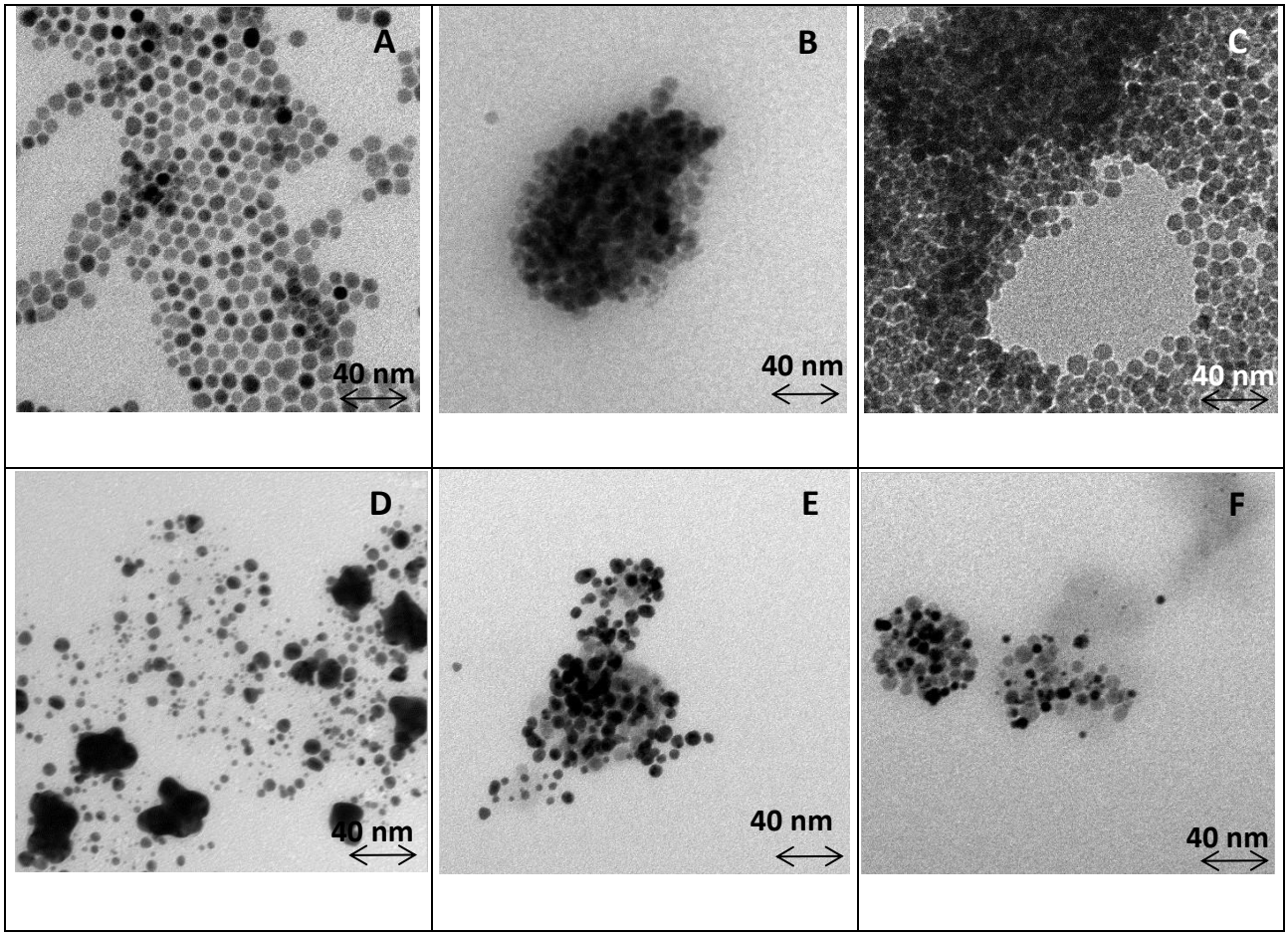


**Figure 48:** TEM analysis (scale 40 nm) of mono and bimetallic species, A) SPIONS, B) HA-CD@Fe C) HA-CD@Fe, D) HA-CD@Au, E) HA-CD@Fe@Au, F)HA-CD@Au@Fe

# CONCLUSIONS

In this research PhD thesis the synthetic strategy for the preparation of hyaluronic acid β-cyclodextrin conjugate (HA-CD) was described. HA-CD resulted an exellect biomaterial for the preparation of magnetic HACD@Fe3O4 NPs and magnetoplasmonic HACD@$Fe_3O_4$@Au NP by and a mild, ecofriendly, and straightforward strategy. The morphology, colloidal stability and magnetic properties of new nanoarchitectures have been investigated by complementary techniques including UV-vis, Dynamic Light Scattering (DLS), ζ-potential, AC magnetization and transmission electron microscopy (TEM) analyses.

HA-CD@Fe@Au resulted stable and combines the qualities of AuN PS with $Fe_3O_4$ NPS, albeit with a partial loss of magnetic behaviour due to gold coating. The promising properties of magnetoplasmonic nanoparticles will be exploited for the development of innovative drug delivery systems.

## MATERIALS AND METHODS

Hyaluronic Acid Sodium Salt (HANa, 600-700 kDa) was kindly provided by Fidia Farmaceutici SPA, local Unit of Noto (Italy). Mono-6-deoxy-6-azido- β-cyclodextrin (β-$CDN_3$) was synthesized according to literature method [35]. HA-Alk and HA-CD are synthesized in a reported manner [75] All other reagents, unless indicated differently are purchased from Sigma-Aldrich (Milano); AmberChrom™ 50WX8 50-100 Mesh ($H^+$) Cation Exchange Resin, Ultrapure water, Acetonitrile, N-methyl-morpholine (NMM), 2-chloro-4,6- dimethoxy-1,3,5-triazine (CDMT), Copper sulphate ($CuSO4 \cdot 5H2O$) and sodium ascorbate diclofenac sodium salt (DCF), $H2O$ for injectable solutions, $H2O$ saline solution 0.9%, Pure acetone .

## CHARACTERIZATION

**Uv-vis:** UV-Vis characterization was performed on a model Jasco V-730 using 1 cm path length quartz cells at r.t. ≅ 25 °C. Steady state fluorescence spectroscopy Steady-state fluorescence measurements were performed on a Jasco model FP-750 spectrofluorometer by using a 1 cm path length quartz cell. UV- Vis

**AC magnetic hysteresis loop:** AC analyses were performed at IMDEA nanociencia, using a commercial inductive magnetometer (AC Hyster, Nanotech Solutions). The Advance AC Hyster Series magnetometer offers a wider field frequency range from 10 kHz up to 300 kHz and field intensities up to 24 kAm that are automatically selected. Each magnetization cycle is obtained out of three repetitions, resulting in the averaged magnetization cycle and the related magnetic parameters ($H_C$, $M_R$, area).

**SQUID:** SQUID analyses were performed at "Tecnicas Fisicas" lab in Facultad de Fisica,; Universidad compluntense de Madrid, on a Quantum Design MPMS-XL (Magnetic Property Measurement Systems) magnetometer, with a continuous operating temperature range between 1.9K and 400 K. Maximum magnetic field of +-5T.

**TEM:** Transmission Electron Microscopy images of samples were performed in Servicio de Microscopía Electrónica del Centro de Biología Molecular “Severo Ochoa” in a Jeol JEM-1010 microscope equipped with a CMOS 4K × 4K, F416 de TVIPS camera.

**Synthesis of HA-CD:** High molecular Sodium Hyaluronate (700-800 KDa) was dissolved in ultrapure water and acidified with AmberChrom™ 50WX8 50-100 Mesh (H+) Cation Exchange Resin; to obtain HA the product was centrifugated and freeze-dried. To obtain HA-Alk a reaction was

set up between HA, acetonitrile, followed by 4-methylmorpholine (NMM), 2-chloro-4,6-dimethoxy-1,3,5-triazine (CDMT; added ad cool temperature then stirred at room temperature) and 2-(prop-2-yn-1-yloxy) ethan-1-amine (linker). The mixture was purified via centrifugation, dialysis and lyophilization. HA-CD is synthesized with a click chemistry reaction between HA-Alk and $CDN_3$, with sodium ascorbate, $CuSO_4*5H_2O$ under argon atmosphere, and purified as described previously.

**Preparation of HA-CD solutions:** For the acute and subacute in vivo toxicity tests, 5 mL and 2.5 mL of a solution of HA-CD 20 mg/mL in $H_2O$ saline were prepared, respectively 0.9%, via sonication.

**Preparation of the DCF stock solution:** A 10 mM DCF stock solution (3.14 mg/mL) was prepared by dissolving 15.90 mg of the compound in 5 mL of pure acetone

**Preparation of HA-CD/DCF:** To synthesize HA-CD/DCF complex, a 1:1 eq. ratio between DCF and CD of HA-CD (SD ≈ 21%) was considered. The methodology involved the deposition of diclofenac film, by evaporating the solvent of the solution and the subsequent addition of an aqueous solution of HA-CD. 628 µL of stock solution of DCF (m = 2 mg) are evaporated and 2 mL of a 5 mg/mL solution of HA-CD in water for injections are added and placed under magnetic stirring for 24 hours (tab 1.3) In a second vial, 3.144 mL of DCF solution (m = 10 mg) evaporates to form the organic film. 5 mL of an aqueous solution of HA-CD 10 mg/mL is added and left under magnetic stirring (tab 1.6). The resulting solutions are called HA-CD/DCF 1 and 2 Two more sample of HA-CD/DCF (called HA-CD/DCF A and B) are prepared using the previous method prescribed, using 1.56 mL of stock solution of DCF (m = 5 mg) and 5 mL of a 5 mg/mL solution of HA-CD in water for injectable solutions. After 24 h and 48h UV- vis analysis are performed.

**Release profile tests:** For the UV-vis analysis were prepared: 2 mL solution of 0,06 mg/mL of DCF in water for injectable solutions, 2 mL solution of 0,16 mg/mL HA-CD and 2 mL of HA-CD/DCF solutions using 63.8 µL aliquot of the synthetized solutions. Release profile of DCF from HA-CD/DCF nanoassembly was evaluated in PBS by a dialysis method using dialysis tubes. The dialysis tubes were prewashed using three solutions: 10% ethanol (for 10 minutes), distilled water (for 20 minutes), and water for injections (overnight). Subsequently, the tubes were washed with PBS. 5 mL of PBS was poured into the outer chamber and 1 mL of HA-CD/DCF solution in PBS (500 mM DCF, 0.8 mg/mL HA-CD) into the inner chamber. The systems were placed in two baths of distilled water thermostated at 37°C under slow magnetic stirring (250 rpm). At fixed times, 1 ml of release medium was withdrawn and replaced with an equal volume of fresh aqueous solution of PBS. The evaluations

were made at 2h, 4h, 6h, 24h, 48h, 72h, 6, 7 and 8 days. A second release profile of DCF from HA-CD/DCF A nano assembly was evaluated in PBS by a dialysis method using dialysis tubes. The dialysis tubes were prewashed using three solutions: 10% ethanol (for 10 minutes), then distilled water for two times (20 minutes each). Subsequently, the tube was washed with PBS. 5 mL of PBS was poured into the outer chamber and 1 mL of HA-CD/DCF solution in PBS (500 mM DCF, 0.8 mg/mL HA-CD) into the inner chamber. The evaluations were made at 1h, 2h, 4h, 6h, 24h, 48h, 72h, 96h, 7 and 8 days.

**Biological evaluation**

Toxicity evaluation of HA-CD using acute and subacute toxicity tests in vitro and in vivo (rat) following ISO-10993-11 guidelines.

**In vitro study:** Fibroblast cells of the L-929 cell line were used for the acute toxicity test. The 3-(4,5-dimethylthiazol- 2l)-2,5-diphenyltetrazolium bromide cell viability assay (MTT assay) was performed. Briefly, L-929 cells were plated on 96-well plates at a density of 4 × 104 cells/well to a final volume of 150 µL and after 24 h were treated with 1% SDS, HA-CD (1 :3), HA-CD/DCF (1:3), and HA-CD@Au@Ag (1:2). After 24 hours, cells were incubated at 37°C with MTT (0.2 mg/mL) for 1 hour. Then, the medium was removed and the cells were lysed with 100 µL dimethyl sulfoxide (DMSO). The amount of MTT reduced to formazan was quantified by measuring the optical density (OD) at 550 nm with a microplate reader.

**In vivo study:** Rats are the preferred rodent species for this acute toxicity test, and females are recommended for such subacute toxicity testing in case differences are found between male and female rats, with females usually being the more sensitive sex.
Male rats (acute test), and male and female rats (subacute test) weighing 250-300 g were used. Experiments on animals comply with the Italian legislation on protecting animals used for experimental and other scientific purposes (DM 116192) and with the European regulation (2010/63/EU). Results to be recorded include body weight, organ weight, observations of any sign(s) of toxicity, gross pathological change after 24 hours, and histopathological change after 15 days.

**Experimental design**

Acute toxicity: 6 female rats

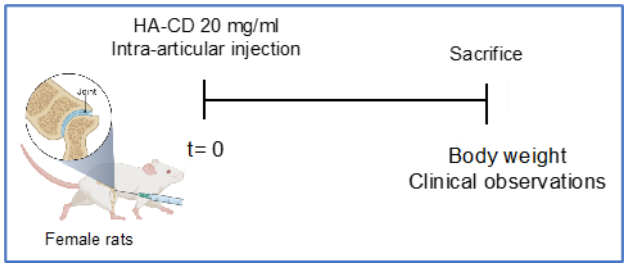


**Figure 50:** Acute toxicity experimental design

Subacute toxicity: 6 female rats and 6 male rats.

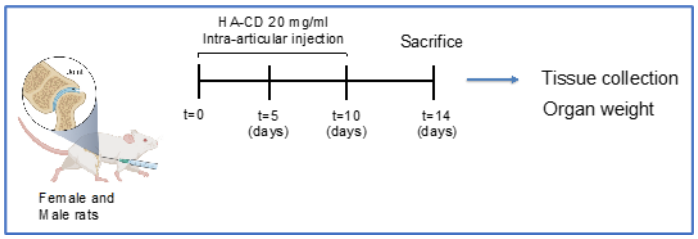


**Figure 51:** Subacute toxicity experimental design

**Treatment**

Animals were treated with HA-CD with a single intra-articular administration (dose 20 mg/ml).

*Acute systemic toxicity:* The animals received a single dose of HA-CD over 24 hours. Signs of toxicity were recorded as they were observed. Body weights were recorded before the start of the experiment and before the end of the test. General clinical characteristics or appearance and behavioural observations were recorded for up to 24 hours.

*Subacute systemic toxicity:* Animals received repeated doses (every 5 days) of HA-CD within 15 days. Body weights were recorded before the start of the experiment, on the days of treatment and before the end of the test. General clinical characteristics or appearance and behavioural observations were recorded up to day15. At the end of the study, necropsy was conducted on all control and treated rats. Organ weights were recorded, and histopathological analysis was performed.

*Survival:* To identify whether HA-CD treatment could influence the longevity of animals over the 15 days, the survival of both female and male animals was assessed at days 0, 5, 10, and at the end of the test.

*Clinical signs:* The animals were observed individually after administration every 5 days for up to 15 days. Changes in the skin and fur, eyes and mucous membranes, respiratory, circulatory, autonomic and central nervous systems, somatomotor activity and behavioural pattern. Attention was paid to

observations of tremors, convulsions, salivation, diarrhoea, lethargy, sleep, and coma.

*Body weight:* The body weight of the animals was measured at the beginning of the test (on day 0), on day 5, 10 after administration and at the end of the test (on day 15).

*Histopathological evaluation:* At the end of the test (on day 15), female and male animals were sacrificed. Subsequently, the organs such as liver, lungs, kidneys, spleen, brain, marrow, stomach, intestine, colon, penis, and vagina were collected and used for histological evaluation. Tissues were fixed in 10% (w/v) PBS-buffered formaldehyde solution at 25°C for 24 hours, dehydrated with graded ethanol, and subsequently embedded in paraffin (obtaining 7-µm-thick sections). Haematoxylin and eosin (H&E) staining was performed to identify histological damage and loss of tissue architecture. After H&E staining, sections were examined by light microscopy using objectives of 20× and 40× magnification.

**Experimental groups**

Sham: group of control animals to which saline (vehicle) was administered intraarticularly (n=6); HA-CD: group of animals to which HA-CD was administered intraarticularly (n=6 males and n=6 females).

**In vitro study of osteosarcoma**

Toxicity evaluation of HA-CD and HA-CD/DCF was evaluated with cell viability test, conducted on osteosarcoma cells of type U2OS. It was performed viability cell test of 3-(4,5-dimethylthiazol-2-yl)-2,5-diphenyltetrazolium bromide (MTT test). Briefly, U2OS cells were plated on 96-well plates at 4 × 104 cells/well density until reaching the final volume of 150 µL and after 24 hours treated with SDS 1%, HA-CD, e HA-CD/DCF. After 24 hours, the cells were incubated at 37°C with MTT (0,2 mg/mL) for 1 hour. Then, the medium was removed, and the cells were lysed with 100 µL of dimethyl sulfoxide (DMSO). Quantity of MTT reduced to formazan was quantified measuring the optical density (OD) at 550 nm with a microplate reader.

**In vivo study of osteosarcoma**

*Animals:* Male mice weighing 250-300 g of the BALB/c strain were used. Experiments on animals comply with the Italian legislation on protecting animals used for experimental and other scientific purposes (DM 116192) and with the European regulation (2010/63/EU).

*Intratibial implantation of U2OS cells*

Animals were treated with HA-CD (10 mg/kg), DCF (1 mg/kg) and HA-CD/DCF (10 mg/kg and 1 mg/kg respectively) with a single intra-articular administration four weeks after induction of

osteosarcoma for two subsequent weeks [77]

Experimental groups: Osteosarcoma group: group of animals injected with the suspension of cells from the U2OS line (2x106 cells/mouse) intratibially (n=8);

HA-CD group: group of animals to which HA-CD (10 mg/kg) was administered orally (n=8) four weeks after the induction of osteosarcoma for two subsequent weeks;

DCF group: group of animals to which DCF (1 mg/kg) was administered orally (n=8) four weeks after the induction of osteosarcoma for two subsequent weeks;

HA-CD/DCF group: group of animals to which HA-CD/DCF (10 mg/kg and 1 mg/kg respectively) was administered orally (n=8) four weeks after the induction of osteosarcoma for the next two weeks.

*Von Frey test:* The von Frey test is a method used to evaluate mechanical allodynia in rodents. For the application of Von Frey filaments, mice were placed one by one on a raised platform and a monofilament was applied perpendicular to the plantar surface of the hind paw. A positive response consisted of quickly withdrawing the paw, licking it, or shaking it during monofilament application or immediately after filament removal [78].

*Histological analysis:* Six weeks after tumour induction, the animals were sacrificed and the hindlimbs were immediately harvested and fixed in 4% paraformaldehyde in PBS at 4°C for 24 h. After fixation, the articles were transferred to a sterile decalcifying solution. Decalcification was performed for 2 weeks. Therefore, the samples were embedded in paraffin and tibia sections were cut for histological analysis (7 μm). After deparaffinization, sections were stained with hematoxylin and eosin to evaluate histological damage [79].

*Immunohistochemical analysis for Ki67:* Tissue sections from the hind limbs (tibia) were processed for immunohistochemical analysis of the tumour marker Ki67. Tibia sections were incubated overnight with anti-Ki67 antibody (#MA5-14520, Invitrogen). The percentage of positive staining was detected using a computerized image analysis system, and images were acquired using an optical microscope.

# BIBLIOGRAPHY

[1] Boldyrev AA, Aldini G, Derave W. Physiology and pathophysiology of carnosine. Physiol Rev. 2013 Oct;93(4):1803-45.

[2] Kamal MA, Jiang H, Hu Y, Keep RF, Smith DE. Influence of genetic knockout of Pept2 on the in vivo disposition of endogenous and exogenous carnosine in wild-type and Pept2 null mice. Am J Physiol Regul Integr Comp Physiol *296*: R986–R991, 2009.

[3] Solana-Manrique, C.; Sanz, F.J.; Martínez-Carrión, G.; Paricio, N. Antioxidant and Neuroprotective Effects of Carnosine: Therapeutic Implications in Neurodegenerative Diseases. Antioxidants 2022

[4Branham, M. L., Singh, P., Bisetty, K., Sabela, M., & Govender, T. Preparation, spectrochemical, and computational analysis of l-Carnosine (2-[(3-Aminopropanoyl) amino]-3-(1 H-imidazol-5-yl) propanoic Acid) and Its Ruthenium (II) coordination complexes in aqueous solution. Molecules, (2011), 16(12), 10269-10291.

[5] Abate, C.; Piperno, A.; Fragoso, A.; Giuffrè, O.; Mazzaglia, A.; Scala, A.; Foti, C. Thermodynamic and voltammetric study on carnosine and ferrocenyl- carnosine. Dalton Transactions 2023, 52 (12), 3699– 3708

[6] Martina Medvidović-Kosanović, Anamarija Stanković, Mateja Drulak, Milan Sak-Bosnar, Potentiometric, electrochemical and UV/VIS investigation of a copper (II) complex with β-alanyl-L-histidine, International Journal of Electrochemical Science, Volume 13, Issue 6, 2018, Pages 5323-5332

[7] Okuda, Jun. "Ferrocene-Chemie und Materialeigenschaften: Ferrocenes. Hrsg. von A. Togni und T. Hayashi. VCH, Weinheim, 1995. 540 S., geb., 248, (1995): 994-995.

[8] Moriuchi, T "Helical chirality of ferrocene moieties in cyclic ferrocene-peptide conjugates." Europ ean Journal of Inorganic Chemistry 2022.5 (2022):

[9] Pal, A., Karmakar, M., Bhatta, S. R., & Thakur, A. A detailed insight into anion sensing based on intramolecular charge transfer (ICT) mechanism: A comprehensive review of the years 2016 to 2021. Coordination Chemistry Reviews, (2021), 448, 214167.

[10] Huang Y., Mosleh I., Abbaspourrad A. Impact of protein/peptide templates on metallic nanoparticle synthesis and applications // Nano-Structures and Nano-Objects. 2022. Vol. 30. p. 100864.

[11] J. Xie, Y. Zheng, J.Y. Ying, Protein-directed synthesis of highly fluorescent gold nanoclusters, J. Am. Chem. Soc. 131 (3) (2009) 888–889.

[12] Z. Durmus, H. Kavas, A. Baykal, H. Sozeri, L. Alpsoy, S.U. Celik, M.S. Toprak, Synthesis and

characterization of l-carnosine coated iron oxide nanoparticles, J. Alloys Compd. 509 (2011) 2555–2561

[13] Hua Li, Jia Chen, Hong Huang, Jiu-Ju Feng, Ai-Jun Wang, Lin-Xiang Shao, Green and facile synthesis of l- carnosine protected fluorescent gold nanoclusters for cellular imaging, Sensors and Actuators B: Chemical, Volume 223, 2016, Pages 40-44, ISSN 0925-4005

[14] C.-A.J. Lin, C.-H. Lee, J.-T. Hsieh, H.-H. Wang, J.K. Li, J.-L. Shen, W.-H. Chan, H.-I. Yeh, W.H. Chang Synthesis of fluorescent metallic nanoclusters toward biomedical application: recent progress and present challenges J. Med. Biol. Eng., 29 (2009), pp. 276-283

[15] R.N. Hegde, S.T. Nandibewoor, Electrochemical Oxidation of Pentoxifylline and its Analysis in Pure and Pharmaceutical Formulations at a Glassy Carbon Electrode, Analytical Letters, 41 (2008) 977-991

[16] H. Beitollahi, M.A. Khalilzadeh, S. Tajik, M. Safaei, K. Zhang, H.W. Jang, M. Shokouhimehr, Recent Advances in Applications of Voltammetric Sensors Modified with Ferrocene and Its Derivatives, ACS Omega, 5 (2020) 2049- 205

[17] R.H. Patil, R.N. Hegde, S.T. Nandibewoor, Electro-oxidation and determination of antihistamine drug, cetirizine dihydrochloride at glassy carbon electrode modified with multi-walled carbon nanotubes, Colloids and Surfaces B: Biointerfaces, 83 (2011) 133-138

[18] H. Karimi-Maleh, H. Beitollahi, P. Senthil Kumar, S. Tajik, P. Mohammadzadeh Jahani, F. Karimi, C. Karaman, Y. Vasseghian, M. Baghayeri, J. Rouhi, P.L. Show, S. Rajendran, L. Fu, N. Zare, Recent advances in carbon nanomaterials-based electrochemical sensors for food azo dyes detection, Food and Chemical Toxicology, 164 (2022) 112961

[19] Bélteki, Rita, et al. "The Role of the Amino Acid Molecular Characteristics on the Formation of Fluorescent Gold-and Silver-Based Nanoclusters." Chemistry–A European Journal 29.45 (2023): e202300720.

[20] C. Abate, G. Neri, A. Scala, P.G. Mineo, E. Fazio, A. Mazzaglia, A. Fragoso, O. Giuffrè, C. Foti, A. Piperno, Screen-Printed Carbon Electrodes with Cationic Cyclodextrin Carbon Nanotubes and Ferrocenyl- Carnosine for Electrochemical Sensing of Hg(II), ACS Applied Nano Materials, 6 (2023) 17187- 17195

[22] Martínez-Castañón, G.A., Niño-Martínez, N., Martínez-Gutierrez, F. *et al.* Synthesis and antibacterial activity of silver nanoparticles with different sizes. *J Nanopart Res* **10**, 1343–1348 (2008).

[23] A.R. Urade, I. Lahiri, K.S. Suresh, Graphene Properties, Synthesis and Applications: A Review, JOM, 75 (2023) 614-630

[24] Lu Z., Rong K., Li J., Yang H., Chen R. Size-dependent antibacterial activities of silver

nanoparticles against oral anaerobic pathogenic bacteria. J. Mater. Sci. Mater. Med. 2013;24:1465–1471.

[25] G. Neri, A. Scala, F. Barreca, E. Fazio, P.G. Mineo, A. Mazzaglia, G. Grassi, A. Piperno, Engineering of carbon-based nanomaterials by ring-opening reactions of a reactive azlactone graphene platform, Chemical Communications, 51 (2015) 4846-4849.

[26] Bélteki, R., Kuklis, L., Gombár, G., Ungor, D., & Csapó, E. (2023). The Role of the Amino Acid Molecular Characteristics on the Formation of Fluorescent Gold-and Silver-Based Nanoclusters. Chemistry–A European Journal, 29(45)

[27] Zhang, Y., Sun, D., Shen, J., & Xin, X. (2020). Dynamic self-assembly of silver nanoclusters into luminescent nanotubes with controlled surface roughness: Scaffold of superhydrophobic materials. *Applied Surface Science*, *514*, 145913.

[28] Kong, J., Zhao, S., Han, X., Li, W., Zhang, J., Wang, Y., ... & Li, Z. (2023). Quantitative Ratiometric Biosensors Based on Fluorescent Ferrocene-Modified Histidine Dipeptide Nanoassemblies. *Analytical Chemistry*, *95*(11), 5053-5060.

[29] Huang, M., Kong, J., Zhang, J., Wang, Z., Hao, D., Zhang, J., ... & He, Z. (2022). Enhanced polychromatic luminescence of bionic peptidyl nanoparticles driven by hydrogen bonds. Particle & Particle Systems Characterization, 39(2), 2100260.

[30] Wood, D. M., and N. W. Ashcroft. "Quantum size effects in the optical properties of small metallic particles." *Physical review B* 25.10 (1982): 6255.

[31] Abhishek, N., Verma, A., Singh, A., & Kumar, T. (2023). Metal-conducting polymer hybrid composites: A promising platform for electrochemical sensing. Inorganic Chemistry Communications, 157, 111334.

[32] Yadav, M., Singh, G. & Lata, S. Revisiting Some Recently Developed Conducting Polymer@Metal Oxide Nanostructures for Electrochemical Sensing of Vital Biomolecules: A Review. J. Anal. Test. 6, 274–295 (2022).

[33] Piperno, A., Mazzaglia, A., Scala, A., Pennisi, R., Zagami, R., Neri, G., ... & Sciortino, M. T. (2019). Casting light on intracellular tracking of a new functional graphene-based microrna delivery system by flim and raman imaging. ACS Applied Materials & Interfaces, 11(49), 46101-46111.

[34] G. Maduraiveeran, W. Jin, Carbon nanomaterials: Synthesis, properties and applications in electrochemical sensors and energy conversion systems, Materials Science and Engineering: B, 272 (2021) 115341

[35] T.T. Nielsen, V. Wintgens, C. Amiel, R. Wimmer, K.L. Larsen, Facile Synthesis of β-Cyclodextrin-Dextran Polymers by “Click” Chemistry, Biomacromolecules, 11 (2010) 1710-1715.

[36] T.A. Nguyen, J.-U. Lee, D. Yoon, H. Cheong, Excitation Energy Dependent Raman Signatures

of ABA- and ABC-stacked Few-layer Graphene, Scientific Reports, 4 (2014) 4630
[37] G. Neri, A. Scala, E. Fazio, P.G. Mineo, A. Rescifina, A. Piperno, G. Grassi, Repurposing of oxazolone chemistry: gaining access to functionalized graphene nanosheets in a top-down approach from graphite, Chemical Science, 6 (2015) 6961-697
[38] Patino, Y., Pilehvar, S., Diaz, E., Ordonez, S., & De Wael, K. (2017). Electrochemical reduction of nalidixic acid at glassy carbon electrode modified with multi-walled carbon nanotubes. *Journal of Hazardous Materials*, *323*, 621-631.
[39] Patil, R. H., Hegde, R. N., & Nandibewoor, S. T.; Electro-oxidation and determination of antihistamine drug, cetirizine dihydrochloride at glassy carbon electrode modified with multi-walled carbon nanotubes. Colloids and Surfaces B: Biointerfaces, 83(1), 2011, 133-138.
[40] Afkhami, A., Ghaedi, H., Madrakian, T., Nematollahi, D., & Mokhtari, B.; Electro-oxidation and voltammetric determination of oxymetholone in the presence of mestanolone using glassy carbon electrode modified with carbon nanotubes. Talanta, 2014, 121, 1-8.
[41] Hrichi, H., Monser, L., & Adhoum, N.; A novel electrochemical sensor based on electropolymerized molecularly imprinted poly (aniline-co-anthranilic acid) for sensitive detection of amlodipine. Journal of Electroanalytical Chemistry, 2017, 805, 133-145.
[42] Kang, W., Pei, X., Bange, A., Haynes, E. N., Heineman, W. R., & Papautsky, I.; Copper-based electrochemical sensor with palladium electrode for cathodic stripping voltammetry of manganese. Analytical Chemistry, 2014, 86(24), 12070-12077.
[43] Sahani, M. K., Singh, A. K., & Jain, A. K.; Nano-level monitoring of Mn2+ ion by fabrication of coated pyrolytic graphite electrode based on isonicotinohydrazide derivatives. *Materials Science and Engineering: C, 2015*, *50*, 124-132.
[44] Kang, W., Rusinek, C., Bange, A., Haynes, E., Heineman, W. R., & Papautsky, I.; Determination of manganese by cathodic stripping voltammetry on a microfabricated platinum thin–film electrode. Electroanalysis, 2017, 29(3), 686-695.
[45] Joca, J. F., Felix, F. S., & Angnes, L.; Ultrasonic-assisted digestion of cement and clinker samples for the determination of manganese by square wave cathodic stripping voltammetry. *Analytical Letters*,2020, *53*(7), 1075-1086..
[46] Rocha, D. P., Foster, C. W., Munoz, R. A., Buller, G. A., Keefe, E. M., & Banks, C. E.; Trace manganese detection via differential pulse cathodic stripping voltammetry using disposable electrodes: additively manufactured nanographite electrochemical sensing platforms. *Analyst*, *145*(9), 2020, 3424-3430.
[47] Lai, Z., Lin, F., Qiu, L., Wang, Y., Chen, X., & Hu, H., . Development of a sequential injection analysis device and its application for the determination of Mn (II) in water. *Talanta*, 2020, *211*,

120752.
[48] Pei, Y., McLeod, J. F., Payne, S. J., & She, Z., A comparative study of electroanalytical methods for detecting manganese in drinking water distribution systems. *Electrocatalysis*, 2021, *12*, 176-187.
[49] Boselli, E., Wu, Z., Friedman, A., Claus Henn, B., & Papautsky, I., Validation of electrochemical sensor for determination of manganese in drinking water. *Environmental science & technology*, 2021, *55*(11), 7501-7509.
[50] Mc Eleney, C., Alves, S., & Mc Crudden, D., Novel magneto-electrochemical determination of Mn (II). *Journal of Electroanalytical Chemistry*,, 2021, *900*, 115734.
[51] Roushani, M., Saedi, Z., Hamdi, F., & Dizajdizi, B. Z., Preparation an electrochemical sensor for detection of manganese (II) ions using glassy carbon electrode modified with multi walled carbon nanotube-chitosan-ionic liquid nanocomposite decorated with ion imprinted polymer. *Journal of Electroanalytical Chemistry*, 2017, *804*, 1-6.
[52] Wu, Z., Heineman, W. R., Haynes, E. N., & Papautsky, I. Electrochemical Determination of Manganese in Whole Blood with Indium Tin Oxide Electrode. *Journal of the Electrochemical Society*, 2022, *169*(5), 057508.
[53] Lamothe, N., Elliott, K., Pei, Y., Shi, Y., Macdonald, K., Payne, S. J., & She, Z., Electrochemical Detection of Manganese in Drinking Water with Chronoamperometry. *Electrocatalysis*, 2024, *15*(4), 353-362.
[54] Wang, Xuandong, et al. "Multifunctional Fe3O4@ P (St/MAA)@ chitosan@ Au core/shell nanoparticles for dual imaging and photothermal therapy." ACS applied materials & interfaces 5.11 (2013): 4966-4971.
[55]; Hada, A. M., Potara, M., Astilean, S., Cordaro, A., Neri, G., Malanga, M., Piperno, A. (2022). Linezolid nanoAntiobiotics and SERS-nanoTags based on polymeric cyclodextrin bimetallic core-shell nanoarchitectures. Carbohydrate Polymers, 293, 119736.
[56] Castiello, F.R., Romo-Herrera, J.M., Farías, M.H. *et al.* “Green” seed-mediated synthesis and morphology of Au nanoparticles using β-cyclodextrin. *Gold Bull* **49**, 45–51 (2016).
[57] Zeng, M., Zhou, J., Wen, L. et al. The relationship between the expression of Ki-67 and the prognosis of osteosarcoma. BMC Cancer 21, 210 (2021)
[58] Vert M, Doi Y, Hellwich KH, Hess M, Hodge P, Kubisa P, et al. "Terminology for biorelated polymers and applications (IUPAC Recommendations 2012)". Pure and Applied Chemistry, 2012,. 84 (2): 377–410.
[59] Buzea, C., Pacheco, I. I., & Robbie, K.; Nanomaterials and nanoparticles: sources and toxicity. Biointerphases, 2007, 2(4), MR17-MR71.
[60] ASTM E 2456 - 06 Standard Terminology Relating to Nanotechnology

[61] Wahnou, H. Nanoparticles. Encyclopedia. Available online: https://encyclopedia.pub/image/167 (accessed on 02 May 2025).

[62] J. Turkevich, J. Hillier, P. C. Stevenson, Nucleation and growth process in the synthesis of colloidal gold., in Discussions of the Faraday Society, n. 11, 1951, p. 55

[63] Jain, P. K., El-Sayed, I. H., & El-Sayed, M. A.; Au nanoparticles target cancer. Nano Today, 2007, 2(1), 18-29

[64] Mulvaney P., Surface plasmon spectroscopy of nanosized metal particles (1996) Langmuir, 12 (3), pp. 788 - 800,

[65] Eker, F.; Akdaşçi, E.; Duman, H.; Bechelany, M.; Karav, S. Gold Nanoparticles in Nanomedicine: Unique Properties and Therapeutic Potential. *Nanomaterials* **2024**, *14*, 1854.

[66] Bansal, S.A.; Kumar, V.; Karimi, J.; Singh, A.P.; Kumar, S. Role of Gold Nanoparticles in Advanced Biomedical Applications. Nanoscale Adv. **2020**, 2, 3764–3787.

[67] Hammami, I.; Alabdallah, N.M.; Jomaa, A.A.; Kamoun, M. Gold Nanoparticles: Synthesis Properties and Applications. J. King Saud. Univ.-Sci. **2021**, 33, 101560.

[68] Batsalova, T.; Vasil'kov, A.; Moten, D.; Voronova, A.; Teneva, I.; Naumkin, A.; Dzhambazov, B. Bimetallic Gold–Iron Oxide Nanoparticles as Carriers of Methotrexate: Perspective Tools for Biomedical Applications. Appl. Sci. 2023, 13, 12894

[69] Ma Z, Mohapatra J, Wei K, Liu JP, Sun S. Magnetic Nanoparticles: Synthesis, Anisotropy, and Applications. Chem Rev. 2023 Apr 12;123(7):3904-3943.

[70] Wu K, Su D, Liu J, Saha R, Wang JP. Magnetic nanoparticles in nanomedicine: a review of recent advances. Nanotechnology. 2019 Dec 13;30(50):502003.

[71] Nguyen, M.D.; Tran, H.-V.; Xu, S.; Lee, T.R. $Fe_3O_4$ Nanoparticles: Structures, Synthesis, Magnetic Properties, Surface Functionalization, and Emerging Applications. *Appl. Sci.* **2021**, *11*, 11301

[72] Teja, A.S.; Koh, P.-Y. Synthesis, Properties, and Applications of Magnetic Iron Oxide Nanoparticles. Prog. Cryst. Growth Charact. Mater. **2009**, 55, 22–45

[73] Sun, S.; Zeng, H. Size-Controlled Synthesis of Magnetite Nanoparticles. J. Am. Chem. Soc. **2002**, 124, 8204–8205.

[74] Zhao S, Yu X, Qian Y, Chen W, Shen J. Multifunctional magnetic iron oxide nanoparticles: an advanced platform for cancer theranostics. *Theranostics* 2020; 10(14):6278-6309.

[75] Nielsen, T.T., Wintgens, V., Amiel, C., Wimmer, R., Larsen, K.L.: Facile synthesis of β-cyclodextrin-dextran polymers by "Click". Chem. Biomacromol. 11(7), 1710–1715 (2010)

[76] Piperno, A., Zagami, R., Cordaro, A. et al. Exploring the entrapment of antiviral agents in hyaluronic acid-cyclodextrin conjugates. J Incl Phenom Macrocycl Chem 93, 33–40 (2019)

[77] Fisher JL, Mackie PS, Howard ML, Zhou H, Choong PF. The expression of the urokinase plasminogen activator system in metastatic murine osteosarcoma: an in vivo mouse model. Clin Cancer Res. 2001 Jun;7(6):1654-60.).
[78] Lanza, M.; Filippone, A.; Casili, G.; Giuffrè, L.; Scuderi, S.A.; Paterniti, I.; Campolo, M.; Cuzzocrea, S.; Esposito, E. Supplementation with SCFAs Re-Establishes Microbiota Composition and Attenuates Hyperalgesia and Pain in a Mouse Model of NTG-Induced Migraine. Int. J. Mol. Sci. 2022, 23, 4847.
[79] Filippone A, Scuderi SA, Basilotta R, Lanza M, Casili G, Bova V, Paterniti I, Esposito E. BAY-117082-driven NLRP3 inflammasome inhibition resolves nitro-glycerine (NTG) neuronal damage in in vivo model of migraine. Biomed Pharmacother. 2022

# SCIENTIFIC ACTIVITY

The fellowship supporting this work was awarded by MUR PON “Ricerca e Innovazione” 2014–2020, Azione IV “Dottorati e Contratti di ricerca su tematiche dell’Innovazione.”
The project was carried out in collaboration with Institute CNR - Istituto per i Processi Chimico Fisici (Messina). Part of this work (six months) has been carried out during a research period abroad at the Nanotech Solutions (NTSOL, Spain) under the supervision of Dr Francisco J Teran.

**Publications**

- Hada, A.-M.; Burduja, N.; **Abbate, M.;** Stagno, C.; Caljon, G.; Maes, L.; Micale, N.; Cordaro, M.; Scala, A.; Mazzaglia, A.; Piperno, A. “Supramolecular assembly of pentamidine and polymeric cyclodextrin bimetallic core–shell nanoarchitectures”, Beilstein J. Nanotechnol. 2022, 13, 1361–1369.
- Abate C., Neri G., **Abbate M.**, Cordaro M., Mineo P. G., Fazio E., Corsaro C., Giuffrè O., Foti C., and Piperno A., “Engineered carbon electrode with graphene-cyclodextrin/ferrocenyl-carnosine nanoassembly for Mn(II) detection”, RCS 2025, *under review*
- Marco Abbate Et Al . Breathing New Life into Old Silver Nitrate: Synthesis of Amphiphilic Silver Nanoclusters as Potent Antimicrobial Nanomedicines. *In preparation*

**Poster Presentation**

1. Nicola Micale, Nina Burduja, Claudio Stagno, Marco Abbate, Antonino Mazzaglia, Angela Scala, Anna Piperno “Synthesis, Characterization and Biological Profile of Pentamidine-Based Nano-Antimicrobials”, 20th International Cyclodextrin Symposium (20° ICS 2024), 13-17/06/2022, Giardini Naxos, Italy

2. Marco Abbate, Massimiliano Cordaro, Giulia Neri, Antonino Mazzaglia, Angela Scala, Anna Piperno “Noble Metal Nanoparticles as Privileged Component of Innovative Nanodrug”(SciCaSi 2022 edition) 1-2/12/2022, Reggio Calabria, Italy

3. Marco Abbate, Massimiliano Cordaro, Giulia Neri, Antonino Mazzaglia, Angela Scala, Anna Piperno “Innovative Hybrid Nano-Architectures based on Cyclodextrin-Hyaluronic Acid

Bioconjugate and Metal Nanoparticles." XVIII Convegno Scuola sulla Chimica dei Carboidrati (XVIII CSCC 2023) 25-28/06/2023, Certosa di Pontignano, Siena, Italy.

**Oral Presentation and Lectures**

1. Marco Abbate. "Noble Metal Nanoparticles as Privileged Component of Innovative Nanodrug" (Doctochem 5th edition), 29-30/11/2022, Messina, Italy

2. Marco Abbate, Massimiliano Cordaro, Giulia Neri, Antonino Mazzaglia, Angela Scala, Anna Piperno "Noble Metal Nanoparticles as Privileged Component of Innovative Nanodrug"(SciCaSi 2022 edition) 1-2/12/2022, Reggio Calabria, Italy

3. Marco Abbate. "A straightforward strategy for making mono and bimetallic magnetic nanoparticles using Hyaluronic Acid/Cyclodextrin bioconjugate" (Doctochem 6th edition), 29-30/11/2023, Messina, Italy

4. Marco Abbate, Massimiliano Cordaro, Giulia Neri, Antonino Mazzaglia, Angela Scala, Alexandru-Milentie Hada, Francisco J. Teran, Anna Piperno. "A straightforward strategy for making mono and bimetallic magnetic nanoparticles using Hyaluronic Acid/Cyclodextrin bioconjugate". 14th Spanish-Italian Symposium on Organic Chemistry (SISOC-XIV), 25-27/02/2024, Torino, Italy,

5. Marco Abbate, Massimiliano Cordaro, Giulia Neri, Antonino Mazzaglia, Angela Scala, Alexandru-Milentie Hada, Francisco J. Teran, Anna Piperno. "Mono and Bimetallic Magnetic Nanoparticles from Cyclodextrin Hyaluronic Acid Bioconjugates." 21st International Cyclodextrin Symposium (21° ICS 2024), June 10-14 2024, Dunkerque, France. Atti p.17 (Document: Thursday 13)

**Miscellaneous**

- Giulia Neri, Chiara Abate, Marco Abbate, Enza Fazio, Massimiliano Cordaro, Anna Piperno "Carbon based Nanomaterials combined with β-Cyclodextrin and Ferrocenyl-Carnosine for Electrochemical Sensing" (*Co-author*), 9th EuChemS Chemistry Congress (ECC9), 07/07/2024 - 11/07/2024 Dublin, Ireland

- Organizing committee of "II Virtual Symposium on Pericyclic Reactions and Synthesis of Carbo- And Heterocyclic Systems", Università degli Studi di Messina, 28-29/11/2024

**Participations in research projects:**

- STRIKE: “Comprehensive strategies to tackle malignant tumors: from nanomedicine and theranostic to precision medicine”